Recrystallization of 2D dimensioned Copper (Cu) foils and graphene nanosheets (GNSs) reinforced Cu matrix laminated composites

Hailong Shi

UNIVERSITÉ DE LORRAINE

HARBIN INSTITUTE OF TECHNOLOGY

DISSERTATION

To be presented at
Université de Lorraine and Harbin Institute of Technology

Hailong SHI 施海龙

To obtain the doctoral degree of
University of Lorraine and Harbin Institute of Technology

SPECIAL FIELD: Engineering Sciences

OPTION: Materials Science

Recrystallization of 2D dimensioned Copper (Cu) foils and graphene nanosheets (GNSs) reinforced Cu matrix laminated composites

To be defended on May 6th, 2021 in front of the jury:

Li Jin	Professor	Shanghai Jiao Tong University, China	Reviewer & Jury member
Leo Kestens	Professor	Universiteit Gent, Belgium	Reviewer & Jury member
Daniel Chateigner	Professor	Université de Caen Normandie, France	Jury member
Weimin Gan	Doctor HDR	Helmholtz-Zentrum Geesthacht, Germany	Co-Supervisor
Lidong Wang	Professor	Harbin Institute of Technology, China	Supervisor
Yunchang Xin	Professor	Nanjing Tech University, China	Jury member
Yudong Zhang	Doctor HDR	Université de Lorraine, France	Supervisor
Claude Esling	Professor	Université de Lorraine, France	Invited
Michael Hofmann	Doctor	Technische Universität München, Germany	Invited

Laboratoire d'Étude des Microstructures et de Mécanique des Matériaux, LEM3

7 rue Félix Savart, 57070 Metz, France

Abstract

Recrystallization is the intrinsic process of cold-deformed metallic materials that occurs inevitably during the thermal treatment. The produced recrystallization texture contributes to the anisotropy of the mechanical and physical properties. Motivated by the minimization of modern products, 2D materials and laminated composites are increasingly demanded by many applications. Thus, for both scientific and engineering purposes, investigations on the recrystallization of such materials are needed to understand the underlying mechanisms.

In this work, Cu foils and graphene nanosheets (GNSs) reinforced Cu matrix laminated composites with Cu foil thicknesses of 10 μm and 30 μm were fabricated, and the recrystallization features were thoroughly investigated from microscale to macroscale by means of SEM-EBSD for microstructure observation, neutron and synchrotron radiation for texture analysis and *in-situ* synchrotron radiation for lattice strain evaluation. The obtained data were analyzed in the frame of crystallography combined with crystal elasticity and surface energy.

The results showed that the recrystallization behavior of the Cu foils were greatly affected by the Cu foil thickness and the addition of the GNSs. For the 10 μm thick Cu foils without GNS, they underwent a transition from the cold-rolling texture to a recrystallization texture dominated by RD-rotated Cube and φ_2-rotated Copper components. The transition was screened by both intrinsic microstructural and extrinsic sample geometrical factors. The orientations of the nuclei were mainly inherited from the deformation orientations. Those with low Taylor factors (Cube, Goss and Brass) demonstrated size preference. The post-nucleation growth was affected by the biaxial thermal elastic constraint and surface energy. Due to their opposite effects, the orientations having moderate biaxial moduli and surface energy density (S, Copper, Brass and recrystallization components) survived, resulting in a mixed texture at the completion of recrystallization. The coherent Σ3 boundaries between the new components stabilized their growth through consuming the other oriented crystals separated by random high-angle boundaries. When sintered into bulk, the texture of the Cu was dominated by the orientations of the abnormally grown grains.

The effects of GNSs on the recrystallization of Cu foils were also Cu foil thickness dependent. For the 10 μm thick foils, the effect of the GNSs manifested after the samples were sintered to high temperatures (> 700 ℃). Instead of creating much constraint to the expansion of the adjacent Cu foils, the GNSs worked as a barrier preventing the penetration of the grown Cu grains, resulting in the stabilization of the recrystallization texture represented by the two rotated components.

For the Cu/GNS composite with Cu foil thickness of 30 μm, the results evidenced that a strong Cube orientation was produced in the Cu/GNS composite instead of the individual non-Cube orientations in the pure Cu stack without GNSs. Detailed strain-state analysis of the Cu foils in the Cu/GNS composite revealed that the anisotropic expansion behavior of the GNS that is incompatible with that of the Cu foils imposed multiple elastic constraints to the foils, resulting in a biaxial isostrain state in the surface layers and a uniaxial compressive strain state in the central layer. The elastic anisotropy of Cu favors the growth of the Cube oriented grains to minimize the total strain energy.

The results of the present work provide quantitative and detailed information on recrystallization of thin Cu foils and laminated composite, which contributes to deepening the understanding of recrystallization behaviour of 2D materials. The mechanisms revealed are useful for analysing abnormal grain growth in elastically strained materials and can also be applied to fabrication process for texturization or even monocrystallization.

Keywords: Recrystallization texture; Grain growth; 2D materials; Composite; Elastic strain energy; Surface energy.

Résumé

La recristallisation est le processus des métaux déformés à froid qui se produit lors du traitement thermique. La texture de recristallisation contribue à l'anisotropie des propriétés mécaniques et physiques. Motivés par la minimisation des produits, les matériaux 2D et les composites stratifiés sont de plus en plus demandés pour des applications. Ainsi, à des fins scientifiques et techniques, des recherches sur la recristallisation de tels matériaux sont nécessaires pour comprendre les mécanismes sous-jacents.

Dans ce travail, des feuilles de Cu et des composites stratifiés à matrice de Cu renforcé de nanofeuilles de graphène (GNS) avec des épaisseurs de Cu de 10 μm et 30 μm ont été fabriqués. La recristallisation ont été étudiées de l'échelle microscopique à l'échelle macroscopique par SEM-EBSD pour l'observation de microstructure, rayonnement neutronique et synchrotron pour l'analyse de texture et rayonnement synchrotron in situ pour l'évaluation de la déformation du réseau. Les données obtenues ont été analysées dans le cadre de la cristallographie combinée à l'élasticité et à l'énergie de surface.

Les résultats ont montré que le comportement de recristallisation de Cu était grandement affecté par l'épaisseur de la feuille de Cu et l'ajout des GNSs. Pour les feuilles de Cu de 10 μm sans GNSs, elles ont subi une transition de la texture de laminage à froid à une texture de recristallisation dominée par des composants Cube tourné RD et Copper tourné φ_2. La transition a été contrôlée par des facteurs intrinsèques microstructuraux et extrinsèques géométriques d'échantillons. Les orientations des germes sont héritées des orientations de déformation. Ceux avec des facteurs de Taylor faibles (Cube, Goss et Brass) ont montré une préférence de taille. La croissance post-nucléation a été affectée par la contrainte d'élasticité thermique biaxiale et l'énergie de surface. En raison de leurs effets opposés, les orientations ayant des modules biaxiaux et une densité d'énergie de surface modérés (S, Copper, Brass et composants de recristallisation) ont survécu, résultant en une texture mixte à la fin de la recristallisation. Les joints Σ3 cohérents entre les nouvelles composantes ont stabilisé leur croissance en

consommant les autres séparés par des joints aléatoires à grand angle. Une fois le Cu fritté en masse, sa texture était dominée par les orientations des grains à croissance anormale.

Les effets des GNSs sur la recristallisation des feuilles de Cu dépendaient également de l'épaisseur de la feuille de Cu. Pour les feuilles de 10 μm d'épaisseur, l'effet des GNSs se manifeste après le frittage des échantillons à des températures élevées (> 700 °C). Au lieu de créer beaucoup de contraintes à l'expansion des feuilles de Cu adjacentes, les GNSs ont fonctionné comme une barrière empêchant la pénétration des grains de Cu développés, entraînant la stabilisation de la texture de recristallisation représentée par les deux composantes tournées.

Pour le composite Cu/GNS avec une épaisseur de Cu de 30 μm, les résultats ont montré qu'une forte orientation Cube était produite dans le composite Cu/GNS au lieu des orientations individuelles non Cube dans l'empilement de Cu pur sans GNSs. Une analyse détaillée de l'état de déformation de Cu dans le composite Cu/GNS a révélé que le comportement d'expansion anisotrope du GNS qui est incompatible avec celui de Cu imposait de multiples contraintes élastiques aux feuilles, entraînant un état isocontrainte biaxiale dans la couche en surface et un état de déformation en compression uniaxiale dans la couche centrale. L'anisotropie élastique du Cu favorise la croissance des grains orientés Cube pour minimiser l'énergie totale de déformation.

Les résultats du présent travail fournissent des informations quantitatives détaillées sur la recristallisation de feuilles de Cu et de composites stratifiés, ce qui contribue à approfondir la compréhension du comportement de recristallisation des matériaux 2D.

Mots clés: Texture de recristallisation; Croissance des grains; Matériaux 2D; Composite; Énergie de déformation élastique; Énergie de surface.

List of the frequently-used abbreviations

EPD	Electrophoretic depostion
RD	Rolling direction
ND	Normal direction
TD	Transverse direction
GNS	Graphene nanosheet
XRD	X-ray diffraction
SEM	Scanning electron microscope
EBSD	Electron backscatter diffraction
TEM	Transmission electron microscope

Contents

Abstract ..... **I**

Résumé ..... **III**

List of the frequently-used abbreviations ..... **V**

Contents ..... **VII**

Chapter 1 Literature review **1**

1.1 General introduction 1

1.2 Driving factors 2

1.2.1 Stored energy driven nucleation 2

1.2.2 Grain growth 3

1.3 Orientation features 4

1.4 Characterization techniques 7

1.5 2D Materials 9

1.6 Main contents of this work 10

Chapter 2 Experimental and calculation methods **14**

2.1 Experimental details 14

2.1.1 Microstructure characterization 14

2.1.2 Texture characterization 14

2.1.3 *In-situ* Lattice strain characterization 16

2.2 Crystallographic calculations 18

2.2.1 Coordinate system 18

2.2.2 Euler angles 19

2.2.3 Coordinate transformation 21

2.2.4 Misorientation 22

2.2.5 Stereographic projection 24

2.2.6 Trace analysis method 25

2.2.7 Twinning elements in FCC lattice 26

Chapter 3 Fabrication of the GNS/Cu composites 28

3.1 Raw materials 28

3.2 Fabrication method 29

3.2.1 Electrophoretic deposition (EPD) of the GNS 29

3.2.2 Vacuum hot-pressing sintering and heat treatment 33

3.3 Summary 34

Chapter 4 Recrystallization texture evolution of cold-rolled Cu foils governed by microstructural and sample geometrical factors during heating 36

4.1 Introduction 36

4.2 Experiments 36

4.3 Results 37

4.3.1 Texture and microstructure of cold-rolled Cu foils 37

4.3.2 Texture evolution during heating 39

4.3.3 Microstructure and orientation evolution during heating 42

4.4 Discussion 52

4.4.1 Effect of deformation stored energy 52

4.4.2 Effect of biaxial elastic strain energy and surface energy 53

4.4.3 Effect of interface mobility 58

4.5 Summary 59

Chapter 5 Effect of GNS on recrystallization texture evolution of Cu/GNS composite with Cu foil thickness of 10 μm 62

5.1 Introduction 62

5.2 Experiments 62

5.3 Results and discussions 63

5.3.1 Texture and microstructure evolution of Cu/GNS during heating 63

5.3.2 Effect of GNS on the lattice strain evolution of Cu foils 69

5.4 Summary 71

Chapter 6 Elastic Strain Induced Abnormal Grain Growth in laminated Cu/GNS composites 74

6.1 Introduction 74

6.2 Experiments 74

6.3 Results 75

6.3.1 Initial microstructure and texture of as-cold-rolled Cu foil 75

6.3.2 Microstructure and texture of as-sintered pure Cu and Cu/GNS 76

6.3.3 Microstructure and orientation evolution of pure Cu and Cu/GNS during heating 78

6.3.4 Thermal expansion of Cu and Cu/GNS during heating and relative lattice strains induced by GNS 80

6.4 Discussion 84

6.4.1 Incompatible thermal expansion induced elastic strain states in Cu foil 84

6.4.2 Orientation dependent elastic strain energy density of strained crystals 86

6.5 Summary 91

Chapter 7 Conclusion and Perspectives 94

7.1 Conclusions 94

7.2 Perspectives 96

Reference 98

Publication list 107

I: Publications in international journals 107

II: Contributions to International Conferences 109

Acknowledgement 110

Chapter 1 Literature review

1.1 General introduction

Crystallographic texture is one of the most important parameters affecting the anisotropic material properties. On the one hand, materials with strong texture are highly desired, since the as-fabricated products could possess outstanding mechanical or physical properties in certain crystallographic orientations. For example, Cube ({100}<001>) or Goss ({110}<001>) texture is highly desired in electrical steels because it possesses superior magnetic property in the <100> crystallographic direction [1, 2]. On the other hand, texture should be avoided in some materials in order to obtain uniform plastic deformation properties. The most well-known example is the fabrication of beverage cans using aluminium sheets by deep drawing [2]. The un-desired 'ears' would be produced on the edge of the cans due to the texture of the aluminium sheet. Therefore, for various purposes, despite the necessities to promote or to avoid the formation of texture in a certain material system, great effort should be taken in related investigation in order to reveal the underlying texture formation mechanisms.

In general, texture is produced mainly through two ways, i.e., by plastic deformation or by recrystallization of cold-deformed materials. For deformation texture, it is normally classified and named according to the deformation method. There are mainly three types of deformation texture:

1. Fiber texture produced by uniaxial compression or drawing [3];
2. Rolling texture produced by rolling [4];
3. Torsion texture produced by simple shear [5, 6].

Recrystallization texture is another important branch generated by microstructure evolution of cold-deformed metallic materials during thermal treatment. It is mainly produced through two processes, i.e., recrystallization and subsequent grain growth. Both the two processes play an important role determining the final form of the recrystallization texture. Recrystallization is a thermally activated microstructure evolution process, whereby new strain-free grains emerge from the deformed matrix and consume the deformed matrix until all the

sample is replaced with recrystallized strain-free grains. In the literature, a great amount of researches focus on explaining the mechanisms controlling the transformation of as-deformed state texture components into the recrystallized ones. Until now, there is still no consensus about the route how the as-deformed state texture components are transformed. On the contrary, controversial results are always obtained in different material systems. In the past decades, about this subject, many theories have been proposed and two of them stood out, i.e., the 'oriented nucleation' (ON) [7, 8] theory and the 'oriented growth' (OG) theory [9, 10]. The ON theory claims that the recrystallization texture is dominated by the orientations of the nuclei formed during the primary recrystallization process. In another word, the orientation distribution of the new recrystallized grains is not random. It always possessses specific orientation relationship (OR) with the deformed matrix. Thus, the growth of the produced nuclei highly determines the final recrystallization texture. As for the OG theory, it argues that the orientations of the primary nuclei are random, however, there exist special OR between the deformed matrix and some of the recrystallized grains. The grain boundaries of these grains possess higher mobility than the other grains. According to the results of many researches [11-13], it is well accepted that these new recrystallized grains possess a 30°~40°/<111> OR with respect to the neighboring deformed matrix in some FCC metals. In this way, after the grain growth process, the orientation of the recrystallization texture is dominated by the orientation of these grains with high growth rate.

1.2 Driving factors

Recrystallization and subsequent grain growth are driven by eliminating the high energy features like point defects, dislocations and grain boundaries accumulated during the cold-deformation process. During each specific recrystallization stages like nucleation, primary grain growth and secondary grain growth, the corresponding driving force differs.

1.2.1 Stored energy driven nucleation

Nucleation is mainly driven by the need to reduce the deformation stored energy. As an indicator for plastic deformation stored energy, Taylor factor could be regarded as a measure for the orientation dependent driving force for recrystallization. It could be calculated as [14]:

$$M = \frac{\sum_{i-1}^{s} \tau_0 |d\gamma_i|}{\sigma_0 d\varepsilon_{vM}}, \quad (1.1)$$

where τ_0 is the critically resolved shear stress, $d\gamma_i$ is the instantaneous slip increment on slip system i, s is the number of active slip systems, σ_0 is the flow stress and $d\varepsilon_{vM}$ is the von Mises equivalent strain.

About this domain, a great amount of investigations have been conducted and two main theories are well accepted, i.e., the 'high stored energy driven nucleation' [15] and 'low stored energy driven nucleation' [16]. The former claims that nucleation occurs preferentially at regions with high deformation stored energy. In other words, the crystals in orientation with the highest Taylor factor are favored for nucleation which contributes to a recrystallization texture dominated by high Taylor factor orientations. With higher Taylor factor, a crystal will accumulate more dislocations during deformation. If a dislocation-free nucleus is formed in such region, more deformation stored energy is released.

Because nucleation happens with the appearance of new dislocation-free grains, many researchers are in favor of the 'low stored energy driven nucleation' theory which claims that the nuclei are preferred to form in the low stored energy region, i.e., deformed matrix with low Taylor factor. In many investigations, a great amount of Cube oriented nuclei with low Taylor factor were observed and resulted in strong Cube recrystallization texture [1, 17, 18]. According the reference, there exist two kinds of dislocations possessing vectors perpendicular to each other in the Cube oriented grains. In this way, during the plastic deformation process, the two kinds of dislocations do not pin each other which contribute to a low dislocation density in the Cube orientated deformed grains. As a result, the sub-grains in the Cube oriented deformed grains will work as the nucleus during the recrystallization process because of the low dislocation density. In summary, the special dislocations in the Cube grains lead to easy recovery of the deformed Cube grains and contribute to preferred nucleation of Cube oriented nuclei.

1.2.2 Grain growth

When the recrystallization process is complete, the microstructure of the deformed sample is replaced by the strain-free new grains. However, grain coarsening will continue because of the

energy stored in the grain boundaries. The subsequent grain growth will be driven by the decrease of this energy and consequently influence the final annealing texture. Sometimes, this process plays a more important role in determining the final annealing texture than the recrystallization process since selective grain growth may happen during this process.

The post-recrystallization grain growth could be classified into two types, normal and abnormal grain growth. The driving force for the former is the energy stored in grain boundaries while the abnormal grain growth could be induced by various factors like stress, magnetic field, surface and interface energy, strain energy, etc [19-21]. For instance, Park et al [22] investigated the effect of film thickness on the evolution of annealing texture in sputtered Cu films. The results showed that the <111>//ND fiber texture was produced when the thickness of Cu film is 100 nm while the <100>//ND fiber texture formed when the Cu film thickness is 480 nm. The formation of the two kinds of texture is explained to be driven by the minimization of the surface energy and strain energy of the total system, respectively.

1.3 Orientation features

Rolling is commonly employed for sheet forming. The obtained rolling texture highly depends on the intrinsic material characters like stacking fault energy (SFE) and the deformation parameters like deformation temperature and rolling reduction [23]. Among all the factors, SFE is the most important one. For example, cold-rolling of pure Cu normally produce Cu-type (as shown in **Fig. 1-1a**) rolling texture while the Cu-Zn (70:30) alloy generate Brass-type (as shown in **Fig. 1-1b**) texture by rolling. The typical 111 pole figures of the two type texture are displayed in **Fig. 1-1**.

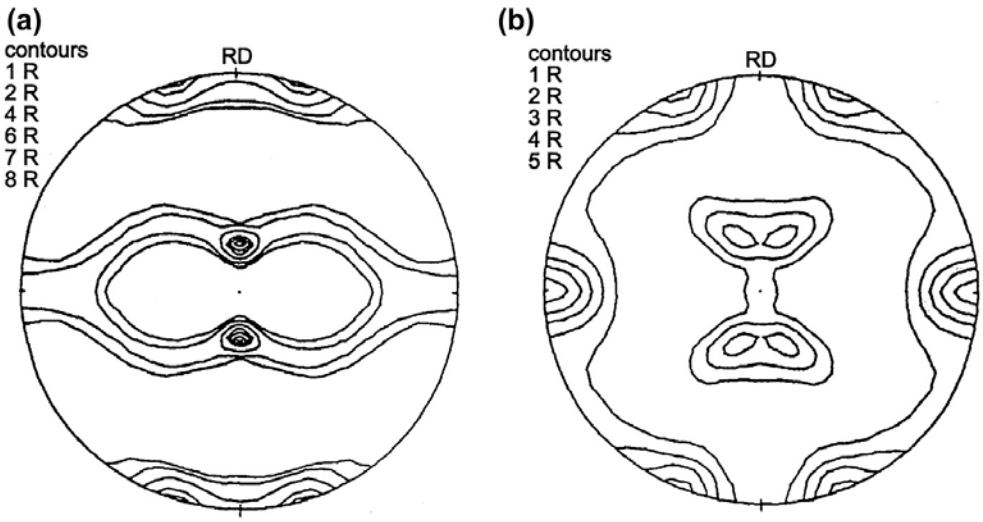

Fig. 1-1. Typical 111 pole figures of 95 % cold-rolled (a) pure Cu and (b) 70:30 brass [24].

In this work, the raw Cu foils were fabricated by cold-rolling. The rolling texture of pure Cu consists mainly of several texture components like the Copper ({112}<111>), the S ({123}<634>), and a relatively weak Brass ({110}<112>) component. The Miller indices and the Euler angles of these components and the other common texture components in rolled and recrystallized FCC metals are summarized in **Table 1-1**.

Table 1-1. Typical fibers and texture components in FCC metals [23].

Components	**Miller indices**	**Euler angles**		
		φ_1	Φ	φ_2
Copper	{112}<111>	90	35	45
S	{123}<634>	59	27	63
Brass	{110}<112>	35	45	0
Goss	{110}<001>	0	45	0
Cube	{100}<001>	0	0	0

Fiber	**Description**
α	<110>//ND
β	From Copper to Brass through S
θ	<100>//ND
γ	<111>//ND
τ	<110>//TD

Because of deformation, the texture components spread out from their ideal orientations. Thus, in many cases, they do not appear as individual points or spheres in the orientation space but as a continuous tubes. We can call the axial lines of the tubes the skeleton line of the texture, and such texture could be finely displayed by a tube in the Euler space as shown in **Fig.1-2**. This fiber is commonly called beta (β) fiber, which connects the three rolling texture components from the Copper ({112}<111>) to the Brass ({110}<112>) through the S({123}<634>).

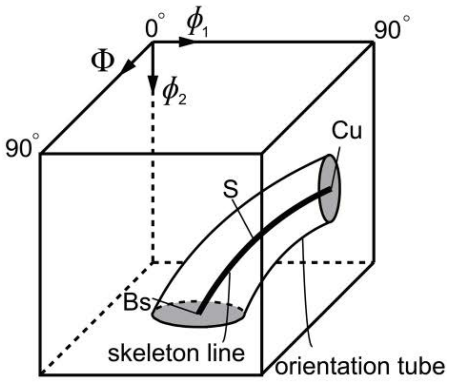

Fig. 1-2 Orientation tube and skeleton line for the β fiber texture in the Euler space [25].

For face centered cubic (FCC) metals and alloys of medium to high stacking fault energy (SFE), the recrystallization texture usually consists of a strong cube texture {100}<001> (as shown in **Fig. 1-3**). When the SFE of Cu is decreased, for example, by alloying elements like Al, Be, Cd, Mg, Ni, P, Sb, Sn, Zn, etc., [26] mirror orientations of the Cu component would appear. Thus, the intensity of the Cube texture component in the recrystallized Cu will be weakened by decreasing the SFE value.

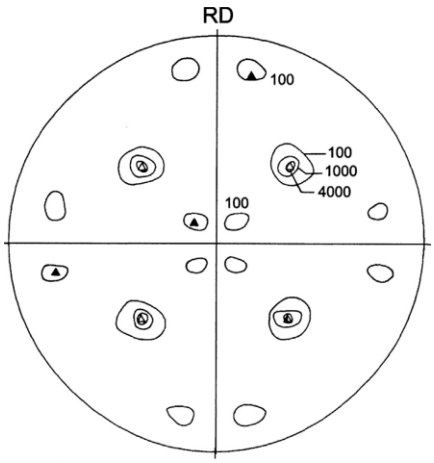

Fig. 1-3 111 Pole figure of 97% cold-rolled Cu annealed at 200°C. Open symbols indicate the ideal "Cube" orientation {100}<001> and filled symbols {122}<212> the 'twin' orientation [27].

1.4 Characterization techniques

Characterization techniques for microstructure observation and texture measurement of crystalline materials have been improving with the advance of materials science. The optical microscope (OM) is firstly used for microstructure observation at early ages. It is built up through the combination of an array of lens and using the visible light to generate the magnified micrograph of small objects. It is almost the easiest way to possess the first impression of the material microstructure, but, at the same time, has many limitations. For instance, normally, maximum magnification of around 1000× could be reached by OM due to the limited power of visible light. Although modern OM has already broken this limit, the magnification is still far less than a typical scanning electron microscope (SEM). In addition, crystallographic orientation information of the investigated sample is not accessible with an OM.

In order to investigate the texture evolution of cold-deformation material during thermal treatment, texture analysis of different states of sample is necessary.

X-ray diffraction is the most established technique for macrotexture measurement. The basic mechanism follows the Bragg's law:

$$2d\sin\theta=n\lambda, \tag{1.1}$$

where d is the inter plannar spacing of the diffracting planes, θ is the incident angle, n is any integer, and λ is the wavelength of the beam.

The electron of the atoms in a crystalline sample scatter the incident X-ray elastically and then generate diffraction patterns employed for texture analysis. However, because of the high absorption of X-rays in matter (mass absorption coefficient in the range of 100 $cm^2 \cdot g^{-1}$ [28]), the penetration of X-ray in material is limited to layers of 10 ~ 100 μm. Thus, when the thickness of a sample is larger than 100 μm, the bulk texture of the investigated sample is not available through this method.

Neutron diffraction can also be used to measure the macrotexture of crystalline samples. With the small mass absorption coefficient (in the range of 0.01 $cm^2 \cdot g^{-1}$ [28]), the penetration depth of neutron in the investigated sample is around 4 orders higher than that of

X-ray, which makes it possible to measure the bulk texture of big samples. Thus, it is really a good technique for texture measurement of samples with large grain sizes. However, large facility is required for producing neutrons (nuclear reactor), which means they are used for texture measurement when specific advantages is offered by neutron over X-rays.

Because of the low penetration depth (less than 1μm) and small interaction volume of electron, the impletion of electron diffraction allows to obtain the diffraction information from discrete sample volumes that are submicron in size together with images of the same region. In this way, orientation of individual grain (microtexture) is accessible and correlation between microstructure and orientation could be established. The representative application of electron diffraction is transmission electron microscope (TEM) and SEM. As shown in **Fig. 1-4** [25], when the incident electron beam interacts with the investigated sample, a variety of different electron and X-ray signals are produced. With these generated signals, microstructure, chemical composition and crystallographic orientation of the investigated sample volume could be analyzed.

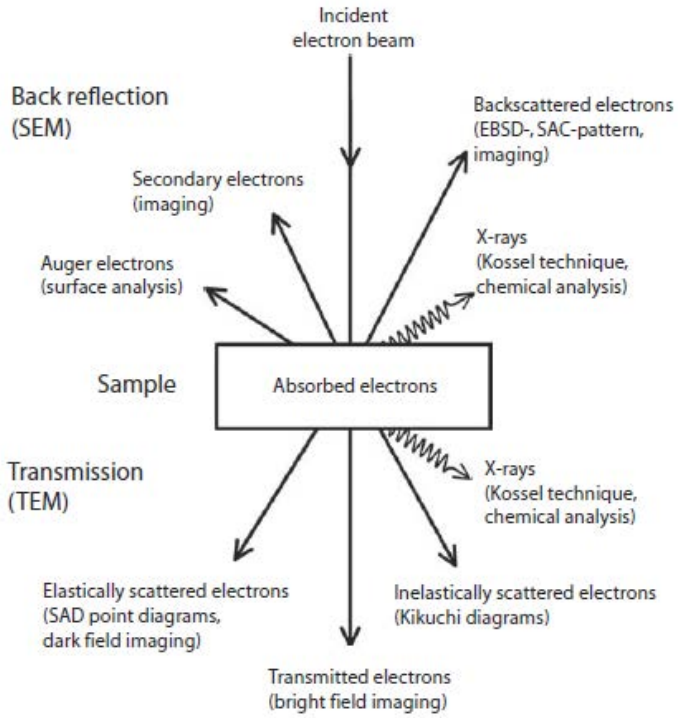

Fig. 1-4 Produced signals by interaction between the incident electron beam and the investigated sample [28].

Clearly, all the employed techniques either for microstructure characterization or texture measurement has its merits and drawbacks. In order to analyze the recrystallization behavior of cold-deformed metallic metals, especially the texture evolution, correlation between the microstructure evolution and texture evolution should be established and quantitative information about the orientation of the nuclei and the recrystallized grains should be characterized.

1.5 2D Materials

Nowadays, minimization of commercial product makes the 2D materials highly demanded. Thus, the recrystallization behavior of 2D materials should be clarified to support better application. In the literature, investigations on recrystallization of thin films mainly have been concentrated on deposited Ag, Cu, Ni and Al films [21, 22, 29-32]. With the similar dimension, their recrystallization features may help to understand and study the recrystallization of 2D free standing films.

For a polycrystalline thin film deposited on a single crystal substrate, the surface energy plays an important role in determining the final recrystallization texture, especially when the grain size of the thin film is larger than the film thickness. During the recrystallization process of this kind of film, abnormal grain growth always occur instead of the normal grain growth because of the anisotropy of surface and interface energy. The abnormal grain growth induced by this energy is normally called Surface-Energy-Driven secondary grain growth (SEDSGG), and this phenomenon has already been observed in many materials [21, 22, 31, 33]. For FCC materials, the surface energy is anisotropic for different crystallographic planes. For example, for {100}, {110} and {111} planes, the surface energy of the {111} planes are the smallest, and the {110} planes the highest. Thus, for thin films with FCC structure, grains with {111} planes parallel to the film plane should be favored during the grain growth process in order to minimize the total surface energy.

Except for surface energy, the strain energy should also be taken into consideration when investigate the grain growth process of deposited thin films. Several types of strain can be generated in the film. The growth strain can be developed inside the material by defects like vacancies, impurity atoms, dislocations and micro cracks. Moreover, epitaxial strain could arise

due to the mismatch between the film and its substrate. The produced epitaxial strain could be described by the following equation [21]:

$$\varepsilon_{epitaxial} = (a_s - a_f)/a_s. \quad (1.2)$$

Where a_s and a_f are the lattice parameters of the substrate and the film.

One kind of important epitaxial strain is the thermal strain which arise because of the different thermal expansion coefficient (TEC) between the substrate and the attached film. Because the thin films deposited on the substrate are usually deposited at temperatures different from the temperature when grain growth occurs. Thus, a biaxial strain will arise when the film and the substrate are annealed at temperatures higher than the deposited temperature because they possess anisotropic TEC values. This thermal strain can be calculated by [20, 31, 33]:

$$\varepsilon_{thermal} \cong (T_{gg} - T_{dep})\cdot(\alpha_s - \alpha_f), \quad (1.3)$$

where α_s and α_f are the isotropic TEC values of the substrate and film, respectively, and T_{gg} and T_{dep} are the grain growth and deposition temperatures, respectively.

Since the strain energy density is given by $\sigma \cdot \varepsilon$, where σ and ε are the strain and stress, respectively. When upon annealing, the biaxial strain arise from different TEC values between the substrate and film and is equally subjected by each grain regardless of their orientations. Thus, because of the anisotropic biaxial elasticity of certain metals, such as Cu, the strain energy of distinctly oriented grains differs. Thus, to minimize the total strain energy, abnormal grain growth of grains with the lowest strain energy will occur when the film is subjected to a biaxial elastic strain.

For thin film with certain thickness, since the strain energy density is not film thickness dependent. When the film thickness is below a certain threshold value, the strain energy together with the surface energy dominates the driving force and lead to abnormal grain growth of grains which minimize the total free energy of the system.

1.6 Main contents of this work

In some industrial application fields such as conductive base of large resistance welding machine, resistance welding machine electrode and lead frame, materials with both high

strength and electrical conductivity are in great demand. Cu possesses outstanding electrical conductivity than other metals but the specific strength is out high enough especially at increased temperature. In order to strengthen Cu, one effective method is to fabricate Cu matrix composite reinforced with strong reinforcements. Ideally, the reinforcements should also possess high electrical conductivity so that the super electrical properties of Cu could be maintained. Graphene is an ideal reinforcement for metal matrix composites because of their superior mechanical performance as well as outstanding in-plane thermal and electrical conductivities. Thus, many researches have been conducted to fabricate graphene or graphene nanosheets (GNSs) reinforced Cu matrix composites with the purpose to increase the mechanical performance of pure Cu while maintain the physical properties. The laminated GNS reinforced Cu matrix composite (GNS/Cu) is one of these materials.

In the literature, many investigations have been conducted related to the recrystallization of cold-deformed bulk FCC metals [2, 17, 23, 34]. However, the recrystallization features of thin Cu foils have not well been analyzed. Moreover, recrystallization behavior of graphene nanosheets (GNSs) reinforced Cu matrix laminated composites is a new domain and has not been investigated yet. Thus, the current work is designed to investigate the recrystallization behavior of thin Cu foils (thickness of 10 μm and 30 μm) and the effect of deposited GNSs on the recrystallization features of the Cu/GNS composites. The Cu/GNSs composites with different Cu layer thicknesses (10 μm and 30 μm) were sintered by vacuum hot-pressing sintering method. The nucleation, recrystallization, normal and abnormal grain growth processes were studied systematically by means of SEM-EBSD for microstructure observation, neutron and synchrotron radiation diffraction for texture measurement and *in-situ* 4D synchrotron radiation diffraction for lattice strain evolution characterization.

Recrystallization of Cu foils with thickness of 10 μm was investigated systematically from nucleation features to post-recrystallization grain growth. For the nucleation stage, the nucleation sites and the orientation features of the produced nuclei were studied in detail. For each stage (nucleation, primary growth of nuclei and post-recrystallization grain growth), the dominant factor is analysed. Annealing twin produced during the recrystallization process is

believed to introduce new orientations into the material. In this work, the contribution of the annealing twin to the final recrystallization texture is also investigated.

For the recrystallization of Cu/GNS composites, the effect of GNS on the recrystallization behavior of Cu foils is studied. On the one hand, the new GNS-Cu interfaces may play an important role during the nucleation process and thus affect the final recrystallization texture. Moreover, the incompatible thermal expansion coefficient (TEC) between Cu and GNS may produce certain thermal strain in the Cu layer. The thermal expansion mismatch induced strain and the effect of this strain on the growth of the recrystallized grain will be figured out and the strain energy effect in determining the final recrystallization texture will be revealed.

The results of this PhD work could provide detailed and quantitative information on the recrystallization of thin Cu foils. Moreover, with the cold-rolled thin Cu foils as the model material, the multiple intrinsic microstructural and extrinsic sample geometrical factors make it possible for us to revisit the recrystallization of cold-deformed FCC materials. The revealed mechanisms will help to deepen our understanding on recrystallization. It should be noted that the microstructure and texture evolution of the samples in this work was analyzed from micro-meso scale by means of SEM-EBSD to macrocopic scale by means of neutron and synchrotron radiation diffraction. Besides, a 4D synchrotron radiation technique is employed to study the lattice strain evolution of the samples during heating. Moreover, the obtained experimental results will be analyzed in the frame of crystallography. These advanced characterization techniques and the combined crystallographic analysis yield reliable and meaningful results.

Chapter 2 Experimental and calculation methods

2.1 Experimental details

2.1.1 Microstructure characterization

The mesoscale microstructural features of the pure Cu and the GNS/Cu samples (details of the fabrication process is detailed in Chapter 3) at the states of as-cold-rolled, as-fully-sintered and as-heated to different temperatures (partially sintered) were characterized by scanning electron microscopy - electron backscatter diffraction (SEM-EBSD), using a JEOL 6500F SEM equipped with an EBSD acquisition camera and the Aztech online acquisition software package (Oxford Instruments).

The EBSD samples were prepared with different method for different foil thickness. For Cu foils with thickness of 30 μm. They were firstly mechanically polished with wet grit silicon carbide sandpaper up to #4000, and then electro polished with a solution of 20% nitric acid and 80% methanol at a temperature lower than 15 °C at a voltage of 10 V for 5 s. When the thickness of Cu foil is 10 μm, the EBSD samples for ND plane measurements were prepared with the same method for TEM sample. The samples were directly electro-polished in a solution of 20% nitric acid and 80% methanol at a voltage of 8 V and at temperatures lower than -28 °C, using a Struers Tenupol-5 twin-jet electropolisher. Specially, for copper foils deposited with GNSs, the GNSs were carefully removed by mechanical polishing before performing the electro-polishing to avoid the nonuniform polishing caused by the deposited GNSs.

The EBSD measurements were conducted automatically under the beam controlled mode with a step size of 70 nm for the as-cold-rolled and the as-heat-treated samples and of 0.35 μm for the as-fully-sintered samples. The measurement results were analyzed with the Channel 5 (Oxford Instruments) and the homemade ATEX [35] software packages.

2.1.2 Texture characterization

The texture of the pure Cu and the GNS/Cu samples at the states of as-cold-rolled, as-fully-sintered and as-heated to different temperatures were measured by neutron diffraction at the diffractometer STRESS-SPEC located at FRM II (Heinz Maier-Leibnitz Zentrum (MLZ), Garching, Germany), and by synchrotron radiation at the P07 beam line at Petra III (Deutsches

Elektronen-Synchrotron (DESY), Hamburg, Germany). For the texture measurements by neutron diffraction, The PG (002) monochromator was selected to produce neutrons with dual-wavelengthes of 1.11 and 1.65 Å. The (111), (220) and (200) diffraction patterns were recorded at $2\theta = 51°$ with a detector window of about 15°. Samples with dimensions of 4mm×4mm×2mm were fully immersed in the incident beam (beam size of Φ 8 mm). The experimental setup is illustrated in **Fig. 2-1**. During the texture measurement, the samples were rotated around two perpendicular axes in order to measure the complete diffraction patterns, i.e., orientation around the TD of the cold-rolled sample (defined as Chi tilting) and rotation around the ND of the sample (defined as Phi rotation). For the Chi tilting, the samples were tilted from 0° to 90° with an interval of 15°. At each Chi angle, the sample rotate around the ND of the sample (0°~360°) and the diffraction pattern were recorded at every 5°. As a result, 72 diffraction pattern images were recorded at each Chi angle to calculate the complete pole figure. The software StressTextureCalculator (SteCa2-2.0) [36] was used to extract the pole figure intensity data. The detailed experimental parameters are list in **Table 2-1**.

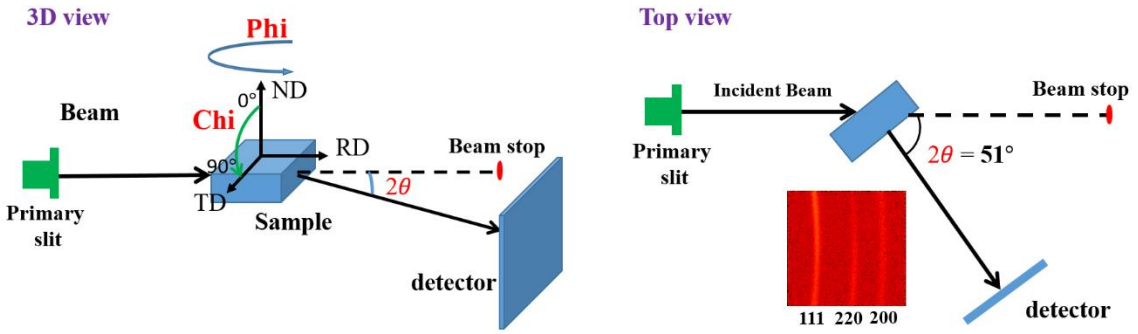

Fig. 2-1 Experimental setup of texture measurement by neutron diffraction.

Table 2-1 Experimental parameters of texture measurement by neutron diffraction.

Wavelength (Å)	Sample to detector distance (mm)	Pixel size (mm)	Slit size (mm)	2θ (°)
1.11; 1.68	1035	1	Φ8	51

For the texture measured by synchrotron radiation diffraction, since the full Debye-scherrer ring could be recorded during the measurement, only on sample rotation, around ND, was needed, as displayed in **Fig. 2-2**. The Debye-sherrer rings of each sample were recorded by the

detector (Perkin Elmer XRD 1621) behind the sample because of the transmission diffraction geometry. For texture measurement of each sample, the samples rotated around the ND of the sample from -90° to 90° with an interval of 5° (37 images were recorded). At each position, the exposure time was set to be 4 seconds to allow the detector to record sufficient diffraction signals. The incident X-ray beam possess the wavelength of 0.14235 Å, and the sample to detector distance was set to be 1688 mm, which allowed the detector to record the (111), (200) and (220) Debye-scherrer rings of Cu. The detailed experimental parameters are summarized in **Table 2-2**.

For the calibration of the misalignment of the detector, a standard LaB_6 powder sample (with a thickness of 5 mm in the beam direction) diffraction data was recorded under the identical experimental conditions at room temperature. The software StressTextureCalculator (SteCa2-2.0) [36] was used to extract the pole figure intensity data.

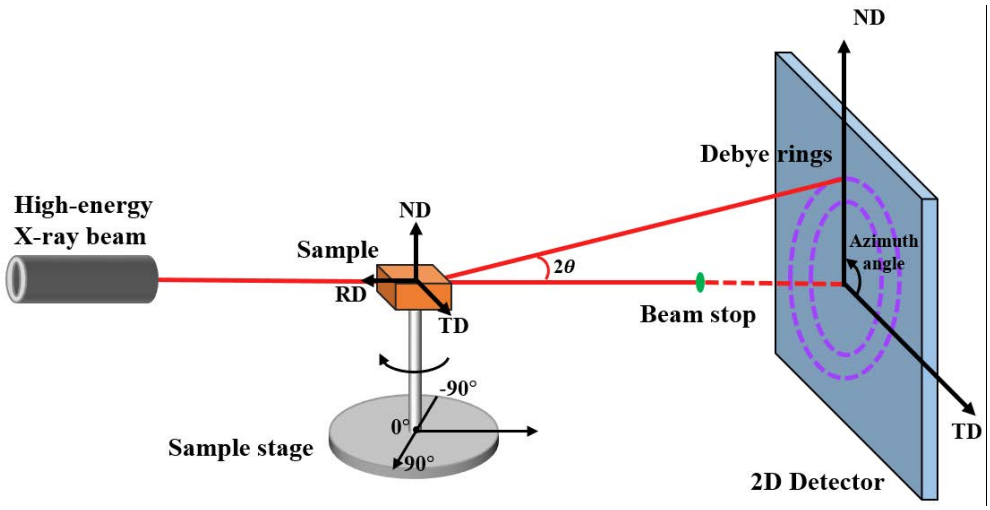

Fig. 2-2 Experimental setup for texture measurement by synchrotron radiation diffraction.

Table 2-2 Experimental parameters of texture measured by synchrotron radiation.

Beam energy (KeV)	Wavelength (Å)	Sample to detector distance (mm)	Pixel size (mm)	Beam size (mm)	Rotation angle range (°)
83	0.14235	1688	0.2	0.7×0.7	-90 ~ 90

2.1.3 *In-situ* Lattice strain characterization

In order to examine the lattice strain evolution during the heating process, the *in-situ* synchrotron radiation diffraction experiments were performed at the P07-HEMS beamline operated by the Helmholtz-Zentrum Geesthact at PETRA III (Deutsches Elektronen-Synchrotron (DESY), Hamburg, Germany) with the assistance of a DIL805A/D dilatometer [37]. The principal experimental parameters are summarized in **Table 2-3**. The misalignment of the detector and the instrumental broadening were calibrated using a standard LaB_6 powder sample. Specifically, in order to subtract the instrumental broadening from the observed profile, the standard LaB_6 powder diffraction data was recorded under the identical experimental condition at room temperature. After that, the diffraction data for the standard LaB_6 powder was calibrated by the Maud software package [38-40] to deduce the instrumental values so that the instrumental broadening could be excluded at different Bragg angles.

During the measurement, the as-cold-rolled pure Cu samples and the GNS/Cu composite samples each was heated from the ambient temperature (< 28 °C) to 950 ℃ at a heating rate of 5 ℃·min^{-1}, then cooled in an argon flow in a dilatometer (DIL 805A/D). A slight compression was applied along the ND to fix the sample in place in the dilatometer during the measurement process. The incident beam was set to be parallel to the TD of the cold-rolled Cu foils. The geometrical configuration of the measurement layout is illustrated in **Fig. 2-3.** During the whole heating process, the full Debye-Scherrer rings were recorded at every 8 seconds. The measured 2D Debye-Scherrer patterns were processed using the FIT-2D [41] by which the Debye-Scherrer rings were integrated radially at selected azimuthal angles (**Fig. 2-3**) to yield 1D line diffraction patterns that were further analyzed using a homemade program, A-fit. The information contained in the peak profile, such as the integrated intensity (I), the Bragg angles (2θ) of the peaks and the full width at half maximum (FWHM) at each measured temperature were extracted.

For the fitting of the diffraction peaks, a Voigt profile (Pseudo-Voigt function) that results from the convolution of the Gaussian and the Lorentzian profile was used to mimic the exact Voigt function and to describe approximately both the instrumental and the intrinsic sample profiles.

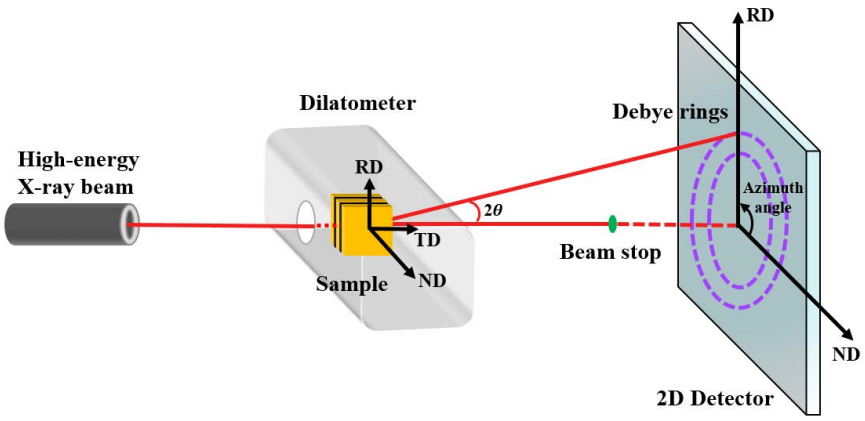

Fig. 2-3 Experimental setup of in-situ synchrotron radiation diffraction measurement.

Table 2-3 Experimental parameters and devices of in-situ synchrotron radiation diffraction measurement.

Energy [42]	Wavelength [Å]	Beamsize [mm^2]	Sample-Detector Distance [mm]	Acquisition time [s]	Detector	Dilatometer
103.3	0.12	0.8×0.8	1306.5	8	Perkin Elmer XRD 1621	DIL 805A/D

2.2 Crystallographic calculations

2.2.1 Coordinate system

In order to describe the orientation of a crystallite in a polycrystalline material, two coordinate systems are introduced, one set to the poloycrystalline sample and the other set to the crystallite, so that the orientation of the crystallite could be represented by the relative position relationship between the two coordinate systems. The most commonly used coordinate system is the Cartesian coordinate system or the orthonormal coordinate system of which the three basis vectors are unit vectors and perpendicular to one another. In this work, because Cu belongs to the face-centered cubic (FCC) crystal system, and the raw materials were deformed by cold-rolling, an orthogonal coordinate system was employed as the sample coordinate system (denoted x-y-z) with the x axis parallel to the rolling direction (RD) of the sample, the y axis parallel to the transverse direction (TD) and the z axis parallel to the normal direction (ND). An orthonormal coordinate system was employed as the crystal coordinate system (denoted i-j-k) with the i axis parallel to the [1 0 0] direction of the crystal, the j axis to the [0 1 0] direction and the k axis to the [0 0 1] direction.

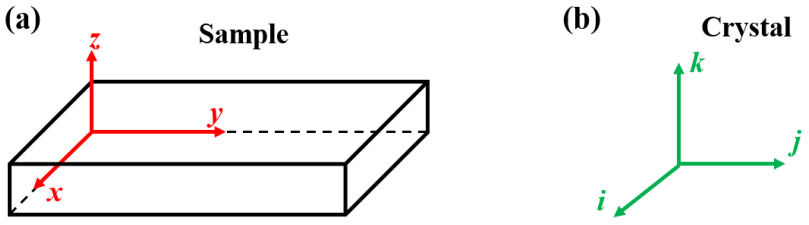

Fig. 2-4 Coordinate systems used in this work. (a) sample coordinate system and (b) crystal coordinate system.

2.2.2 Euler angles

The Euler angles are three rotation angles developed by Leonhard Euler {Evlero, 1776 #476} to describe relative orientation between two coordinate systems and thereby representing the crystal orientation. In our case, these three angles are used to describe the relative orientation between the sample coordinate system and the crystal coordinate system. The crystallographic orientation of a certain microstructural constituent in the sample could then be defined by the three angles and normally denoted $(\varphi_1, \Phi, \varphi_2)$.

Applying the three consequent rotations defined by the three Euler angles could transform the sample coordinate system to the crystal coordinate system, thereby defining the orientation of the crystal. There are serveal different ways of applying the rotations [43, 44], among which, the most commonly used is the notation of Bunge [43]. As shown in **Fig. 2-5**, the rotations are realized by three consecutive rotations around the *z*, x' and z'' axes with rotation angles of φ_1, Φ and φ_2, where the '*x*-*y*-*z*' represents the sample coordinate system S and the '*i*-*j*-*k*' the crystal coordinate system C.

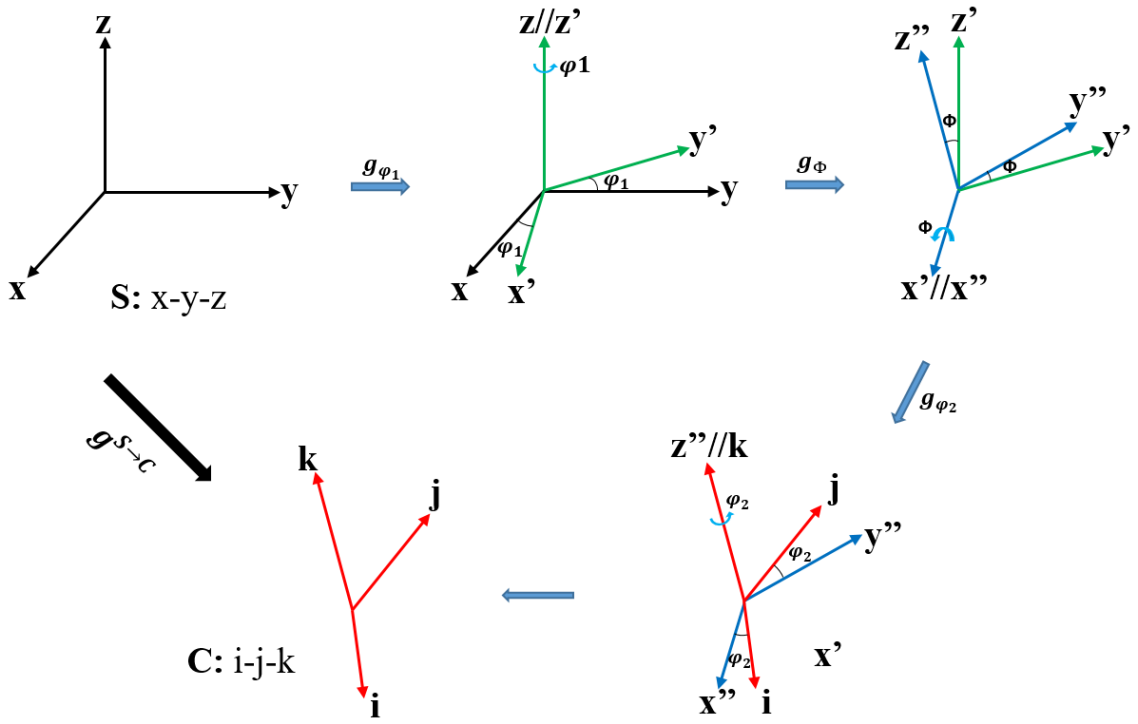

Fig. 2-5 Illustration of the three rotations in Bunge's notation. The sample coordination system S: 'x-y-z'; the crystal coordinate system C: 'i-j-k'.

When the rotations are written in terms of rotation matrices, for instance, the three rotations are represented in the matrix form as $\mathbf{g}_{\varphi_1}$, $\mathbf{g}_{\phi}$ and $\mathbf{g}_{\varphi_2}$, the rotation from the sample coordinate system S to the crystal coordinate system C ($\mathbf{g}^{s\to c}$) can be described as follows:

$$\mathbf{G}^{s\to c} = \mathbf{g}_{\varphi_1} \cdot \mathbf{g}_{\phi} \cdot \mathbf{g}_{\varphi_2} = \begin{pmatrix} g_{11} & g_{12} & g_{13} \\ g_{21} & g_{22} & g_{23} \\ g_{31} & g_{32} & g_{33} \end{pmatrix} \tag{2.1}$$

where

$$\mathbf{g}_{\varphi_1} = \begin{bmatrix} \cos\varphi_1 & \sin\varphi_1 & 0 \\ -\sin\varphi_1 & \cos\varphi_1 & 0 \\ 0 & 0 & 1 \end{bmatrix}$$

$$\mathbf{g}_{\phi} = \begin{bmatrix} 1 & 0 & 0 \\ 0 & \cos\phi & \sin\phi \\ 0 & -\sin\phi & \cos\phi \end{bmatrix}$$

$$\mathbf{g}_{\varphi_2} = \begin{bmatrix} \cos\varphi_2 & \sin\varphi_2 & 0 \\ -\sin\varphi_2 & \cos\varphi_2 & 0 \\ 0 & 0 & 1 \end{bmatrix}$$

and

$$g_{11} = \cos\varphi_1 \cos\varphi_2 - \sin\varphi_1 \sin\varphi_2 \cos\Phi$$

$$g_{12} = -\cos\varphi_1 \sin\varphi_2 - \sin\varphi_1 \cos\varphi_2 \cos\Phi$$

$$g_{13} = \sin\varphi_1 \sin\Phi$$

$$g_{21} = \sin\varphi_1 \cos\varphi_2 + \cos\varphi_1 \sin\varphi_2 \cos\Phi$$

$$g_{22} = -\sin\varphi_1 \sin\varphi_2 + \cos\varphi_1 \cos\varphi_2 \cos\Phi$$

$$g_{23} = -\cos\varphi_1 \sin\Phi$$

$$g_{31} = \sin\varphi_2 \sin\Phi$$

$$g_{32} = \cos\varphi_2 \sin\Phi$$

$$g_{33} = -\cos\Phi$$

2.2.3 Coordinate transformation

In the crystallographic concept, a vector is always expressed in different coordinate systems. Thus, it is really important to know how these coordinate systems are related to one another. Through coordinate transformation, we can express the same vector in different coordinate systems. As displayed in **Fig. 2-6**, a vector $\vec{V}$ is displayed in two coordinate systems (S_1: x-y-z and S_2: i-j-k). Thus, the same vector $\vec{V}$ is represented by different coordinates in the two systems, $[V_x,\ V_y,\ V_z]$ in system S1 and $[V_i,\ V_j,\ V_k]$ in system S_2. These two vectors could be related by a coordinate transformation matrix M between the two coordinate systems as expressed by Eq. (2-2).

$$\begin{bmatrix} \boldsymbol{x} \\ \boldsymbol{y} \\ \boldsymbol{z} \end{bmatrix}^{S_1} = M * \begin{bmatrix} \boldsymbol{i} \\ \boldsymbol{j} \\ \boldsymbol{k} \end{bmatrix}^{S_2} \tag{2.2}$$

The three basis vectors in the destiny coordinate system (S_2) could be expressed by the three basis vectors in the original coordinate system (S_1) by:

$$\boldsymbol{i} = a_{11}\boldsymbol{x} + a_{21}\boldsymbol{y} + a_{31}\boldsymbol{z}$$

$$\boldsymbol{j} = a_{12}\boldsymbol{x} + a_{22}\boldsymbol{y} + a_{32}\boldsymbol{z} \tag{2.3}$$

$$\boldsymbol{k} = a_{13}\boldsymbol{x} + a_{23}\boldsymbol{y} + a_{33}\boldsymbol{z}$$

So the coordinate transformation matrix M from S_1 to S_2 is as:

$$M = \begin{pmatrix} a_{11} & a_{12} & a_{13} \\ a_{21} & a_{22} & a_{23} \\ a_{31} & a_{32} & a_{33} \end{pmatrix} \tag{2.4}$$

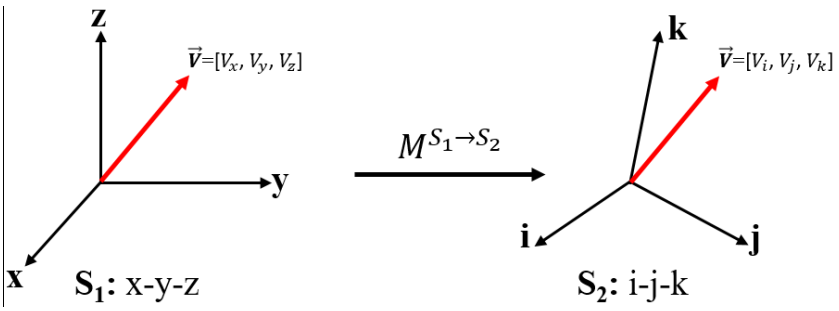

Fig. 2-6 Illustration of coordinate transformation of a vector between two coordinate systems S_1 ('x-y-z') and S_2 ('i-j-k').

2.2.4 Misorientation

Misorientation normally describes the relative orientation of two crystals with respect to each other. This orientation relationship (OR) could be represented as the OR of the coordinate systems of the two crystals (C1 and C2). As described in § 2.2.2, the orientation of a crystal could be represented by a rotation operation to rotate the sample coordinate system to coincide with the crystal coordinate system. Thus, the misorientation represented by coordinate transformation matrix between two crystals $\Delta \mathbf{g}^{C_1 \to C_2}$ could then be calculated, using the measured Euler angles of the two crystals, as illustrated in **Fig. 2-7**. Typically, the misorientation is expressed in the angle-axis representation, (θ, d). The angle-axis pair is then calculated.

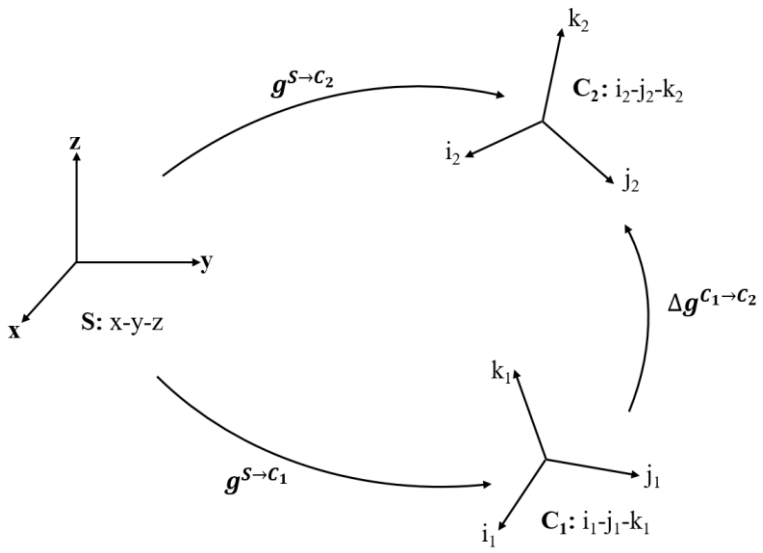

Fig. 2-7 Schematic of misorientation between two crystal coordinate systems C1 and C2, via the sample coordinate systems. 'x-y-z' is the sample coordinate system S. 'i1- j1- k1' and 'i2- j2- k2' are the crystal coordinate systems C1 and C2, respectively. $g^{S\to C_1}$ and $g^{S\to C_2}$ are rotation matrices from the sample coordinate system S to the Cartesian coordinate systems of the two crystals C1 and C2. $\Delta g^{C_1\to C_2}$ is the misorientation matrix between the two crystals C1 and C2.

The misorientation matrices $\Delta g^{C_1\to C_2}$ can be expressed with Eq. (2-5).

$$\Delta g^{C_1\to C_2} = (S_i)^{-1} \times (g^{S\to C_1})^{-1} \times g^{S\to C_2} \times S_j \tag{2.5}$$

where S_i and S_j are the rotational symmetric matrices of crystal C_1 and C_2, respectively, $g^{S\to C_1}$ and $g^{S\to C_2}$ represent the rotation matrices from the sample coordinate system S to the crystal coordinate systems of crystals C_1 and C_2. In the matrix form, the misorientation matrix ($\Delta g^{C_1\to C_2}$) is shown as follows:

$$\Delta g^{C_1\to C_2} = \begin{pmatrix} g_{11} & g_{12} & g_{13} \\ g_{21} & g_{22} & g_{23} \\ g_{31} & g_{32} & g_{33} \end{pmatrix} \tag{2.6}$$

With the as-calculated misorientation matrix, the rotation angle could be calculated as below:

$$\theta = arc\,cos((g_{11} + g_{22} + g_{33} - 1)/2) \tag{2.7}$$

For the rotation axis d [d_1, d_2, d_3], when the rotation angle is not the multiple of π, it could be calculated from the elements of the misorientation matrix as follows :

$$d_1 = \frac{g_{23} - g_{32}}{2\sin\theta}$$

$$d_2 = \frac{g_{31}-g_{13}}{2\sin\theta} \quad (2.8)$$

$$d_3 = \frac{g_{12}-g_{21}}{2\sin\theta}$$

For special situations, for example, when the angle equals 0, d = [1 0 0]. When the angle is the multiple of π, the misorientation axis d is calculated as follows :

$$d_1 = \pm\sqrt{(g_{11}+1)/2}$$

$$d_2 = \pm\sqrt{(g_{22}+1)/2} \quad (2.9)$$

$$d_3 = \pm\sqrt{(g_{33}+1)/2}$$

It should be noted that more than one axis-angle pairs could be obtained from the calculation because of crystallographic symmetry. However, all the as-calculated (θ, d) pairs are crystallographically equivalent.

2.2.5 Stereographic projection

The stereographic projection is often used to project a vector in a 3D space to a 2D plane for easy orientation display and comparison. As illustrated in **Fig. 2-8**, vector **OP** is a unit vector displayed in the unit sphere O-XYZ and intersects the sphere at P. The equatorial plane X-O-Y functions as the projection plane for projecting the vector. The as-projected point of point P (denoted P') is the intersection between the equatorial plane X-O-Y and the connection line between P and the south pole of the unit sphere.

The coordinates of P in the 3D coordinate system are (x_1, y_1, z_1) and the coordinates of P' on the projection plane X-O-Y are (x_2, y_2), respectively, and they satisfy the following mathematical relationship:

$$x_1^2 + y_1^2 + z_1^2 = 1$$
$$\frac{x_1}{x_2} = \frac{y_1}{y_2}$$

$$\tan\theta = \frac{\sqrt{x_1^2 + y_1^2}}{1+|z_1|} = \frac{\sqrt{x_2^2 + y_2^2}}{1}$$

$$\frac{x_1}{x_2} = \frac{y_1}{y_2} = \frac{\sqrt{x_1^2 + y_1^2}}{\sqrt{x_2^2 + y_2^2}} = \frac{1+|z_1|}{1} \tag{2.10}$$

Thus, the coordinates of P' (x_2, y_2) can be determined with the coordinates of P (x_1, y_1, z_1) by the follow Equation (2-11).

$$x_2 = \frac{x_1}{1+|z_1|}$$
$$y_2 = \frac{y_1}{1+|z_1|} \tag{2.11}$$

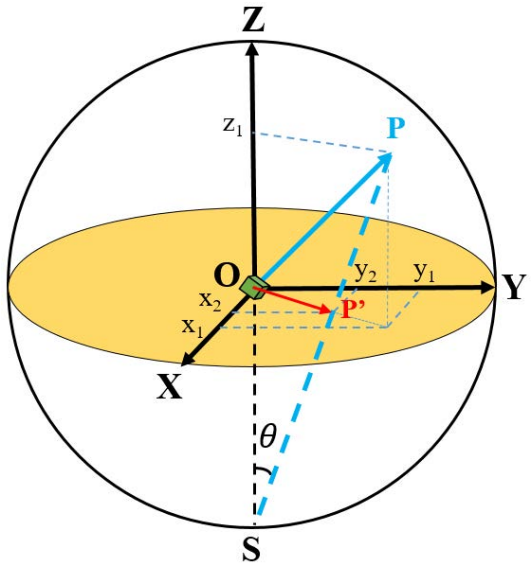

Fig. 2-8 Illustration of representation of a vector in 3D space to a 2D plane by stereographic projection method. OP is the vector in 3D space, X-O-Y is the projection plane (equatorial plane), P' is the projection of P in the projection plane (defined as the intersection between the projection plane X-O-Y and the connection line between P and the south pole (S) of the unit sphere).

2.2.6 Trace analysis method

For deformation realized by dislocation slip, a step will be formed on the sample surface when a dislocation glides out of the surface. Thus, slip traces can be observed when a sufficient amount of dislocations glide out of the sample surface. Such slip traces can be used to identify the possible active slip systems using the trace analysis method. For a known crystal system (FCC for the present Cu), the main slip systems are known. Using the measured crystallographic orientation of the crystal with respect to the sample coordinate system (represented with the

Euler angles in Bunge notation [45, 46]), the orientations of the intersections of the theoretical slip planes of the crystal with the sample surface can be calculated. **Fig. 2-9a** shows how we determine the theoretical trace vector in the sample coordinate system. The xOy plane is the sample surface and also the observation plane. N_{sp} is the normal direction of the slip plane expressed in the sample coordinate system. The trace vector in the sample coordinate system is the cross product of the normal direction of the xOy plane and N_{sp}. Comparison between the observed trace and the theoretical trace are usually conducted in the pole figure. As shown in **Fig. 2-9b**, the xOy plane is selected as the projection plane and point A is the pole of the slip plane. If we connect the center of the pole figure and the pole of the slip plane, the theoretical trace should be perpendicular to the connection line between the origin of the projection plane and the pole (dotted line). By comparing the calculated intersection orientation with the observed slip trace orientation, the active slip plane could be determined.

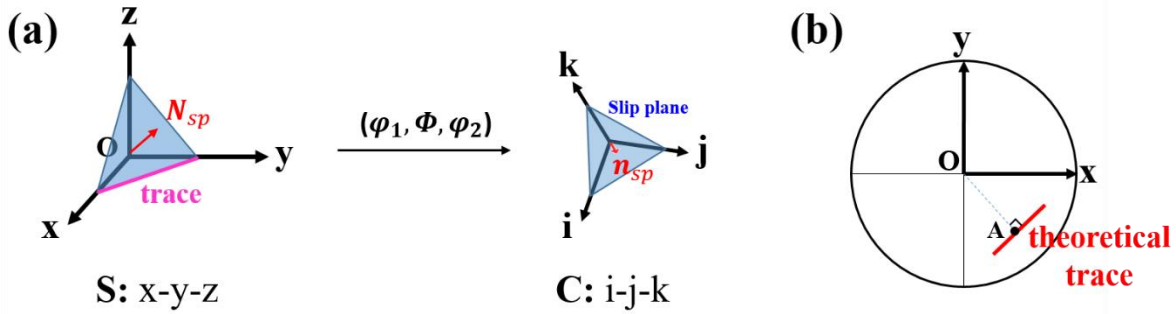

Fig. 2-9 Theoretical slip trace displayed in (a) sample coordinate system and (b) pole figure.

2.2.7 Twinning elements in FCC lattice

Twinning renders a part of a crystal to be in a symmetrical relation with the untwinned part.

The twinning mode of a twin can be fully defined by the twinning elements [47]. They are K_1 - the twinning plane (the first unrotated and undistorted plane), η_1 - the twinning direction, K_2 - the conjugate twinning plane (the second undistorted plane) which rotates this plane to K_2' in the twin, η_2 - the conjugate twinning direction which becomes η_2' in the K_2' plane, P - the plane of shear that is perpendicular to K_1 and K_2 and possessing η_1 and η_2, and s - the magnitude of shear which equals $2cot\ \alpha$, as shown in **Fig. 2-10**.

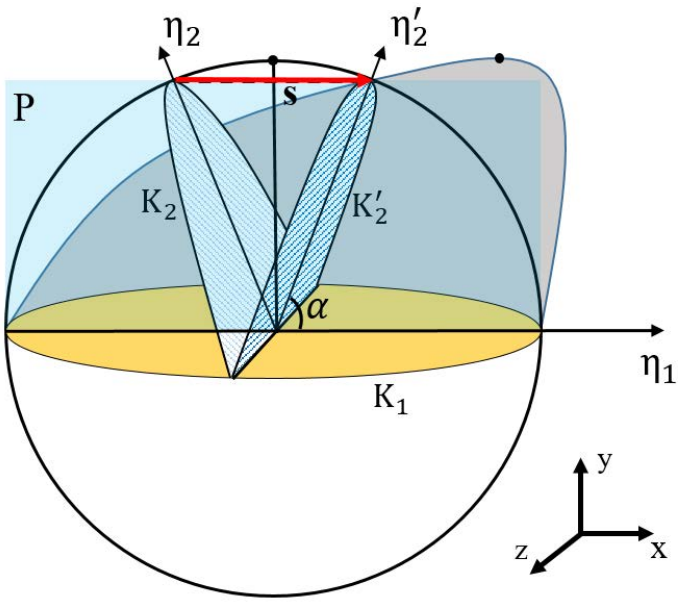

Fig. 2-10 Illustration of twinning elements [47].

Chapter 3 Fabrication of the GNS/Cu composites

3.1 Raw materials

The raw materials used in this study include two parts, the cold-rolled Cu foils and the graphene nanosheets (GNSs). The GNSs were purchased from Knano Co. Ltd. (P.R. China) produced by the thermal reduction of graphite oxide. The raw GNSs are agglomerated in fluffy powder structure. Each GNS exhibits irregular-shaped flake morphology with a mean diameter ranging from 1~3 μm and a thickness around 1~5 nm, corresponding to a thickness of less than 15 layers of graphene (assuming that the thickness of monolayer graphene is 0.34 nm). This thickness was verified by Atomic Force Microscopy (AFM) analysis. **Fig. 3-1a** shows an example AFM image of the raw graphene nanosheet (light brown) deposited on a single-crystal silicon substrate (dark brown) from an aqueous dispersion, and **Fig. 3-1b** the thickness profile along the white line in **Fig. 3-1a**, starting from the point marked with the green triangle and ending at the point marked with the red triangle. The average thickness of the GNS is about 3.85 nm that is consistent with the specification thickness of the purchased GNSs.

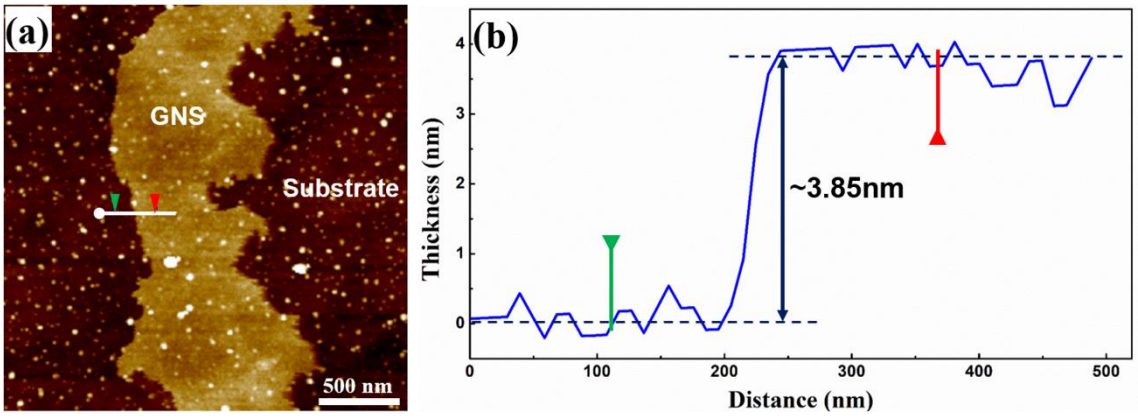

Fig. 3-1 (a) AFM image of a raw graphene nanosheet (GNS) deposited on a single-crystal silicon substrate and (b) the corresponding thickness profile along the white line in (a).

The as-cold-rolled industrially pure Cu foils with 3 kinds of thickness (10 μm, 30 μm and 50 μm) were used in this work. The chemical composition of the Cu foils is displayed in **Table 3-1**.

Table 3-1 Chemical composition of Cu foil (wt.%) used in this work.

Cu	Pb	Fe	Sb	S	As	Bi
≥ 99.90	≤ 0.005	≤ 0.005	≤ 0.002	≤ 0.005	≤ 0.002	≤ 0.001

3.2 Fabrication method

The fabrication method of the GNS/Cu composites in this work mainly consists of two steps (as displayed in **Fig. 3-2**):

(1) Electrophoretic deposition (EPD) of GNSs on the Cu foil surfaces;

(2) Stacking of the as-deposited Cu foils and sintering to as-sintered composites by vacuum hot-pressing sintering:

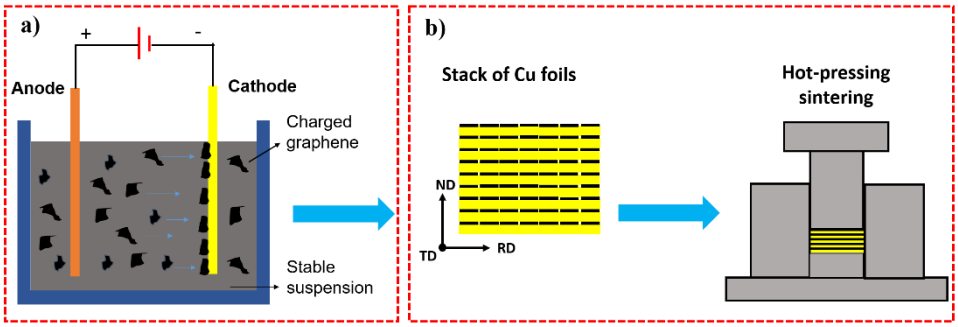

Fig. 3-2 Schematic illustration for the fabrication of as-hot-rolled Cu/GNS laminated composite. (a) GNSs were deposited on Cu foils by electrophoretic deposition and (b) Cu foils deposited with GNSs were stacked together and sintered into Cu/GNS composites by vacuum hot-pressing sintering.

3.2.1 Electrophoretic deposition (EPD) of the GNS

In order to fabricate the laminated Cu/GNSs composites, the first step is to construct the laminated basic unit by depositing the GNSs on the raw Cu foil surface. In this study, the electrophoretic deposition technique was employed to deposit the GNSs on the Cu foil surfaces.

As shown in **Fig. 3-3**, the electrophoretic deposition (EPD) process was conducted in an electrolytic cell. A pure Cu plate of 50×50×5 mm^3 was employed as the anode and the cold-rolled Cu foils with the same sized surface area as the cathode. Electrolyte suspension with GNSs of 0.004 $g \cdot mol^{-1}$ was utilized and the distance between the two electrodes was 50 mm. After deposition, the as-deposited Cu foils were dried in air and stored in a vacuum tank for the subsequent stacking and the hot-pressing sintering. For comparison, the Cu foils without the

deposition of the GNSs were also prepared. 100 foils of Cu each with an area of 4×4 mm^2 with and without the GNSs were further stacked to thick bulks. The stacks were made along the direction normal to the foil plane, i.e., the normal direction (ND) in the orthonormal rolling coordinate system (the rolling direction (RD), the transverse direction (TD) and the ND) by keeping the respective RD and TD consistent for each foil. The stacks with the GNSs were denoted GNS/Cu and the stacks without the GNSs pure Cu.

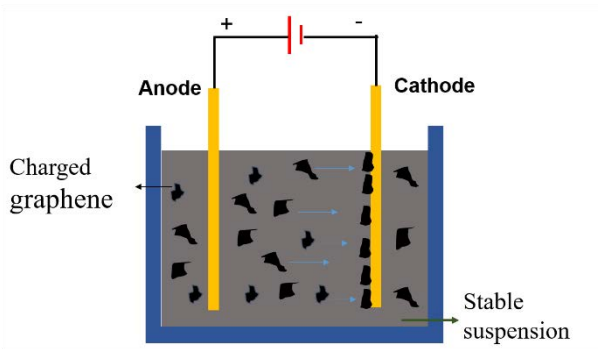

Fig. 3-3 Schematic illustration of the Electrophoretic deposition of the GNSs on the Cu foil.

3.2.1.1 Optimization of the ultrasonic vibration processing duration

Pre-dispersion of the GNSs in the isopropanol solvent is performed by the ultrasonic vibration process. Because the GNS possesses nano sizes, they tend to agglomerate into big clusters in the suspension because of the Van der Waals force. To avoid this, a long-time ultrasonic treatment is necessary to uniformly disperse the GNSs in the suspension, which is important for a successful fabrication of the Cu-GNS basic unit.

In this study, the influence of the ultrasonic vibration time on the dispersion of the GNSs in the electrolyte suspension was investigated. **Fig. 3-4** displays the SEM-secondary electron (SE) images of Cu foils deposited with the GNSs for 10 min after the electrolyte suspension was processed with ultrasonic vibration for different times. The ultrasonic processing time has great influence on the dispersion of the GNSs in the suspension. When the suspension was ultrasonically processed for 2 h, many GNS clusters were observed on the Cu foil surface (as shown in **Fig. 3-4a** and **d**). This means that the ultrasonic vibration process did not eliminate the big clusters of the GNSs in the suspension. When the ultrasonic processing time was

increased to 5 h, giant clusters of GNSs was not found anymore on the Cu foil surface and the GNSs with high transparency were observed (as shown in **Fig. 3-4b** and **e**). After the ultrasonic processing time was further increased to 10 h, the GNS clusters were fully eliminated in the suspension and individual GNSs were observed deposited on the Cu foil surface (as shown in **Fig. 3-4c** and **f**). Thus, in this study, the GNS suspension were ultraosonically processed for 10 h to realize a uniform dispersion of the GNSs in the electrolyte suspension.

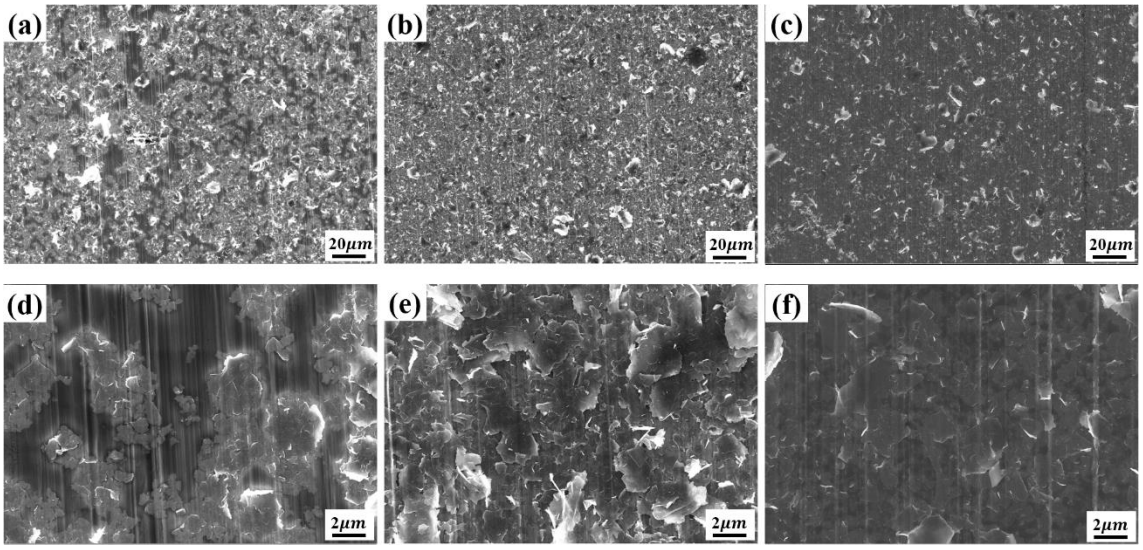

Fig. 3-4 SEM-secondary electron (SE) images of Cu foils deposited with GNSs for 10 min by electrolyte suspension after ultrasonically vibrated for (a) and (d) 2h, (b) and (e) 5 h and (c) and (f) 10h.

3.2.1.2 Optimization of deposition time

The influence of the deposition time was investigated to find the optimum deposition parameters. **Fig. 3-5** shows SEM-SE images of the Cu foils deposited with GNSs for different times (5 min, 10 min, 15 min and 30 min) by keeping the other deposition parameters (voltage, current and electrolyte solution) identical. When the Cu foil was deposited with the GNSs for 5 min (as shown in **Fig. 3-5a**), we can see that only a few GNSs were deposited on the surface of the Cu foil, leaving most of the Cu foil surface exposed. With the increase of the deposition time, more GNSs were observed deposited on the surface of the Cu foil as displayed in **Fig. 3-5b** and **c**. However, when the deposition time was increased to 30 min, too many GNSs were deposited on the Cu foil surface. Some of them were observed overlapped (as shown in **Fig. 3-**

5d), which is not desired for the composite. Thus, in this study, the GNSs were deposited for 15 min for each Cu foil. It should be noted that both sides of the Cu foil surface were deposited with the same volume of GNSs. This means that the coverage of the GNSs on the Cu foil will be increased when we stack the Cu-GNS foils together.

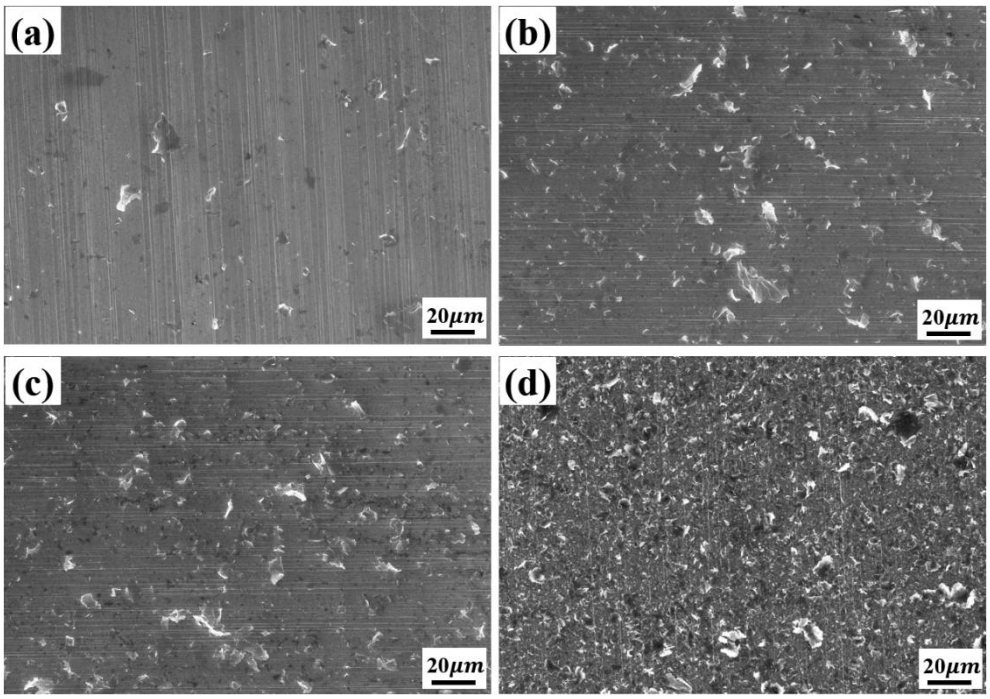

Fig. 3-5 Cu foil deposited with GNSs for (a) 5 min, (b) 10 min, (c) 15 min and (d) 30 min.

Fig. 3-6 shows the SEM-SE micrographs of the raw cold-rolled Cu foil surface (**Fig. 3-6a**), and Cu foil deposited with GNSs on the surface (**Fig. 3-6b** and **c**). As can be seen, the surface of the raw Cu foil is clean and the rolling pattern is still clearly observed along the rolling direction (indicated with the yellow arrow). After deposition with the GNSs for 60 seconds, we can see that the GNSs are distributed uniformly on the Cu foil surface. Notably, these GNSs do not superimpose one on the other, which means that the pre-dispersion of the GNSs in the isopropyl alcohol solution by ultrasonic vibration for 10 h was effective to realize a uniform GNS distribution and to avoid the formation of GNS agglomerations in the solution. It can be observed that almost all the GNSs tile on the Cu foil surface because of the two dimensional structure of the GNSs. Since the Cu foils were deposited with the GNSs on both surfaces, the coverage of the GNSs will be doubled when these deposited Cu foils were stacked together

during the subsequent sintering process, which achieved a nearly continuous distribution of the GNSs in the GNS layer.

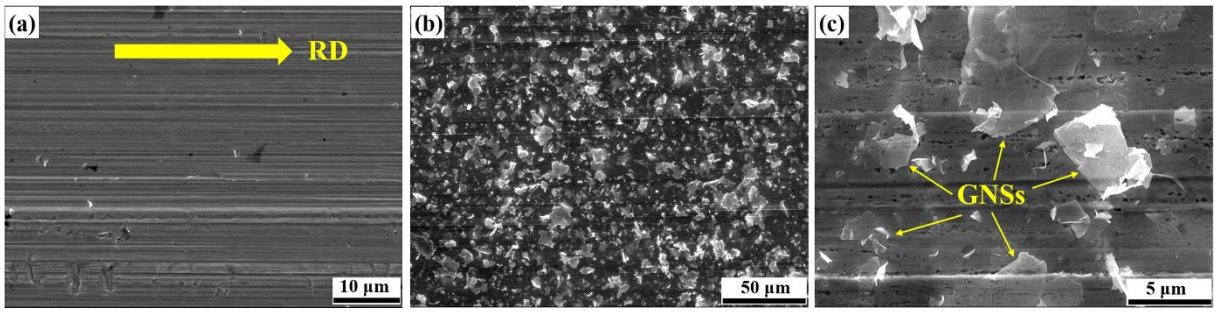

Fig. 3-6 SEM-SE images of (a) as-cold-rolled Cu foil and (b) and (c) Cu foils deposited with GNSs on surface at different magnifications.

3.2.2 Vacuum hot-pressing sintering and heat treatment

The hot-pressing sintering process of the GNS/Cu composite and the pure Cu was identically conducted in vacuum (<10^{-2} Pa) under a compressive stress of about 50 MPa applied along the ND. The stacks were first heated to 950 °C at a rate of about 5 °C· min^{-1}, isothermally held for 2 h and then cooled inside the furnace to room temperature. To accelerate the cooling process, a circulating cooling water system of the furnace was switched on. As all the microstructural processes in the material finished before the cooling process, the aim of the cooling inside the furnace was to keep the materials under vacuum thus to protect them from being oxidized at high temperatures.

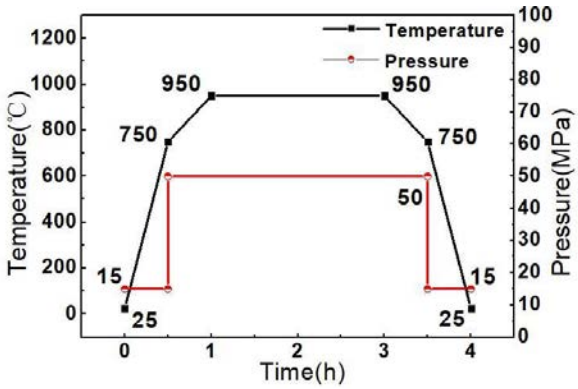

Fig. 3-7 Sintering process diagram of pure Cu and GNS/Cu composites for fabrication of as-sintered samples.

To study the microstructural and texture evolution during recrystallization, the pure Cu and Cu/GNS composite samples were heated to various temperatures using a dilatometer (DIL

805A/D). The cold-rolled Cu foils were shaped into squares of 4mm×4mm and stacked into stacks with total thicknesses of 1~3 mm along the ND of the cold-rolled foil. The stacks were put into a sample holder (made of 430 stainless steel (ferritic steel)) as displayed in **Fig. 3-8**. A thermocouple was welded on the surface of the sample holder for monitoring the real-time heating temperature. The heating process was conducted under vacuum (<10^{-2} Pa) at a heating rate of 5 °C· min^{-1}. When reaching the set heating temperature, the as-heated sample was quenched with forced argon flow to room temperature. The detailed parameters for Cu and Cu/GNS composites with different Cu foil thickness were summarized in **Table 3-2**.

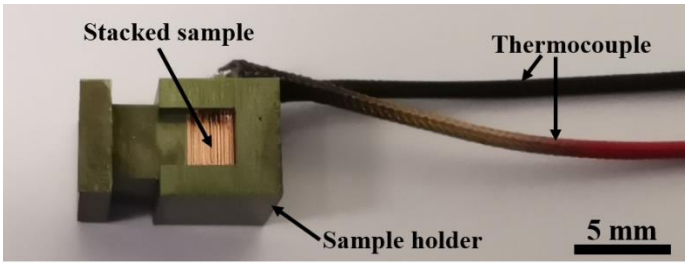

Fig. 3-8 Samples of pure Cu and Cu/GNS composite used in this work for heat treatment in a dilatometer (DIL 805A/D).

Table 3-2. Heating temperatures for heat treatment of Cu and Cu/GNS samples with different Cu foil thickness.

Thickness	**Temperature / ℃**					
10 µm	150	200	280	350	450	700
30 µm	150	170	230	450	700	

3.3 Summary

In the present work, cold-rolled Cu foils with thicknesses of 10 µm and 30 µm were deposited with GNSs using an electrophoretic deposition technique. The deposition parameters of ultrasonic processing duration and deposition duration were optimized. The stacked Cu foils with and without GNSs were sintered into bulk as-sintered pure Cu and Cu/GNS composites using the hot-pressing sintering method under vacuum. In order to study the microstructure and

texture evolution of Cu foils and Cu/GNS composites during heating of the sintering process, the Cu and Cu/GNS stacks were heated to different temperatures using a Dilatometer (DIL 805A/D) under vacuum. With the fabricated composites and the prepared samples, the research work in the following chapters was carried out.

Chapter 4 Recrystallization texture evolution of cold-rolled Cu foils governed by microstructural and sample geometrical factors during heating

4.1 Introduction

Recrystallization is an important microstructural process of cold-deformed metallic materials during thermal treatment. Through this process, the materials undergo microstructure evolution and produce different preferred crystallographic orientations or texture, which results in drastic mechanical and physical property changes. Owing to the technical importance and the theoretical significance of this phenomenon, recrystallization has long been a subject of intensive investigations [2, 23, 48]. However, nucleation and grain growth related controversial experimental results are always observed by researchers in different material systems, thus none of the proposed theories could entirely explain the results. Therefore, quantitative and detailed information on recrystallization are needed for deepening the understanding of this process, especially in 2D materials. In this chapter, cold-rolled Cu foils with thickness of 10 μm without GNSs were employed to investigate the recrystallization of cold-worked Cu governed by both microstructural and sample geometrical factors, i.e., stored deformation energy, elastic strain energy, surface energy and boundary mobility. The global orientation evolution of the Cu foils was investigated by neutron and synchrotron radiation measurements and the thermal lattice strain by *in-situ* synchrotron radiation in macroscopic scale, combined with the spatially correlated microstructure and orientation examination by SEM-EBSD at meso/micro scale. The results were further analyzed in the frame of the orientation dependent crystal elasticity and surface energy.

4.2 Experiments

In this chapter, the cold-rolled Cu foils with thickness of 10 μm were employed. The stacked Cu foils without GNSs were heated to 150 ℃, 200 ℃, 280 ℃, 350 ℃, 450 ℃, 700 ℃ and 950 ℃, respectively. The detailed information on sample preparation can be found in

§ 3.2.2. The microstructure of the as-cold-rolled, as-sintered and as-heated Cu samples were characterized by SEM-EBSD. The texture of different states of samples were measured by neutron and synchrotron radiation diffraction. The software StressTextureCalculator (SteCa2-2.0) was used to extract the pole figure intensity data. The evolution of the lattice strains of Cu samples during the heating process was investigated by the 4D *in-situ* synchrotron radiation diffraction technique (3D space + 1D time). The Debye-Scherrer rings were integrated to the diffraction patterns with the Fit2D package, and the data from the LaB_6 powder measurement was used to subtract the instrumental effect. The information contained in the peak profile, such as the integrated intensity (I) and the Bragg angles (2θ) of the peaks at each measured temperature were extracted.

4.3 Results

4.3.1 Texture and microstructure of cold-rolled Cu foils

Fig. 4-1a shows the typical φ_2 = 0°, 45° and 60° sections of the orientation distribution function (ODF) of the cold-rolled Cu foils. The ideal positions of the cold-rolling texture components are also indicated for reference. It is seen that the texture is dominated by four components constituting two typical fibers, i.e., the β fiber (from Copper to Brass through the S component) and the α fiber (from the Brass to the Goss component). The intensities of the β fiber components are much stronger but in a decreasing order from the Copper to the Brass. Moreover, the Copper and the S components spread toward the Cube orientation (φ_2 = 45° and 65° sections). In addition, the Cube that is known as the typical recrystallization texture component also exists in the cold-rolled Cu foils but with much lower intensity.

Fig. 4-1b-c display the SEM-EBSD orientation micrographs of the cold-rolled Cu foil measured at the RD-TD (**Fig. 4-1b**) and the RD-ND (**Fig. 4-1c**) sections. The deformed grains were colored according to the respective texture components (**Fig. 4-1b$_1$** and **c**) and also in Kikuchi band quality index (**Fig. 4-1b$_2$**). It is seen that the deformed Cu grains are in band shape and elongated along the RD (**Fig. 4-1c**). Most of the grains belong to the texture components revealed by the ODF sections in **Fig.4-1a**. However, large orientation deviations exist within almost all grains, as represented by the color variation of the grains in **Fig. 4-1b$_1$** and **c**. Due to

the large deviation, the orientation of one deformed grain can evolve from one component to another, for example from the Copper to the S or from the Brass to the Goss (**Fig. 4-1b1**). The orientation transition is more frequent at grain boundary regions. This indicates that the deformation was very heterogeneous or localized. Moreover, thin deformation bands were formed in some coarse grains, some being horizontal and the others vertical, as indicated by the white arrows in **Fig. 4-1b1**. The latter is always discontinuous. This further evidences the existence of heterogeneous deformation. However, such deformation heterogeneity does not appear for all the deformation orientations. The high Taylor factor orientations (the Copper and the S) suffer more than the low Taylor orientations (the Cube, the Goss and the Brass). This fact seems to be in agreement with the statement that the grains with high Taylor factors (the S and the Copper) possess high deformation stored energy [49] represented by high dislocation density. Interestingly, cell structures already existed in some deformed grains, especially in the deformation bands and in heterogeneous deformation regions of grains with high Taylor factor, as clearly seen in **Fig. 4-1b$_2$.** This indicates that recovery already happened in the cold-rolling state. These cells may become potential recrystallization nuclei during the subsequent heating.

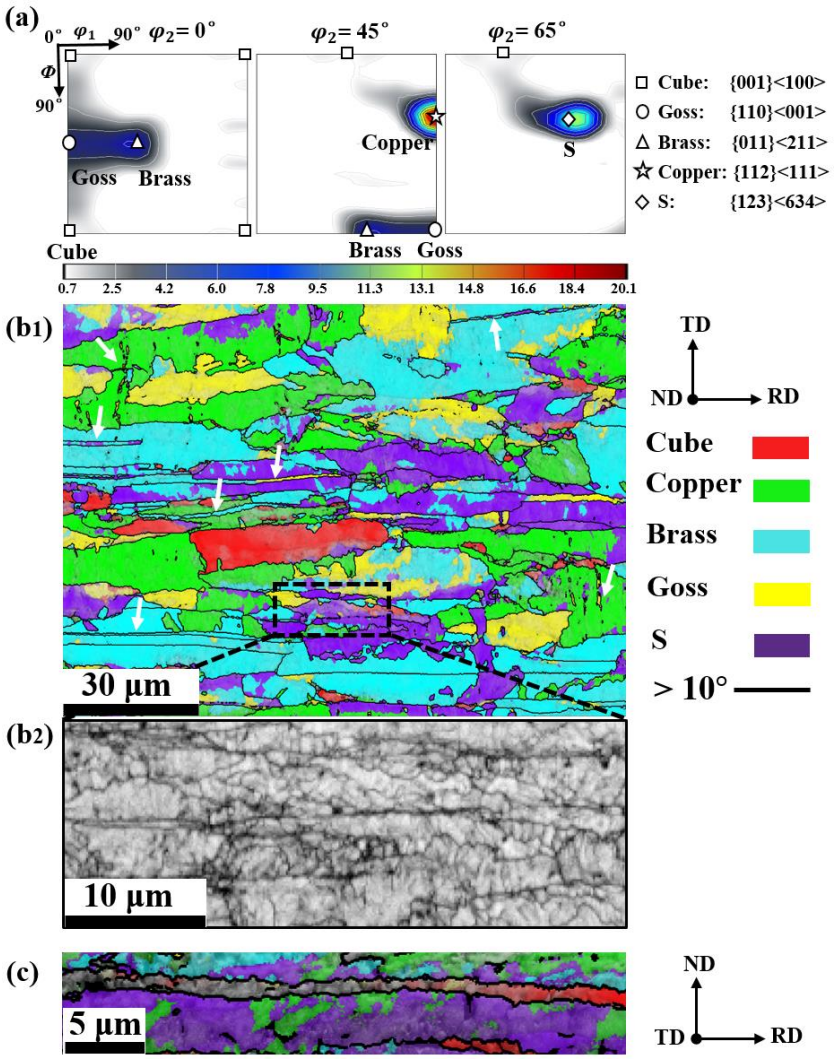

Fig. 4-1. Texture and microstructure of cold-rolled Cu foils. (a) Typical φ2 = 0°, 45° and 65° sections of orientation distribution function (ODF) determined from neutron diffraction measurements (ideal texture components of cold-rolled FCC materials are detailed and indicated). SEM-EBSD orientation micrographs of (b1) RD-TD section, (c) RD-ND section colored according to orientation of cold-rolling texture components of FCC metals and (b2) band quality indexed micrograph of RD-TD section.

4.3.2 Texture evolution during heating

Fig. 4-2 shows the ODF sections (φ_2 = 0°, 20°, 30°, 35°, 45° and 55°) of the stacked Cu samples heated to 150 ℃, 280 ℃, 350 ℃, 450 ℃ and 700 ℃, respectively, with the ideal orientations for reference. As the orientations of the recrystallized Cu foils may not possess the rolling symmetry, we reduced the Euler space according to the cubic crystal symmetry and the triclinic sample symmetry, *i.e.*, φ_1: 0~360°, Φ: 0~90° and φ_2: 0~90° [28] to fully describe

the texture of the as-heated Cu foils. It is seen that, in general, the texture changed from a typical cold-rolling texture to a recrystallization texture dominated by three pairs of distinct orientations, as described in **Table 4-1**.

Table 4-1. Three pairs of rotated orientations as principal recrystallization texture components in as-heated Cu foils.

Orientation pair	Component	Euler angle	Miller indices
1	RD-rotated Cube-1	(0, 30, 0)	(0 4 7) [1 0 0]
	RD-rotated Cube-2	(0, 60 ,0)	(0 7 4) [1 0 0]
2	φ_2-rotated Copper-1	(90, 35, 35)	(2, 3, 5) [-9, -14, 12]
	φ_2-rotated Copper-2	(90, 35, 55)	(3, 2, 5) [-14, -9, 12]
3	φ_2-rotated Copper-3	(49, 62, 22)	(2, 5, 3) [9, -12, 14]
	φ_2-rotated Copper-4	(30, 71, 30)	(3, 5, 2) [14, -12, 9]

Further examinations revealed that at low heating temperatures (150°C and 280°), the foils were still dominated by the cold-rolling components (Copper, Brass and S) but with much reduced sharpness (as displayed in **Fig. 4-2a** and **b**). A detailed microstructural analysis will be given in the next section. The pronounced change occurred when the Cu samples were heated to 350 ℃. The change is characterized by two features. One is the drastic weakening of the cold-rolling components (**Fig. 4-2c,**), and the other is the emergence of three pairs of new orientations (one pair of RD-rotated Cube and two pairs of φ_2-rotated Copper, especially the former). It should be mentioned that the two φ_2-rotated Copper orientations are related by sample symmetry. The three pairs of new orientations were fully developed and became dominant with increased intensities when the temperature reached 450 °C (**Fig. 4-2d**) where the cold-rolling components became weak. The three pairs of rotated-orientations, especially the φ_2-rotated Copper, are more straightforward with the representation of the φ_2 sections of the cylindrical Euler space [28], as shown in **Fig. 4-3**. In fact, geometrically the two pairs of φ_2-rotated Copper orientations are related to two individual Copper orientations by ±10° around the c-axis of the two Copper oriented crystals. The two individual Copper orientations are related by the sample symmetry. When the Cu sample was further heated to 700 ℃ (**Fig. 4-2e**), the intensities of the three pairs of new orientations were slightly increased (with the

maximum intensity increased from 3.36 m.r.d to 4.21 m.r.d) with the identical texture pattern in the ODF sections. It should be noted that the φ_2-rotated Copper components are quite close to the Copper and the S components. The spread covering these two deformation orientations indicate that the two rolling components were not totally eliminated by the recrystallization. Clearly, during the heating process from the room temperature to 700 °C, the texture transition from the deformed type (cold-rolling texture) to the recrystallization texture (dominated by the three pairs of rotated orientations) occurred progressively. Next, we will analyze in detail the orientation correlated microstructure evolution that underlay the texture transition by SEM-EBSD.

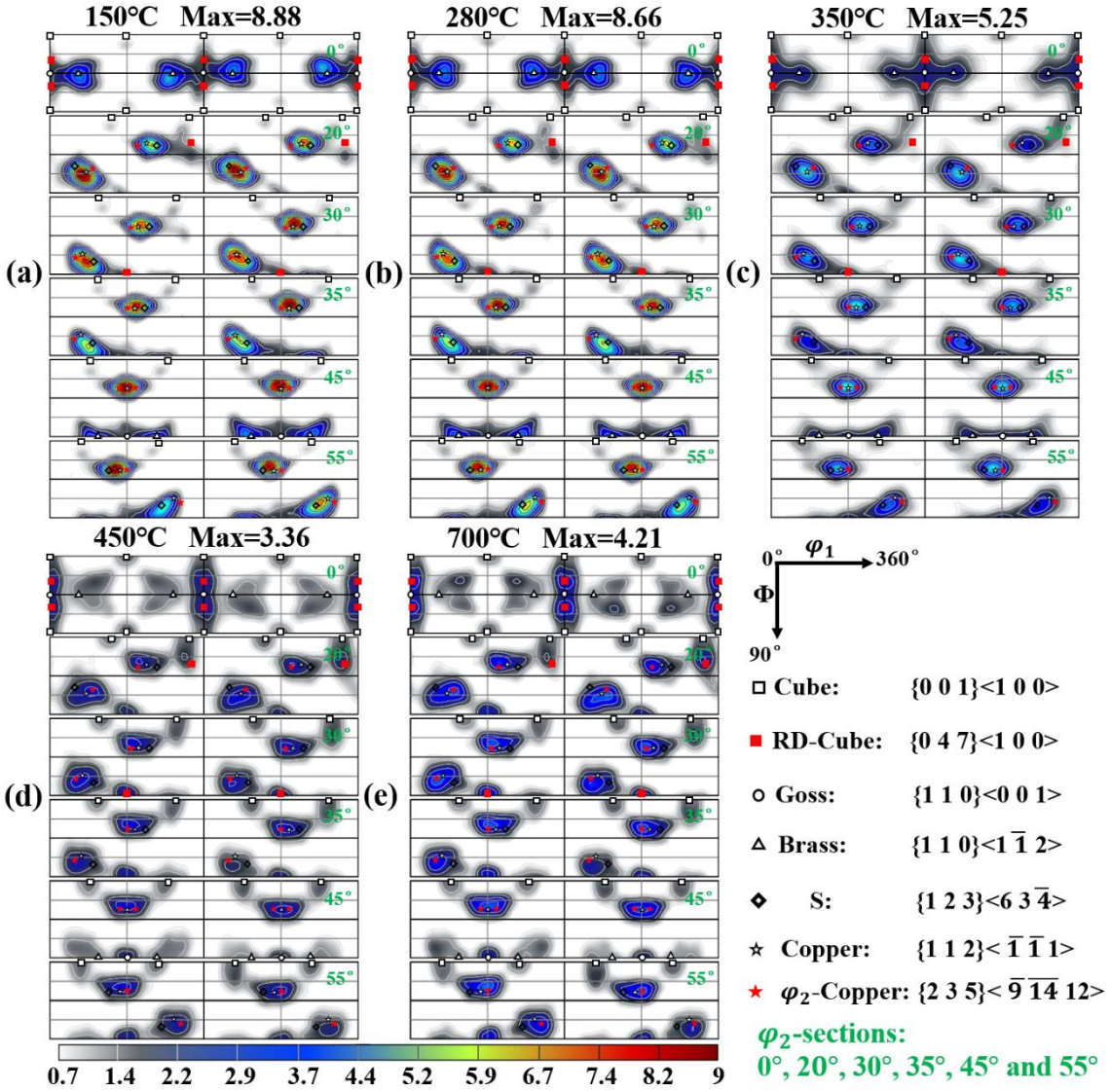

Fig. 4-2. ODF sections (φ_2 = 0°, 20°, 30°, 35°, 45° and 55°) of Cu foils heated to **(a)** 150 °C, **(b)** 280 °C, **(c)** 350 °C, **(d)** 450 °C and **(e)** 700 °C.

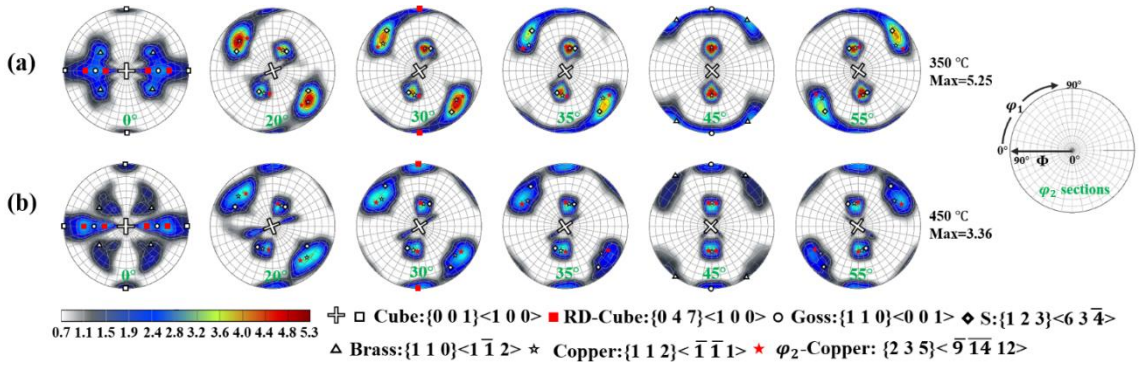

Fig. 4-3. Texture of Cu foils heated to (a) 350 °C and (b) 450 °C represented in cylindrical Euler space with φ_2 sections of 0°, 20°, 30°, 35°, 45° and 55°.

4.3.3 Microstructure and orientation evolution during heating

The microstructure of Cu samples heated to different temperatures (200 °C, 280 °C, 350 °C and 450 °C) were examined on the RD-TD section. **Fig. 4-4** shows the corresponding SEM-EBSD orientation micrographs to demonstrate the microstructure evolution during the nucleation and the subsequent growth of the formed nuclei.

4.3.3.1 Recrystallization nucleation

It is seen from **Fig. 4-4a1** and **a2** that at 200 °C although the foil is still dominantly occupied by the band-shaped deformed grains, new distortion-free regions, i.e., recrystallization nuclei, started to form and yielded a recrystallization fraction of about 0.64±0.03 %, as highlighted in blue in **Fig. 4-4a2**. Detailed analysis on the nucleation sites showed that the nuclei could be classified into three groups:

1) within a deformed grain (denoted **Intra1**);

2) at the interface between two or more deformed grains but belonging to one of them (denoted **Intra2**);

3) at the interface between two or more deformed grains but belonging to none of them (denoted **Inter**).

The amounts of the three groups are quite different. The number fractions of the three types were analysed and are displayed in **Fig. 4-5a**. Clearly, the **Intra2** type is in absolute majority (about 60.3 %) in comparison with the other two types (**Intra1** (15.6 %) and **Inter**

(24.1 %)). Detailed orientation analysis showed that for the **Intra1** type the nuclei are always disoriented from their matrices and the disorientations spread in a large angle range from low (~2°) to high (~15°). For the two other types (**Intra2** and **Inter**) the distribution of the disorientation angle between the nuclei and their neighbours present a bi-modal feature, as shown in **Fig. 4-5b**, one peak at about 20° and the other at 55°. The latter is numerous.

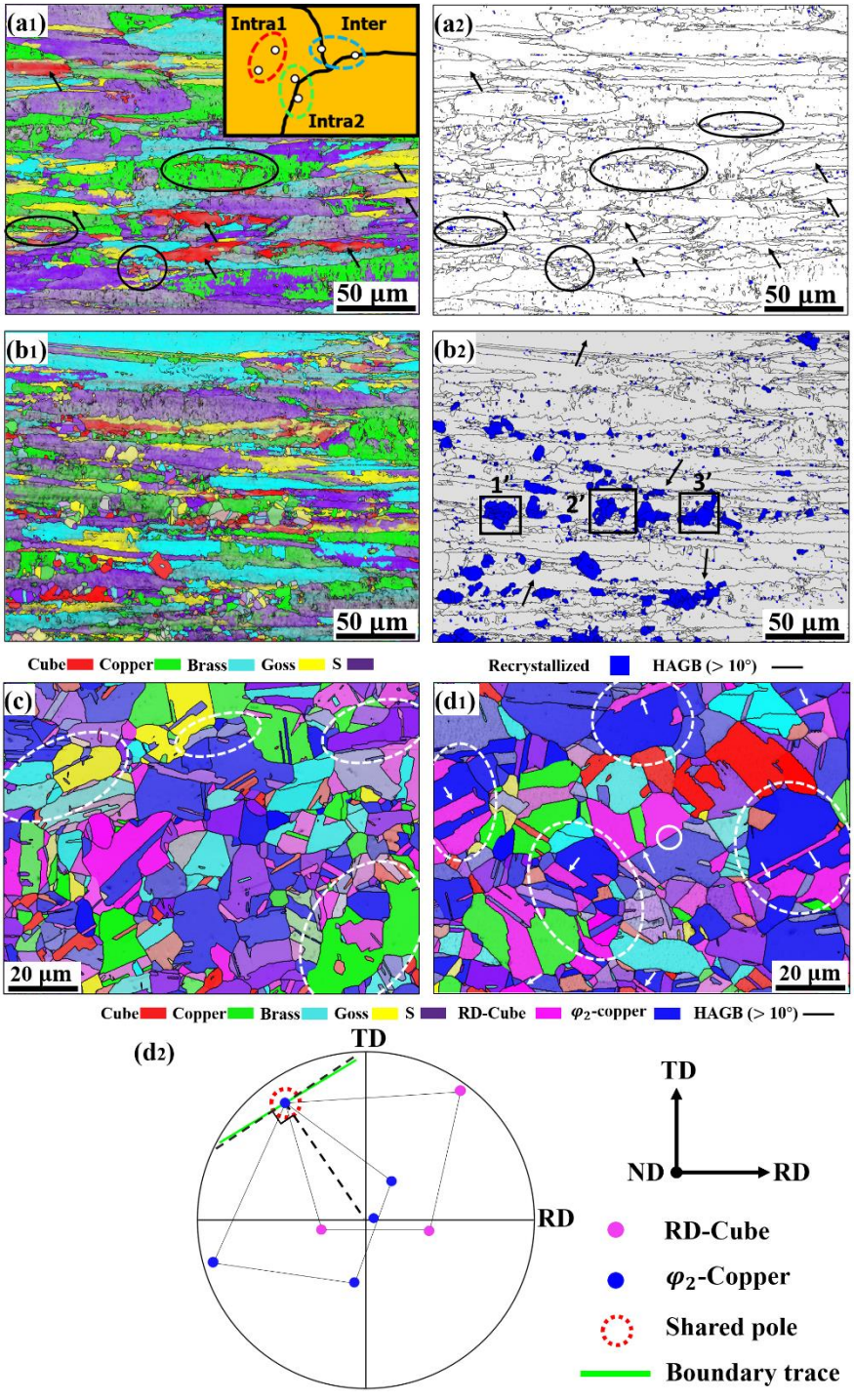

Fig. 4-4. SEM-EBSD texture component micrographs of Cu heated to (a1) 200 ℃, (b1) 280 ℃, (c) 350 ℃ and (d) 450 ℃. Recrystallized grains in blue in Cu foils heated to (a2) 200 ℃ and (b2) 280 ℃. (d2) {111} pole figure of selected area enclosed in the solid circle in (d1).

In order to statistically investigate the orientation features of the nuclei, the orientations of the nuclei in **Fig. 4-4a$_2$** were further plotted in the Euler space weighted with their areas and are displayed with the φ_2= 0°, 20°, 30°, 35°, 45° and 55° sections in **Fig. 4-6a**. It is seen that the orientations are mainly clustered at two locations. One is at the RD-rotated Cube positions (from the Cube position) and along the α fiber (from Goss to Brass component) with certain spread from the α fiber (denoted **cluster 1**) and the other at the orientation cluster of the Copper, the S and the φ_2-rotated Copper (denoted **cluster 2**). Moreover, the nuclei with the orientation close to the Cube show size preference, whereas those with orientations at **cluster 2** possess smaller sizes. Further examination on the nucleation sites revealed that the nuclei with orientations at **cluster 1** are not from the large-sized deformed grains with the Cube, the Goss or the Brass orientations (as indicated by the black arrows in **Fig. 4-4a$_1$** and **a$_2$**). Instead, they were rather formed within the heterogeneous deformation regions, such as thin deformation bands and highly disoriented zones in the Copper and the S grains or from small individual grains adjoining the other grains (as circled by black solid cycles in **Fig. 4-4a$_1$** and **a$_2$**). This further confirms that most of the nuclei were evolved from the substructures of the deformed grains with high deformation heterogeneity. More precisely, the recrystallization nucleation occurred preferentially from the low Taylor factor regions surrounded by high Taylor factor matrix. This fact is neither in agreement with the so-called "high stored energy nucleation mechanism" [15] nor with the "low stored energy nucleation mechanism" [16], both of which were reported in the literature.

When the Cu foils were heated to 280 ℃ (**Fig. 4-4b$_1$** and **b$_2$**), the recrystallization continued through both further nucleation of the new grains and the growth of the already recrystallized nuclei, resulting in a total recrystallized fraction of about 10.62%. Due to the two events, the recrystallized microstructure became heterogeneous in terms of size and distribution (as displayed in **Fig. 4-4b$_2$)**. The sizes of the grown nuclei amount to about 10 to 20 μm,

whereas the new coming ones are as small as 1 to 2 μm. Interestingly, the growth often happened to several neighboring nuclei and gave rise to the formation of grain agglomerates, as outlined with the black frames in **Fig. 4-4b2**. In view of this significant heterogeneity, we analyzed the orientation features of the two groups, the recrystallized nuclei and the grown grains, and plotted their orientations in the Euler space, as shown in **Fig. 4-6b** and **c**. The separation between the two groups is 4 μm^2 that is the maximum grain area of the recrystallized grains at 200 °C. For the new nuclei with grain area smaller than 4 μm^2, they still possess the similar orientation features to those of the nuclei formed at 200 °C, as displayed in **Fig. 4-6b** but the number of the nuclei is greatly increased. However, at 280°C, the nuclei with orientations at **cluster 2** (Copper, S and the φ_2-rotated Copper) started to gain comparable sizes with respect to those located at **cluster 1** (RD-rotated Cube and Goss to Brass along the α fiber). Although at this temperature, nucleation happened intensively in many deformed grains, few nuclei appeared in the deformed matrix with small orientation variation, as indicated with the black arrows in **Fig. 4-4b2**. Most of them are low Taylor factor orientations (the Brass and the Goss). This evidenced that the deformed grains with constant orientation were more stable than grains with large orientation variation or with deformation bands during the heating process. Interestingly, for the grown grains as shown in **Fig. 4-6c**, their orientations do not possess the same orientation features as those of the small nuclei but become dispersed, suggesting that the growth is selective by other factors different from those for nucleation.

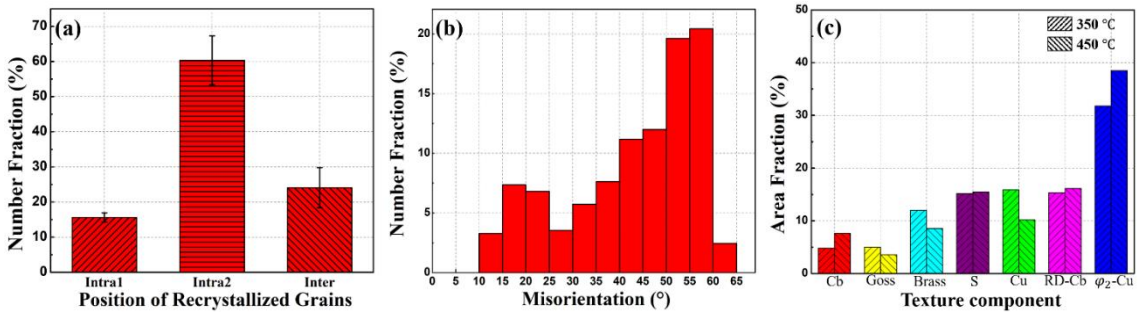

Fig. 4-5. Number fractions of (a) nuclei formed at various positions in Cu foil; (b) misorientation angle between nuclei and neighboring grains; (c) area fractions of differently oriented grains in Cu foils heated to 450 °C.

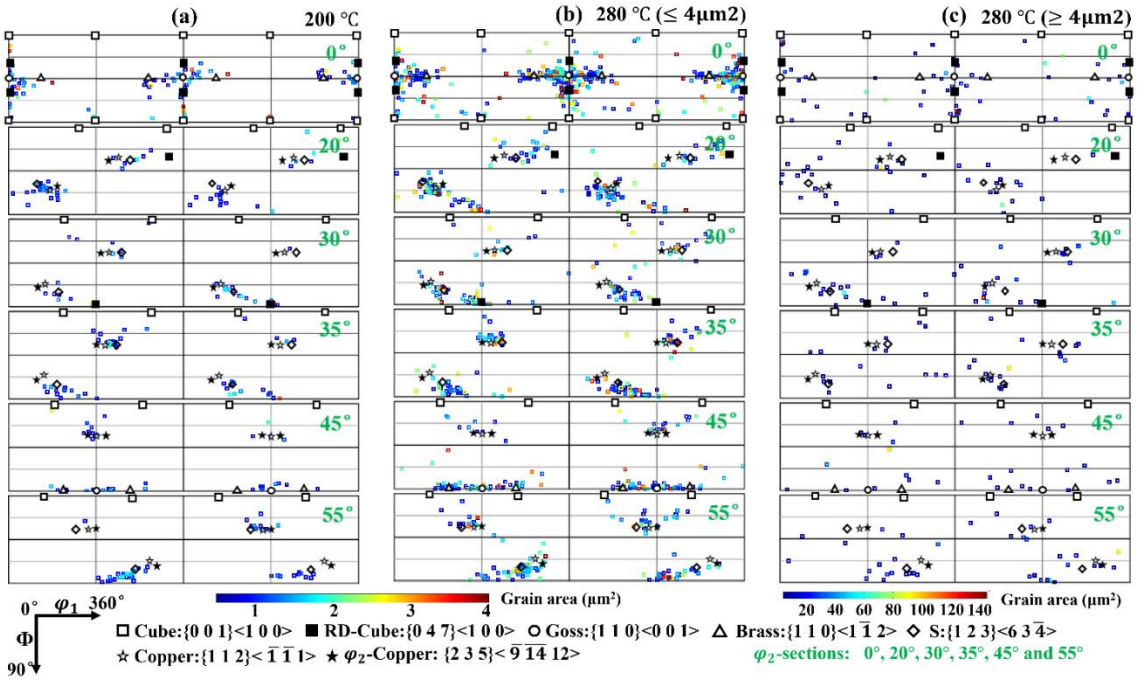

Fig. 4-6. φ2= 0°, 20°, 30°, 35°, 45° and 55° sections of Euler Space showing orientations of recrystallized grains weighted by grain area in Cu foils heated to (a) 200 ℃, (b) 280 ℃: grain area smaller than 4 μm2 and (c) 280 ℃: grain area larger than 4 μm2.

4.3.3.2 Completion of Recrystallization

When the temperature was increased to 350 ℃, as seen in Fig. **Fig. 4-4c**, the original band-shaped deformation grains were totally replaced by the near equiaxed but, to some extent, irregularly shaped grain blocks, suggesting that the primary recrystallization was complete. According to the colors of the grains referenced to the color code in the figure caption and the area fractions of differently oriented grains in **Fig. 4-5c**, one can find that although the grains with the new recrystallization components appear, their amounts are not in majority (RD-rotated Cube: 15.33 % and φ_2-rotated Copper: 31.78 %). The remaining of the cold-rolling orientations occupy almost the half of the total microstructure, notably, the Copper (15.89 %) and the S (15.19 %), as well as the Brass (12 %), and the Goss (5.01 %) orientations. Further examining the shape of the grain blocks, we found that certain blocks should be the remnants of the deformed grains, as outlined with the white dotted circles in **Fig. 4-4c**. Some of them are still in elongated shape in the RD (the 3 circles in the upper area of **Fig. 4-4c**) and the others are large grains with small equiaxed grains embedded in them (the circle in the lower corner of

Fig. 4-4c). This suggested that the recrystallization happened in two different ways, discontinuous recrystallization [51-54] by forming nuclei and their growth to consume the deformed neighbors and continuous recrystallization [55, 56] through continuous decrease of dislocations of deformed matrices and surviving the consumption by the growth of the recrystallized nuclei. Through this, the recrystallization was finished with a mixture of newly formed grains and remnants of the deformed matrices. Thus, the orientations of the microstructure demonstrate a mixed feature as revealed by the macroscopic texture measurement result (**Fig. 4-2c**)**.** Another interesting phenomenon is that when recrystallization was complete, the sizes of the recrystallized grains are relatively homogeneous. The size heterogeneity at 280 °C (**Fig. 4-4 b$_2$**) was not inherited. This means, the growth of the near Goss and near Cube oriented grains which were favored during the primary grain growth were stagnated when they grew to the Cu foil surface. This stagnation may be related to their high surface energy, as analyzed in detail later.

When the Cu foils were heated to 450 °C, as shown in **Fig. 4-4d$_1$**, the microstructure is still composed of recrystallized grain blocks. Their sizes are obviously increased compared with those formed at 350 °C. In addition, the area fraction of the φ_2-rotated Copper (38.48 %) grains are further increased with the decrease of the area fractions of the residual cold-rolling components, i.e., the Copper (10.17 %), the Brass (8.56 %) and the Goss (3.59 %). However, the area fraction of the RD-rotated Cube stayed almost unchanged (15.33 % at 350 °C and 16.15 % at 450 °C). This evidenced that the grains with the φ_2-rotated Copper orientation were favored during the grain growth process as opposed to the other orientations of the initially recrystallized grains. This further indicates that the growth of the recrystallized grains is indeed selective. Close examination revealed that the grains with the two rotated components (RD-rotated Cube in pink and φ_2-rotated Copper in dark blue) are always in neighbor or even form grain agglomerates, as outlined with the white dotted lines in **Fig. 4-4d$_1$**. The two components are always separated by a straight interface, as seen in **Fig. 4-4d$_1$**. Crystallographic analysis showed that the two orientations are close to twin relation (60°/<111>) and the traces of most of the straight interfaces are close to their common {111} planes (the twinning plane K1), as

indicated by the white arrows in **Fig. 4-4d1**. Such a crystallographic feature of one example grain pair as circled with the solid line in **Fig. 4-4d1** are illustrated with their {111} pole figure in **Fig. 4-4d2**. From the pole figure we can see that the two grains share one common {111} pole, as highlighted with the dashed circle. The trace of their interface (the green line) is in quasi coincidence with the black dashed line that is perpendicular to the black dashed line connecting the origin of the stereographic projection plane and the overlapping poles. This suggests that the two grains share a common {111} plane as their boundary. Such a boundary is coherent that should have low energy and thus low mobility [46-48].

4.3.3.3 Annealing twin

Accompanying the recrystallization process, the formation of annealing twins represented as another microstructure feature. This phenomenon is typical for many FCC metals with medium to low stacking fault energy during recrystallization annealing, such as Cu, Ag and Au [57-59]. Our detailed microstructure examination revealed that at the nucleation stage, i.e., the sizes of the recrystallized grains are below 2 μm, there were no twins appearing within the nuclei, as shown in **Fig. 4-7a1**. The massive formation of twins happened during the subsequent growth of the nuclei, as shown in **Fig. 4-7a2**. This means that twins were formed when the nuclei grew into certain sizes. When the recrystallization is complete (350 °C), almost all recrystallized grains in the observed area contain twins, as shown in **Fig. 4-7b**. In the figure, the red Σ3 boundaries are used to indicate the twin relation between the two adjacent crystals. The Σ3 boundaries were detected at two kinds of places, within recrystallized grains and at boundaries between blocks. We denote the former ones intragranular twin and the latter intergranular twin. For the intergranular type, the formation of the twin was by coincidence. Two nuclei already having twin relations formed individually at two neighboring sites, as the twin relation already existed between the deformed grains, as shown in **Fig. 4-7a1** and **a2** (grains separated by the red Σ3 boundaries). Through growth, they got into contact, as shown in **Fig. 4-7a2**. The intragranular twins are those with triangular shape located at grain corners (Type A) or with thin lamellar morphology located within recrystallized grain (Type B to E), as illustrated in **Fig. 4-7c**. The formation of the intragranular twins during recrystallization processes have

been thoroughly studied by many investigations. They were formed either by growth accidents (such as corner twins) [60] or by forming specific boundary segment with low energy between the twinned part of the grain and the adjacent grain [61, 62].

In order to evaluate the contribution of the annealing twins to the recrystallization texture of the as-heated Cu foils, we further analyzed the area fraction and the crystallographic orientation features of the intragranular twins in the Cu foils heated to 450 ℃, as highlighted in purple in **Fig. 4-7d.** Their orientations weighted by their areas were represented with the φ_2 = 0°, 20°, 30°, 35°, 45° and 55° sections of the Euler space and are displayed in **Fig. 4-7e.** The results showed that although the intragranular twins formed in almost all the recrystallized grains, their area fraction is only about 6.62 % in the total recrystallized area. More importantly, as shown in **Fig. 4-7e**, the orientations of these twins are rather random, falling into the orientation background of the recrystallization texture. Thus, in the present study, the intragranular twins did not make sufficient contributions to the recrystallization texture of the as-heated Cu foils. The resultant recrystallization texture is mainly attributed to the orientations of the grown recrystallized grains.

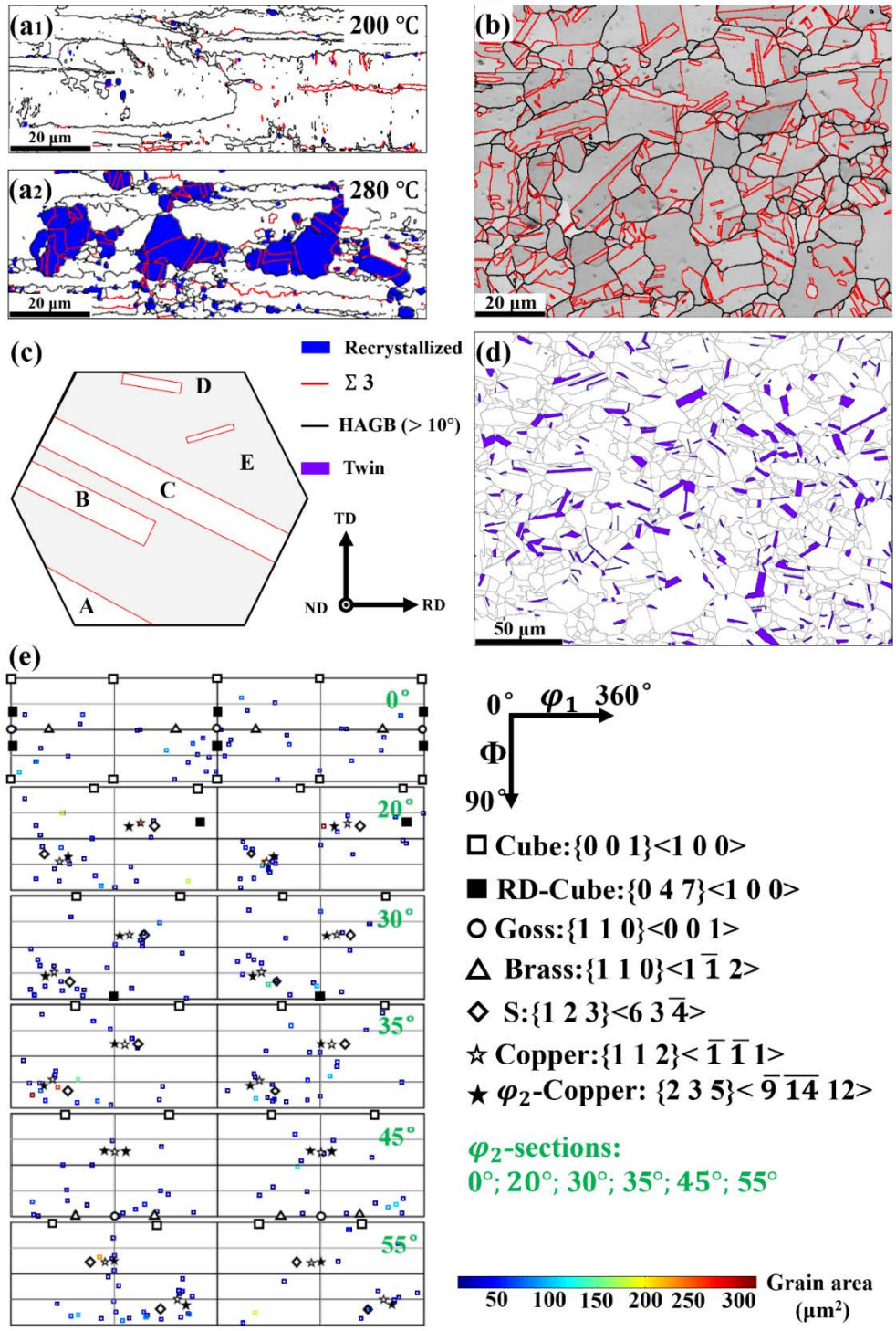

Fig. 4-7. Annealing twin in Cu foils heated to (a1) 200°C, (a2) 280 °C and (b) 350 °C. (c) Illustration of five typical intragranular twins observed in Cu foils. (d) Morphologies of intragranular twins (in purple) in Cu foils heated to 450 °C and (e) φ2= 0°, 20°, 30°, 35°, 45° and 55° sections of Euler space showing their orientations weighted by area with positions of ideal components in the same sections.

4.3.3.4 Thermal expansion of Cu and geometrical thermal constraint

During heating, thermal expansion of Cu foil should occur accompanying the microstructural and texture evolution. The expansion is usually represented by the d-spacing increase of the crystalline planes. Thus, the diffraction behavior of the present Cu foils under the synchrotron radiation was measured *in-situ* with the heating process. **Fig. 4-8a** and **b** show the d-spacing evolution of the {111} and the {200} planes in the RD (in-plane) and ND (out-of-plane) with the temperature from 40 ℃ to 500 ℃. It is seen from the figures that the d-spacing of the two planes in the two directions increase linearly with the temperature. However, for both planes, the expansion in RD is always smaller than that in ND. This anisotropic behavior is related to the geometry of the Cu foils. As in the present study the Cu foils are very thin (10 μm) as compared to the length or the width (4 mm), the foils possess a quasi 2D structure. The in-plane (foil plane or in the RD and TD) expansion was much constrained by such a geometry and the out-of-plane (normal to the foil plane or along the ND) expansion was free. Thus, the foils were subjected a biaxial thermal constraint during the heating process. Then, we further quantified the biaxial geometrical thermal strain, using the relative RD d-spacing referenced to the ND d-spacing at 40℃, as expressed by Eq. (4.1):

$$\varepsilon = \frac{d_{hkl_{RD}(T)} - d_{hkl_{ND}(T_0)}}{d_{hkl_{ND}(T_0)}}, \tag{4.1}$$

where $d_{hkl_{RD}(T)}$ is the RD d-spacing of planes *{h k l}* at temperature *T* and $d_{hkl_{ND}(T_0)}$ is the ND d-spacing at T_0 (40℃). The results of the geometrical thermal strains of the {111} and the {200} in the RD are displayed in **Fig. 4-8c**. It is seen that the two strains ($\{111\}_{Cu}$ and $\{200\}_{Cu}$) increased linearly with the temperature, demonstrating that the biaxial thermal constraint is elastic. Moreover, the two strains are very close, thus, the biaxial thermal constraint is quasi-isotropic in the foil plane.

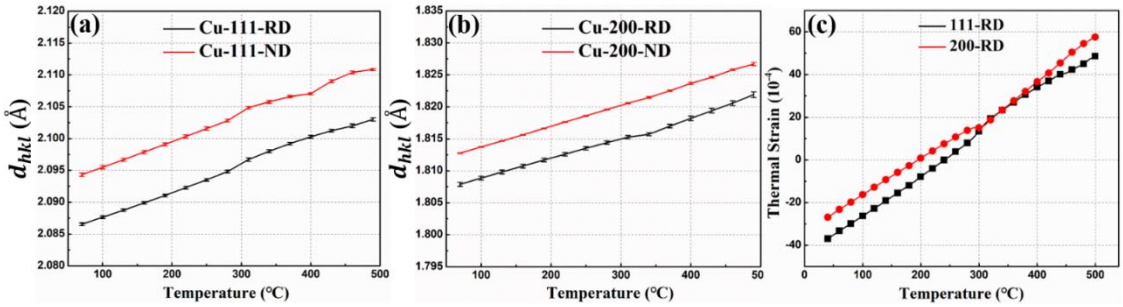

Fig. 4-8. Variations of d-spacing (d_{hkl}) of (a) {111} and (b) {200} planes in RD and ND; (c) biaxial thermal strain ε as a function of temperature.

4.4 Discussion

The above results show that the final recrystallization texture of the Cu foils (dominated by three pairs of rotated orientations (**Fig. 4-2d** and **e**)) is distinct from the orientations of the initial nuclei (close to the RD-rotated Cube orientations and along α fiber from the Goss to the Brass and close to the Copper and the S (**Fig. 4-6a** and **b**)). This means that selective grain growth occurred during the grain growth process and resulted in the recrystallization texture transition. Such a transition was, in fact, a result of several screening events by the microstructural factors and the geometrical factors of the samples. The intrinsic factors should be the deformation stored energy and the later grain boundary mobility. The extrinsic factors that are related to the 2D geometrical features of the sample are the biaxial thermal constraint and the surface energy. The deformation stored energy was dominant at the nucleation stage making the first screening, the geometrical factors became decisive when the recrystallized nuclei grew into large sizes through the foil thickness, and the grain boundary mobility took a dominant role when the coherent Σ3 boundaries were formed between grains with the two kinds of rotated orientations.

4.4.1 Effect of deformation stored energy

At the nucleation stage, the orientations of the nuclei were mainly inherited from the deformation orientation. The fact that nucleation occurred preferentially in low Taylor factor regions surrounded by high Taylor factor matrices or grains with high deformation heterogeneity indicates that the nucleation was still driven by the need to reduce the high stored

deformation energy. Due to the large deformation heterogeneity in some grains, especially the high Taylor factor ones, the low Taylor factor orientation regions existing in the highly deformed matrices should result from the orientation variation induced by the heterogeneous deformation. Such regions should possess specific dislocation configurations allowing quick recovery to form subgrains in the deformed matrices, as cell structures already existed in the deformed matrices in the present cold-rolled foils (**Fig. 4-1b2)**. This suggests that dynamic recovery [63] already happened during the rolling process. In consequence, the low Taylor factor orientation regions provided more early recovered regions that became potential nuclei for recrystallization when heating started. As these nuclei were highly disoriented with respect to their surroundings, their boundaries were highly mobile. Thus, they could grow rapidly through consuming their surroundings with high stored energy and demonstrated size preference at the nucleation stage. However, at this stage, as the sizes of the nuclei were still very small (1 to 2 μm in size) and isolated in the deformed matrices that possessed high hardness, the effect of the biaxial thermal constraint, the sample surface and the grain boundary mobility of the coherent Σ3 did not make any contribution to the screening effect.

4.4.2 Effect of biaxial elastic strain energy and surface energy

When the nuclei grew into large sizes through the foil thickness, the biaxial elastic strain energy and surface energy came into effect, because the thermal elastic constraint is accumulative being proportional to the sizes of the grains and the surface energy depends on the sizes of the surface areas occupied by the grains.

Under the biaxial elastic strain state, the elastic strain energy density of differently oriented crystals could be expressed as follows [29]:

$$W = 1/2 \cdot M\varepsilon_{(hkl)}^2, \tag{4.2}$$

where M is the biaxial elastic modulus and ε is the elastic strain of the *(h k l)* planes. As revealed by the *in-situ* synchrotron radiation diffraction measurement, the elastic thermal strain demonstrated an isostrain character (**Fig. 4-8c**). The strain energy densities of different texture components are mainly proportional to the corresponding biaxial elastic moduli. As analyzed

in **Chapter 4**, the elastic modulus can be derived from the stiffness tensor of the material. The biaxial moduli of the plane *(h k l)* in two in-plane directions - the RD and the TD - for the present cold-rolled foils can be expressed as follows [42]:

$$M_{RD}=[(C_{11}+2C_{12})(2C_{44}+(P-Q)H)]/(C_{12}+2C_{44}-QH)$$
$$M_{TD}=[(C_{11}+2C_{12})(2C_{44}+(R-Q)H)]/(C_{12}+2C_{44}-QH) \quad (4.3)$$

in which

$$P=a_{11}^2a_{31}^2+a_{12}^2a_{32}^2+a_{13}^2a_{33}^2$$
$$R=a_{21}^2a_{31}^2+a_{22}^2a_{32}^2+a_{23}^2a_{33}^2$$
$$Q=a_{31}^4+a_{32}^4+a_{33}^4$$
$$H=2C_{44}+C_{12}-C_{11}.$$

In the equations, C_{11}, C_{12} and C_{44} are the elastic constants of Cu, and a_{ij} (i ; j =1, 2, and 3) are direction cosines specifying the angle between the i^{th} axis of the Cubic crystal coordinate system and the j^{th} axis of the rolling coordinate system. For the rolling coordinate system or the Cubic crystal system, 1 stands for the RD or a-axis, 2 the TD or b-axis and 3 the ND or c-axis.

For the surface effect, as large surface areas were involved in the grown recrystallized grains, it also played an important role to grain growth, especially when the grains grew through the thickness of the foil and became flat columns through the foils. For the surface energy, we used the surface energy density data simulated by Zhang et al. in the frame of the modified embedded-atom method of Cu crystals [64] for the analysis.

Based on the two above theoretical analyses, we calculated the biaxial moduli in the respective RD and TD on the foil plane and the surface energy density of all possible orientations of Cu crystals and displayed the calculation results in the orientation space in **Fig. 4-9** and **10,** respectively. The corresponding ODF sections of the Cu foil heated to 450°C from **Fig. 4-2d** but represented only with intensity line contours is also superimposed on the figures in **Fig. 4-9** and **10** for comparison. The biaxial moduli and the surface energy density of the ideal orientations of the nuclei and the final recrystallization texture components are also listed in **Table 4-2**.

It is seen from **Fig. 4-9** and **Fig. 4-10**, the preferences either by the strain energy or by the surface energy is always in two opposite extremes. The most favorable orientations by the strain energy are the θ-fiber [65] with {100} parallel to the foil plane, but these orientations are the unfavourable orientations by the surface energy. Vice versa, the most favorable orientations by the surface energy are the γ-fiber [65] with the {111} parallel to the foil plane, but these orientations are the most unfavorable orientations by the strain energy, as shown in **Table 4-2**. As revealed by the present results, neither the orientations in the θ-fiber nor those in the γ-fiber were found in the final recrystallization texture components. The more pronounced hindrance happened to the orientations that are near the Cube component. Such orientations are typical and important recrystallization components of many cold-deformed bulk FCC metals [1, 17, 18, 61, 66-68]. These orientations indeed existed in the nucleation stage in the present work and demonstrated size preference (**Fig. 4-6a**). However, they did not further develop into an important component. The selected orientations are, to some extent, in compromise to the two opposite effects. From the biaxial moduli and the surface energy densities of the surviving components just after the recrystallization at 350 °C, listed in **Table 4-2**, one can see that they have more or less moderate biaxial moduli and surface energy density. However, among them the Goss orientation possesses the highest TD biaxial modulus (281.7 GPa), thus its growth is not favored by the elastic thermal strain energy. Indeed, its proportion was relatively low at 350 °C (5.01 % (**Fig. 4-5c)**) and further decreased during the heating to 450 °C (3.59 % (**Fig. 4-5c**)). For the other deformation components, the Brass, the S and the Copper components, they have both moderate biaxial moduli and moderate surface energy densities, thus they survived the recrystallization and indeed they were not eliminated. However, during the growth process from 350 °C to 450 °C their area fractions decreased or stayed unchanged (**Fig. 4-5c**). In contrast, although the φ_2-rotated Copper crystals have very similar biaxial moduli and surface energy intensity values to those of the three components, its area fraction is much higher at the completion of recrystallization. Moreover, during the growth process, its amount was even further increased. Another anomaly happens to the RD-rotated Cube component. Although it possesses favorable biaxial moduli (**Table 4-2**), its surface energy density is much higher.

Even so, its area fraction is the second highest and even slightly increased during the growth process. These two anomalies should be related to the effect of the second microstructural factor, boundary mobility.

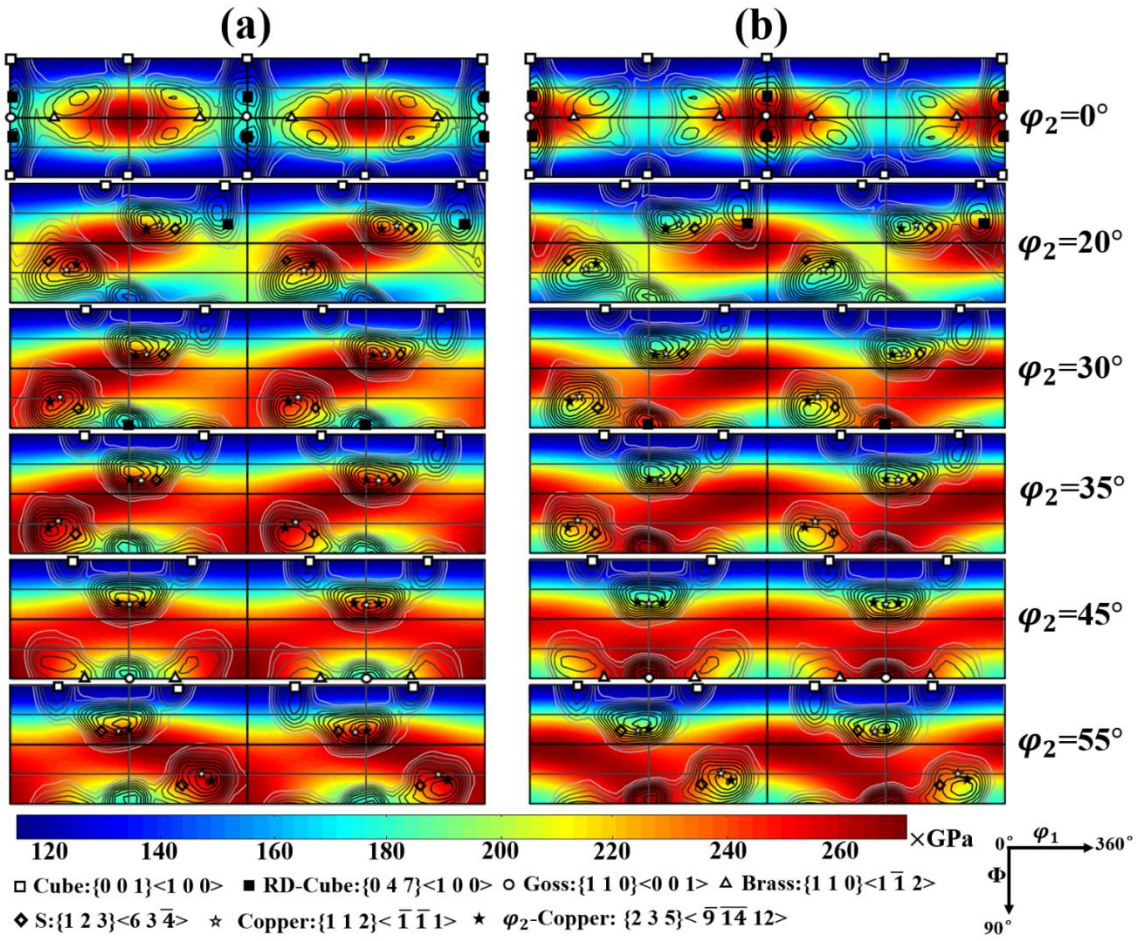

Fig. 4-9. φ_2 = 0°, 20°, 30°, 35°, 45° and 55° sections of biaxial moduli along (a) RD and (b) TD as a function of crystal orientation in orientation space.

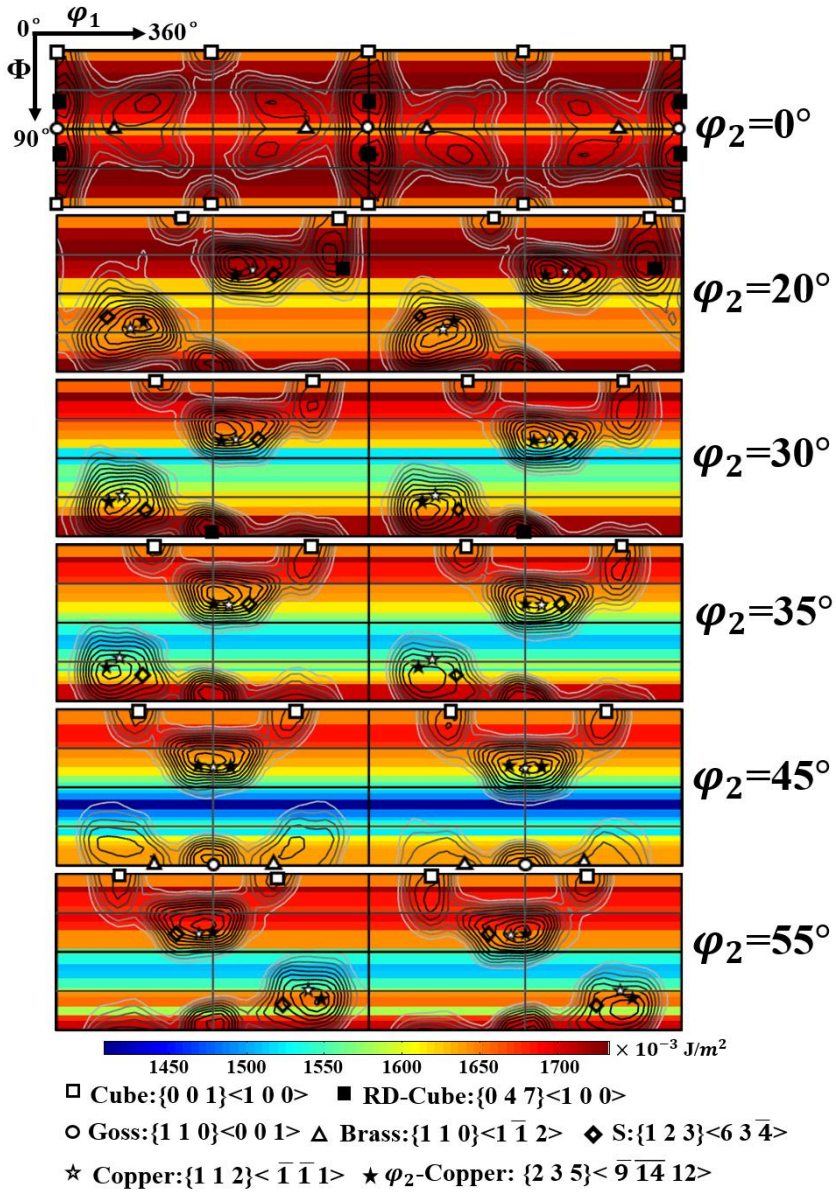

Fig. 4-10. φ_2= 0°, 20°, 30°, 35°, 45° and 55° sections of surface energy density as a function of crystal orientation in orientation space.

Table. 4-2. Calculated values of average, RD and TD biaxial elastic moduli and surface energy for recrystallized components of cold-rolled Cu foil. For reference, the corresponding values of θ-fiber and γ-fiber are also displayed.

Component	**Euler angles**	**$M_{average}$ /(GPa)**	**M_{RD}/(GPa)**	**M_{TD}/(GPa)**	**Surface energy density/(10^{-3} J/m^2)**
Goss	(0, 45, 0)	233.3	184.8	281.7	1640.9
Brass	(35, 45, 0)	233.3	216.7	249.8	1640.9
S	(59, 37, 63)	234.1	234.6	233.7	1656.6
Copper	(90, 35, 45)	232.5	248.6	216.3	1611.5
RD-Cube	(0, 30, 0) (0, 60, 0)	209.2	170.6	247.8	1711.8
φ_2-rotated Copper	(90, 35, 35) (90, 35, 55) (49, 62, 22) (30, 71, 30)	231.5	250.7	211.9	1645.8
θ-fiber		114.8	114.8	114.8	1650.9
γ-fiber		261.0	261.0	261.0	1408.6

4.4.3 Effect of interface mobility

We further calculated the disorientation between the components in **Table 4-2**. We found that only the RD-rotated Cube and the φ_2-rotated Copper possess a near Σ3 relation or a twin relation. As we observed in the microstructure, the grains with the two orientations are always adjoining each other and separated by a coherent {111} plane (**Fig. 4-4d$_1$**). Thus, during the growth process, when they got in contact, the coherent {111} boundaries functioned as a kind of "pins" that could stabilize the two components, especially the RD-rotated Cube with high surface energy. Moreover, the anisotropic biaxial moduli of the two components are complementary in the RD and in the TD directions, i.e., if one is higher, the other is lower in the same direction (**Table 4-2**). This decreases the average moduli of their agglomerates in the

two directions (**Fig. 4-4d1)**. Thus, during the growth process, the φ_2-rotated Copper components could easily grow by consuming the other components (the Brass, the S and the Copper) in their neighbor, as there are no specific orientation relationships between them and the boundaries are of high-angle random ones. In this way, the amount of φ_2-rotated Copper components was further increased during the growth process with the decrease of the Brass, the S and the Copper components, but the amount of the RD-rotated Cube was stabilized by the coherent boundaries.

4.5 Summary

In this chapter, the texture evolution of the cold-rolled Cu foil with thickness of 10 μm during the recrystallization process was thoroughly investigated through texture measurements by neutron and synchrotron radiation diffraction and thermal lattice strain measurement by *in-situ* synchrotron radiation diffraction at macroscopic scale and through spatially correlated microstructure and crystallographic orientation characterization by SEM-EBSD at meso- to microscopic-scale. The nucleation sites and the orientation features of the recrystallization grains during the nucleation process and the microstructure evolution during the subsequent grain growth were statistically investigated. The experimental results revealed that the orientations of the recrystallized parts evolved constantly through selective growth by four major screening factors.

1. At the nucleation state, the orientations of the nuclei were mainly inherited from the deformation texture components and clustered at two orientation locations. One is from the Cube to the RD-rotated Cube and along the α skeleton line from the Goss to the Brass. The other is along the β fiber covering the Copper, the S and the φ_2-rotated Copper. The first cluster demonstrated size preference, especially the Cube orientation. At this state, the screening factor is the deformation stored energy. Those with low Taylor factors surrounded with high Taylor factor deformation matrices had the preference in nucleation and growth.

2. When the recrystallized nuclei grew to certain sizes (through the foil thickness) during heating, the geometrical 2D features of the foils induced orientation dependent biaxial thermal constraint and imposed orientation dependent surface constraint to the grown grains. The nuclei

with both moderate biaxial moduli in the foil plane and moderate surface energy densities were favored for further growth. Under such constraints, the RD-rotated Cube and the Brass orientations in the first cluster and the near Copper, the near S and the φ_2-rotated Copper orientations survived at the completion of the recrystallization.

3. During the post-recrystallization grain growth, the twin relations between the RD-rotated Cube and the φ_2-rotated Copper grains produced coherent {111} interfaces when the two grew into contact. Such immobile boundaries stabilized the two orientations. The agglomerates of the two oriented blocks further benefited from the complementary anisotropic biaxial moduli. The relative higher moduli of the φ_2-rotated Copper oriented crystals was compensated by the relatively low moduli of the RD-rotated Cube oriented crystals. Such a combination allowed a preferential growth of the φ_2-rotated Copper crystals at the expense of the other surviving orientations that had no specific orientation relationships and were delineated by the random high-angle boundaries.

The present study provided exhaustive information on the recrystallization texture transition characterized from the oriented nucleation at the nucleation stage to the oriented growth at the growth stage governed by both the intrinsic microstructural factors and the extrinsic sample geometrical factors. The results from this work contributes to deepening the understanding of the recrystallization phenomena.

Chapter 5 Effect of GNS on recrystallization texture evolution of Cu/GNS composite with Cu foil thickness of 10 μm

5.1 Introduction

Graphene nanosheets (GNSs) reinforced Copper (Cu) matrix composites were normally fabricated to increase the mechanical and physical properties of pure Cu [69, 70]. Inspired by the microstructure of shell in nature, the laminated Cu/GNS composite was designed to further improve the mechanical properties of the Cu/GNS composites by constructing a layered structure in the composite [19, 71-76]. The incorporated GNSs as well as the constructed layered structure could impose great impact on the recrystallization of Cu during heating, which is expected to greatly influence the mechanical properties of the as-fabricated laminated Cu/GNS composites. Because the design of such a Cu-GNS-Cu layer structure is totally a new subject, the recrystallization features of Cu in this composite is unknown. The thermal expansion mismatch between GNSs and Cu could generate thermal constraint to Cu, and Cu-GNS-Cu layered structure could influence the grain growth process.

Motivated by these considerations and based on the results obtained in Chapter 4, the recrystallization features of Cu/GNS composites with Cu layer thickness of 10 μm was thoroughly investigated by means of SEM-EBSD for microstructure observation, synchrotron radiation diffraction for texture measurement and *in-situ* synchrotron radiation for lattice strain evolution characterization. The obtained results could provide useful information for better understanding the recrystallization of Cu/GNS composites and the revealed mechanisms is potential for instructing the fabrication of composites with desired recrystallization texture.

5.2 Experiments

In this chapter, the 10 μm thick cold-rolled Cu foils and the GNSs with thickness of around 1~5 nm were employ as the raw materials. The GNSs were deposited on the Cu foil surfaces using an electrophoretic deposition technique to synthesis the basic unit of the Cu/GNS composite. The as-deposited Cu foils were stacked and sintered to as-sintered bulk Cu/GNS

composite using the hot-pressing sintering method under vacuum. The stacked Cu/GNS foils were also heated to 150 ℃, 200 ℃, 280 ℃, 350 ℃, 450 ℃, and 700 ℃, respectively. The detailed information on sample preparation can be found in § 3.2.2.

The microstructure of the as-sintered and as-heated Cu and Cu/GNS samples were characterized by SEM-EBSD. The texture of different states of samples were measured by neutron and synchrotron radiation diffraction. The evolution of the lattice strains of Cu in the the Cu/GNS samples during the heating process was investigated by a 4D *in-situ* synchrotron radiation diffraction technique (3D space + 1D time). The software StressTextureCalculator (SteCa2-2.0) was used to extract the pole figure intensity data. The EBSD data were processed with the home-made software ATEX and the ODFs were calculated with the incorporated package in ATEX using a series expansion method. The Debye-Scherrer rings were integrated to the diffraction patterns with the Fit2D package, and the data from the LaB_6 powder measurement was used to subtract the instrumental effect. The information contained in the peak profile, such as the integrated intensity (I) and the Bragg angles (2θ) of the peaks at each measured temperature were extracted.

5.3 Results and discussions

5.3.1 Texture and microstructure evolution of Cu/GNS during heating

5.3.1.1 Texture and microstructure evolution of Cu/GNS before foils sintered into bulk

Fig. 5-1 shows the ODF sections (φ_2 = 0°, 20°, 30°, 35°, 45° and 55°) of the Cu/GNS composite samples heated to 150 ℃, 280 ℃, 350 ℃, 450 ℃ and 700 ℃, respectively, with the ideal orientations for reference. In general, compared with the as-heated pure Cu stacks (shown in **Fig. 4-2**), the Cu/GNS composite possess similar texture patterns and intensities at each corresponding temperature. The Cu/GNS samples also demonstrate a texture transition from the cold-rolling texture to a recrystallized texture dominated by two rotated components, i.e., RD-rotated Cube and φ_2-rotated Copper, as found in the pure Cu samples (**Table 4-1** and **Fig. 4-2**). The only noticeable variation lies at 280 ℃. At this temperature, compared with the pure Cu stack (**Fig. 4-2b**), the Cu/GNS composite possess similar texture pattern but the maximum

intensities of components in the Cu/GNS sample is lower (maximum texture intensity of 6.84 m.r.d for Cu/GNS and 8.66 m.r.d for Cu).

When the temperature is below 700 ℃, neither the pure Cu stacks nor the Cu/GNS stacks were sintered into bulk materials. In other words, each Cu foil still stays individually. In this way, the texture evolution occurs independently in each single Cu layer, so that the Cu and the Cu/GNS composites present a similar texture evolution features at the same temperatures. For the lower texture intensity of Cu/GNS at 280 ℃, it should be related to the GNSs. From 150 ℃ to 280 ℃, recovery and recrystallization of the cold-rolled Cu occurred. The addition of the GNS could accelerate this process by stimulating nucleation [77, 78], which means that the GNSs may provide additional nucleation sites in the deformed matrix. Then, recrystallization was more advanced in the Cu/GNS samples than in the pure Cu sample at the same temperature. In this way, the deformed texture was weakened more quickly in the Cu/GNS composites and thus present a lower texture intensity.

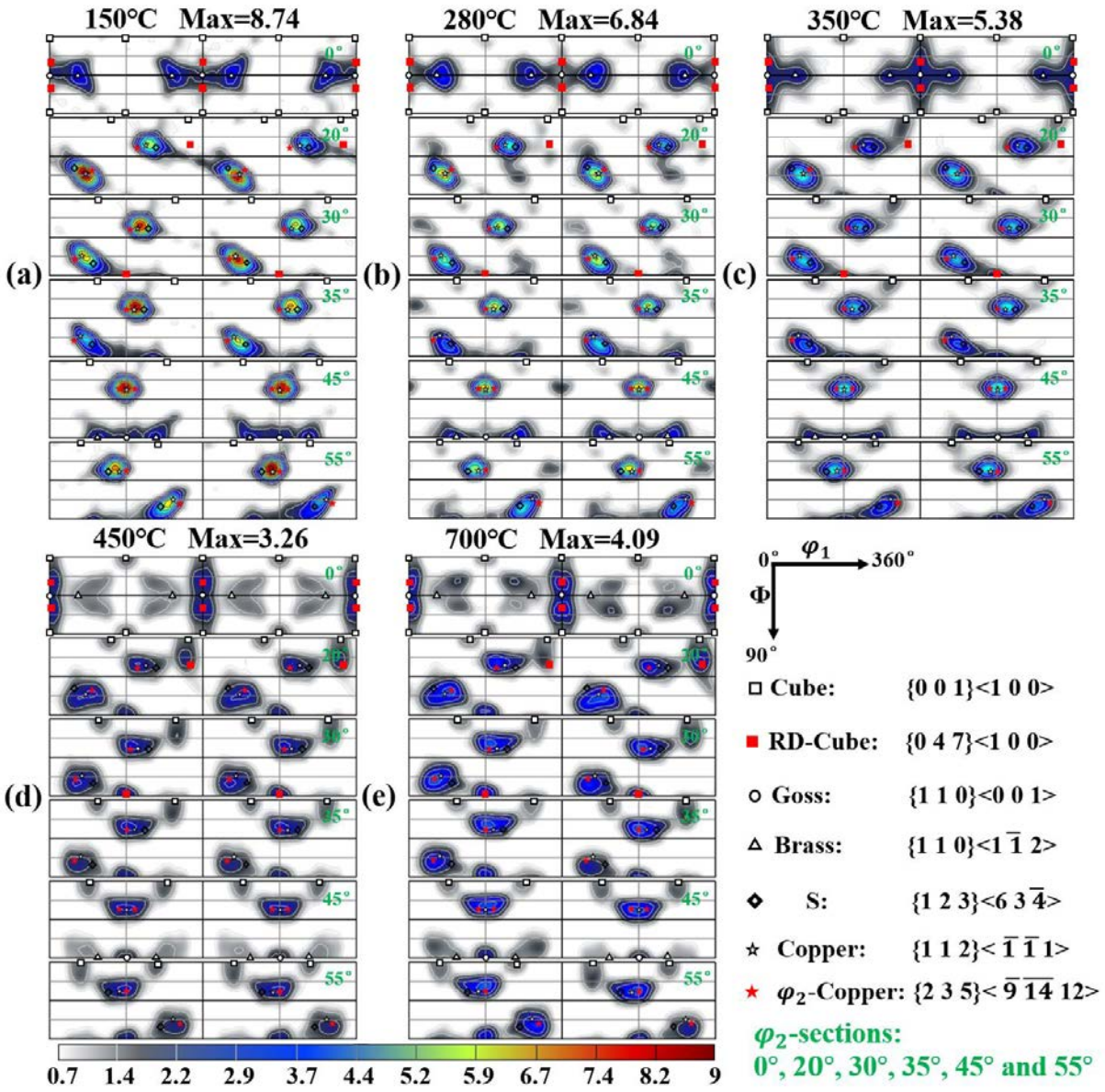

Fig. 5-1. ODF sections (φ_2 = 0°, 20°, 30°, 35°, 45° and 55°) of Cu/GNS composites heated to **(a)** 150 °C, **(b)** 280 °C, **(c)** 350 °C, **(d)** 450 °C and **(e)** 700 °C.

The microstructure evolution of the Cu/GNS composites at different temperatures were also investigated. As displayed in **Fig. 5-2**, the SEM-EBSD texture component micrographs of Cu/GNS heated to 200 ℃, 280 ℃, 350 ℃ and 450 ℃, the microstructure is similar to that of the pure Cu at the same temperature. At low heating temperatures, the microstructures were largely occupied by the band shape deformed grains (as displayed in **Fig. 5-2a** and **b_1**). With the increased temperature, the deformed matrix was progressively consumed by the growth of the recrystallized grains. It should be noted that, at 280 ℃, the recrystallized area fraction

reached 11.8 % in the Cu/GNS composite which is higher than that of the pure Cu (10.32 %), confirming that recrystallization progressed more in advance in the Cu/GNS than that in the pure Cu. Additionally, the distribution of the recrystallized grains is relatively homogeneous although the agglomerates of the recrystallized grains were also observed. When further increased the heating temperature to 350 ℃ and 450 ℃, the microstructure of the Cu/GNS obey the similar manner to that of the pure Cu. At 350 ℃, the texture is dominated by a mixed orientations of cold-rolling and new recrystallized components and at 450 ℃ it is mainly dominated by the new recrystallized components (RD-rotated Cube and φ_2-rotated Copper).

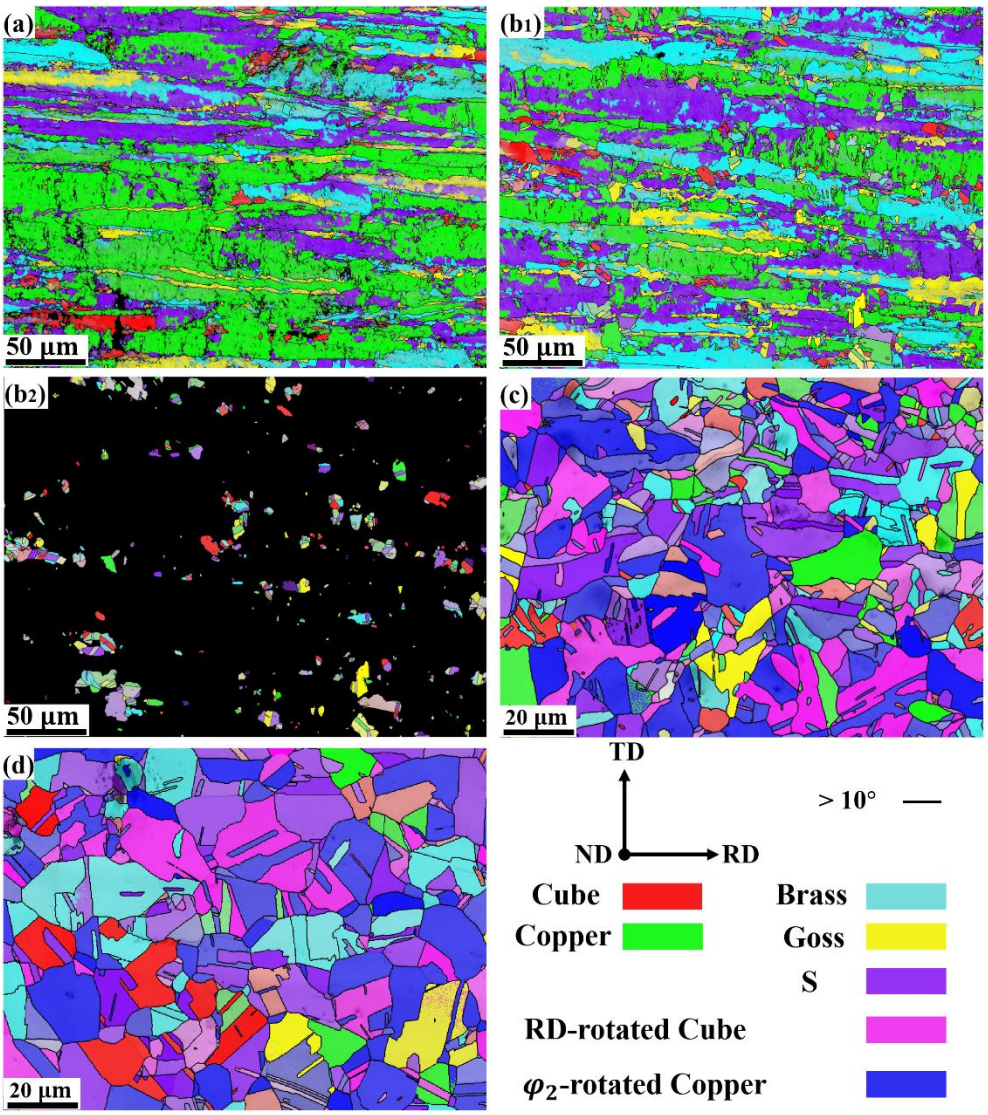

Fig. 5-2. SEM-EBSD texture component micrographs of Cu/GNS heated to (a) 200 ℃, (b_1) 280 ℃, (c) 350 ℃ and (d) 450 ℃. Partition of recrystallized grains in Cu/GNS heated to 280 ℃ (b_2).

5.3.1.2 Texture and microstructure features of Cu/GNS after foils sintered into bulk

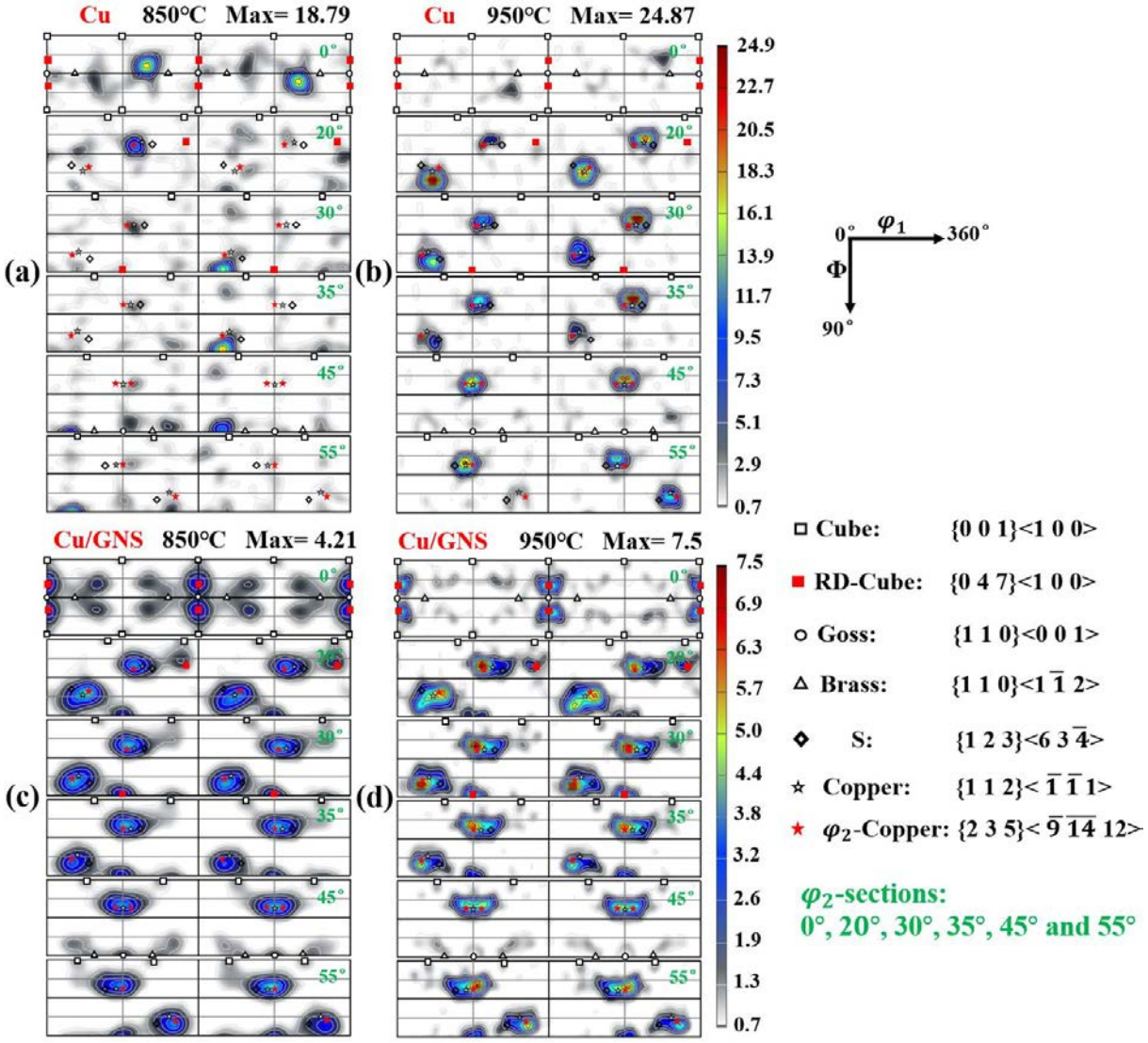

Fig. 5-3. ODF sections (φ_2 = 0°, 20°, 30°, 35°, 45° and 55°) of Cu heated to **(a)** 850 °C, **(b)** 950 °C and Cu/GNS heated to **(c)** 850 °C and **(d)** 950 °C.

When the pure Cu and the Cu/GNS samples were heated to higher temperatures and sintered into bulk blocks, textures with pronounced components developed separately in the two kinds of samples. **Fig. 5-3** shows the ODF sections (φ_2 = 0°, 20°, 30°, 35°, 45° and 55°) of both the pure Cu and Cu/GNS composite samples heated to 850 °C and 950 °C, respectively, with the ideal orientations for reference. For the pure Cu, the texture evolved from the two kinds of rotated components to a few individual orientations. Some are very strong and the others are weakas shown in **Fig. 5-3a** and **b**. The two dominant rotated components totally disappeared,

especially the RD-rotated Cube component, whereas the Copper component became absolutely dominant instead.

As for the Cu/GNS composite, the texture is still present with the two rotated components with increased intensity (maximum texture intensity of 7.5 m.r.d at 950 °C).

Fig. 5-4 shows the TD plane SEM-EBSD texture component micrographs of Cu heated to 850 ℃ and 950 ℃ and of Cu/GNS heated to 950 ℃. It is clearly seen that at 850 ℃ some parts of the Cu foils were sintered into bulk and abnormal grain growth occurred in these parts (**Fig. 5-4a**), forming very heterogeneous sized grain structure. The sizes of grown ones amount to several millimeters in the foil plane. At these places, the grain growth was no longer confined within a single foil layer that means the initial foil surfaces were swept off. The grains that experienced abnormal growth and the those confined in the Cu foil possess different orientation features. For the former, their orientation is close to the φ_2-rotated Copper component (**Fig. 5-4a**), whereas, for the latter, they still possess the similar orientations with those at 700 ℃ (*i.e.*, dominated by the RD-rotated Cube and the φ_2-rotated Copper).

When the heating temperature increased to 950 ℃, all the Cu foils in the pure Cu were sintered into one bulk and the microstructure is represented with a few coarse grains and no layer could be spotted any more. The microstructure of the pure Cu is occupied with the S, the Copper and the φ_2-rotated Copper oriented grains but the Copper component possesses size preference (**Fig. 5-4b**). However, for the Cu/GNS composite, even at this temperature, the layered structure was well conserved with the layer structure clearly visible as displayed in **Fig. 5-4c**, although the Cu foils with CNSs were already sintered into one bulk. Grain growth in Cu/GNS is still confined within each Cu layer. In each layer, the grains of the two rotated orientations are always observed adjoining each other.

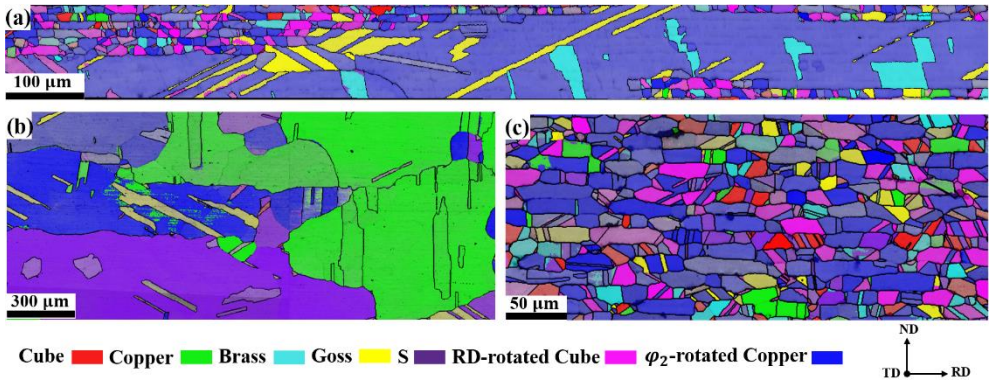

Fig. 5-4. SEM-EBSD texture component micrographs of TD plane of Cu heated to (a) 850 ℃, (b) 950 ℃ and of Cu/GNS heated to (c) 950 ℃.

5.3.2 Effect of GNS on the lattice strain evolution of Cu foils

To reveal the possible influences of the GNS, the lattice strain evolution of Cu during heating was studied by a 4D synchrotron radiation diffraction measurements. The d-spacing changes of {111} and {200} planes of Cu in the pure Cu and the Cu/GNS samples from room temperature to 500 ℃ were measured. Similar to the case of the pure Cu foils in Chapter 4, the change of the d-spacing of the lattice planes perpendicular to the RD was used to analyze the in-plane (foil plane) strain (**Fig. 5-5a**), and the change of the d-spacing of the lattice planes perpendicular to the ND the out-of-plane strain (**Fig. 5-5a**). **Fig. 5-5a** and **b** shows the RD and ND d_{hkl} of the $\{111\}_{Cu}$ and $\{200\}_{Cu}$ planes of the Cu foils in the pure Cu and in the Cu/GNS samples. It is seen that, in general, the d_{hkl} of each lattice plane increases linearly with the temperature. The difference in d_{hkl} between the RD and ND is due to the 2D feature of the thin Cu foils. Interestingly, the d_{hkl} of the same lattice plane for Cu in the pure Cu sample and for Cu in the Cu/GNS sample is very close, especially for the $\{200\}_{Cu}$ planes and at temperatures below 300 ℃. It seems that the deposited GNS did not exert much constraint to the expansion of the Cu foils.

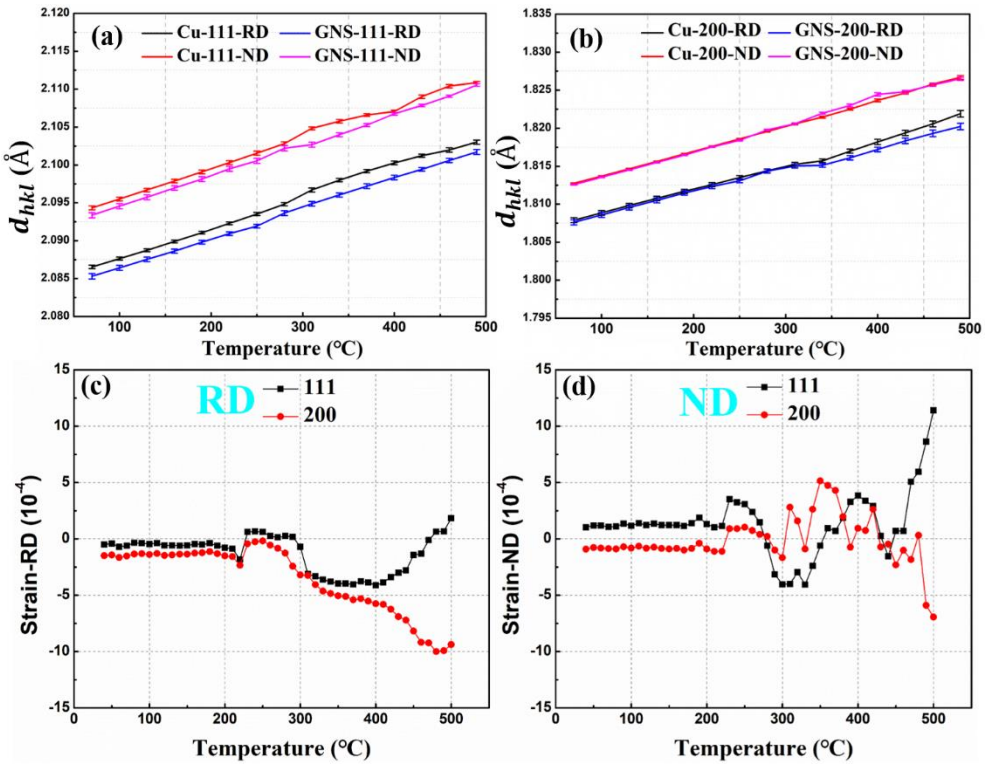

Fig. 5-4. Comparison of dhkl of (a) {111}Cu, (b) {200}Cu of the two samples and relative lattice strains of Cu in Cu/GNS with respect to that of Cu in pure Cu (c) in RD (in-plane) and (d) in ND (out-of-plane).

In order to evaluate the constraint, the relative elastic strain of Cu/GNS with respect to the pure Cu at the same temperature was calculated with **Eq. (5.1)**:

$$\varepsilon = \frac{d_{hkl_{GNS/Cu}(T)} - d_{hkl_{Cu}(T)}}{d_{hkl_{Cu}(T)}}, \tag{5.1}$$

where $d_{hkl_{GNS/Cu}(T)}$ and $d_{hkl_{Cu}(T)}$ are the d_{hkl} of Cu in the Cu/GNS and in the pure Cu sample at temperature T.

The results are displayed in **Fig. 5-5c** and **d**. It is seen that relative strains are located horizontally around zero and become dispersed when temperature goes high. Thus, the GNS exerted almost no constraint to the Cu. This may because the Cu foils are too thin (thickness of 10 μm) and geometrical constraint is much more pronounced. The confinement effect of the GNSs were largely overwhelmed by the sample geometrical effect.

The different texture and microstructure evolution at higher temperature in the two kinds of samples is surely attributed to the GNSs, although no obvious thermal constraint was detected. When the heating temperature is not high enough (< 700 ℃), the recrystallization and

subsequent grain growth was still confined within each single Cu layer. In this way, the microstructure and texture evolution in Cu and the Cu/GNS were driven by the same factors (microstructural and sample geometrical). As they possess similar recrystallization and grain growth features in terms of microstructure and texture, there was no effect from the GNSs. This is different from the case of the Cu/GNS composite with 30 μm thick Cu foils. The results and analyses will be detailed in the next chapter (Chapter 6). However, when the heating temperature was high enough, in the pure Cu, the growth of the recrystallized grains could overpass the Cu layer interfaces. As a result, the interlayer interfaces were removed and the foil shape induced geometrical factors like, surface energy and biaxial strain energy no longer exist in the Cu bulk. Thus, the grain growth follows the same rules for the bulk Cu, *i.e.*, driven by the reduction of the grain boundaries, and the grains with large sizes were then favored. Differently, for the Cu/GNS composite, the existence of the GNS layers working as a barrier for atom diffusion and prevent the grown grains from penetrating into the adjacent Cu layers. Thus, the layer structure was conserved in the Cu/GNS composites even at high temperature and the layer shape induced sample geometrical factors always worked in the composites. Moreover, grain growth was impeded by the interfaces of the GNSs layers, and the microstructure and texture were stabilized to the end of the sintering and the abnormal grain growth was totally suppressed.

5.4 Summary

In this chapter, the effect of the GNS on the microstructure evolution, texture evolution and lattice strain evolution of 10 μm thick Cu foils during heating were investigated by SEM-EBSD, synchrotron radiation diffraction and *in-situ* synchrotron radiation, respectively. The incorporated GNSs maintained the layered structure in the Cu/GNS composite and thus yield a distinct recrystallization texture in comparison with that of pure Cu sample after being sintered at high temperature.

When the heating temperature is not high enough (< 700 ℃), the deposited GNSs do not affect the recrystallization and grain growth of the Cu. The Cu/GNS composites present the similar microstructure and texture features compared with those of the 10 μm thick Cu foils.

The effect of the GNSs stood out after the samples were sintered to higher temperatures (> 700 ℃). With the existence of the GNS layer, the growth of the Cu grains was confined within each Cu layer and the bulk Cu/GNS composites could be regarded as many individual Cu layers. The adhered GNSs worked as layer barriers for the penetration of the grown Cu grains to the neighboring layers. In this way, the abnormal grain growth was suppressed. As a result, the recrystallization texture of the bulk Cu/GNS composites is similar to that of the Cu foils dominated by the RD-rotated Cube and the φ_2-rotated Copper components.

Chapter 6 Elastic Strain Induced Abnormal Grain Growth in laminated Cu/GNS composites

6.1 Introduction

Recrystallization and grain growth are intrinsic processes of metallic materials occurring inevitably when the material is thermally treated after cold plastic deformation. Certain orientation related stimuli, such as orientation related strain and surface energy, may cause abnormal grain growth and completely modify the recrystallized microstructure and texture [20-22, 30-33, 79]. As the microstructural and texture transformation significantly affect the properties of the materials, the determination and interpretation of recrystallization texture are of both fundamental and practical importance in materials processing. Thus, study on the origin of recrystallization and grain growth has been intensive for decades for the purpose of practical property control and theoretical microstructure process simulation. In this chapter, the microstructure, texture and lattice strain evolution of the GNS/Cu composite were examined referenced to the Cu stack without GNSs by *ex-situ* and *in-situ* orientation characterization techniques. The microstructure and texture of the as-cold-rolled, as-sintered and as-heated Cu and Cu/GNS samples were firstly explored. Then, the thermal expansion of Cu and Cu/GNS during heating and the relative lattice strains induced by GNS were analysed. Finally, the elastic strain energy of differently oriented Cu crystals was calculated and its effect on recrystallization and grain growth was analyzed.

6.2 Experiments

In this chapter, the materials used are the cold-rolled Cu foils with thickness of 30 μm and graphene nanosheets (GNSs) with thickness of around 1~5 nm. The stacked Cu foils with and without GNSs were heated to 150 ℃, 170 ℃, 230 ℃, 350 ℃, 450 ℃, 700 ℃ and 950 ℃, respectively. The detailed information on sample preparation can be found in § 3.2.2. The microstructure of the as-cold-rolled, as-sintered and as-heated Cu and Cu/GNS samples were characterized by SEM and EBSD. The texture of different states of samples were measured by

neutron diffraction. The software StressTextureCalculator (SteCa2-2.0) was used to extract the pole figure intensity data. The evolution of the lattice strains of Cu in the Cu and the Cu/GNS samples during the heating process was investigated by the 4D *in-situ* synchrotron radiation diffraction technique (3D space + 1D time). The Debye-Scherrer rings were integrated to the diffraction patterns with the Fit2D package, and the data from the LaB_6 powder measurement was used to subtract the instrumental effect. The information contained in the peak profile, such as the integrated intensity (I), the Bragg angles (2θ) of the peaks and the full width at half maximum (FWHM) at each measured temperature were extracted.

6.3 Results

6.3.1 Initial microstructure and texture of as-cold-rolled Cu foil

Fig. 6-1 displays an SEM-EBSD RD-axis inverse pole figure (RD-IPF) micrograph of the RD-ND plane of the as-cold-rolled Cu foil. It is seen that the cold-rolled Cu foil possesses banded microstructure composed of grains elongated in the RD. The orientation of the deformed grains were further analyzed and represented with the respective texture component micrograph in **Fig. 6-1b**. It is clearly seen that the cold-rolled grains possess the Copper, the Brass, the Goss, the Cube and the S orientations that are the typical texture components of the cold-rolled FCC metals.

Fig. 6-1c shows the $\varphi_2 = 0°$, 45° and 60° sections of the orientation distribution function (ODF) of the cold-rolled foils measured by through-volume neutron diffraction. For reference, the ideal positions of the cold-rolled texture components are also indicated in the figure. It is seen from the measured ODF sections that macroscopically the texture of the present cold-rolled foils is also characterized by the five typical cold-rolled texture components: Copper, S, Brass, Goss and Cube, among which the Copper component is the strongest, the S the second and the Cube the weakest. Moreover, the Brass component spreads toward the Goss orientation along the α skeleton line ($\varphi_2 = 0°$ and 45° sections) and the Copper and the S components spread toward the Cube orientation ($\varphi_2 = 45°$ and 65° sections).

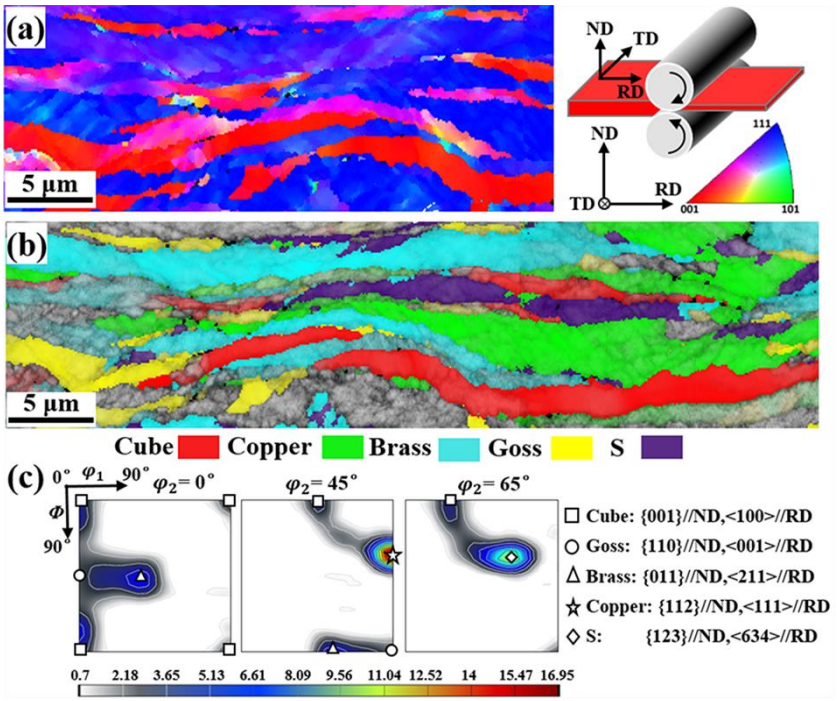

Fig. 6-1. Microstructure and texture of initial as-cold-rolled Cu foils. (a) SEM-EBSD RD inverse pole figure (RD-IPF) micrograph. (b) SEM-EBSD micrograph colored according to orientation of cold-rolled texture components of FCC metals. (c) Typical φ2= 0°, 45° and 65° sections of orientation distribution function (ODF) [46] measured by neutron diffraction (ideal texture components of cold-rolled FCC materials are detailed and indicated).

6.3.2 Microstructure and texture of as-sintered pure Cu and Cu/GNS

After sintering, the microstructures and textures in the two kinds of samples are in great contrast, although the initial banded structure in each Cu foil in both the pure Cu and the Cu/GNS sample was replaced by fully recrystallized coarse grains, as shown in **Fig. 6-2**, the SEM-EBSD RD-IPF micrographs from the RD-ND plane of the as-fully-sintered multilayered pure Cu and Cu/GNS samples together with the corresponding neutron diffraction ODF sections. For the pure Cu (**Fig. 6-2a**), it is composed of several coarse grains with the sizes in millimetre range and the texture is characterized by strong individual orientations. Although the microstructure of the pure Cu was obtained from the sample containing 100 layers of the cold-rolled foils, no layer interfaces can be identified within the coarse grains. The grain boundary migration during grain growth already overcame the confinement of the layer surfaces. However, for the Cu/GNS composite, the microstructure is clearly layered and mainly

composed of rectangular blocks delineated by the layer interfaces (the horizontal ones) where the GNSs were deposited and with the boundaries nearly perpendicular to the layer interfaces (the vertical ones). Moreover, most of the boundaries are low-angle boundaries (< 15°, yellow lines in **Fig. 6-2b**). Although each block has its own distinct orientation, they are very close to the Cube orientation. Very occasionally, non-Cube oriented grains can be spotted (light to bright blue ones). Most of these grains are twin related with their neighbouring Cube oriented blocks and the boundaries between them are the Σ3 coincident site lattice (CSL) boundaries. Such boundaries are less mobile [2], hence survived the abnormal growth of the Cube grains. The through-volume neutron diffraction ODF sections ($\varphi_2 = 0°$ and 45°) in **Fig. 6-2b** confirmed that in the whole measured sample volume ($4\times10\times2$ mm^3) the Cube orientation is clearly dominant, thus, the microstructure displayed in **Fig. 6-2b** is throughout the whole treated sample. The layered microstructure in the Cu/GNS sample suggests that recovery, recrystallization and then the abnormal grain growth occurred only within each foil and did not overpass the foil surfaces on which the GNSs were deposited. The orientation feature of each Cu foil infers that the Cube oriented grains had the absolute privilege to survive and grow by consuming the other orientation grains until they joined each other.

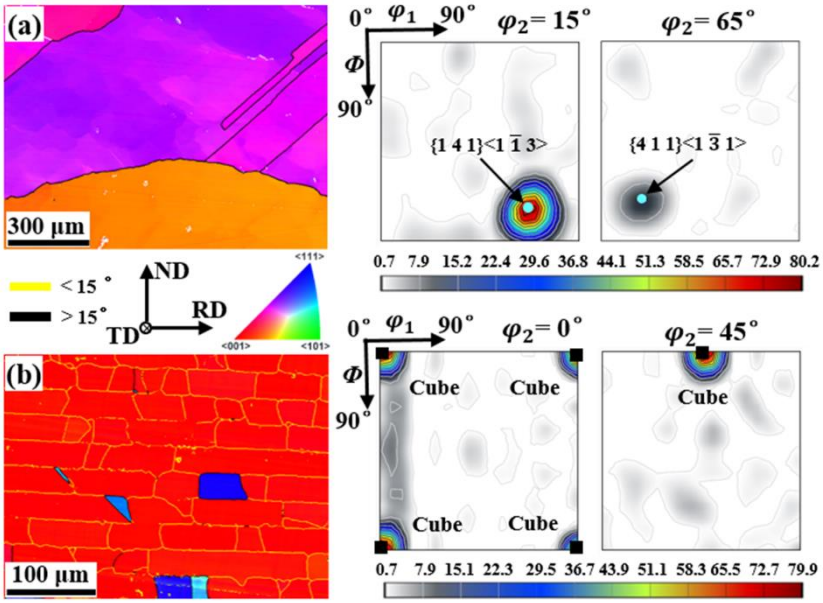

Fig. 6-2 EBSD RD-IPF micrographs and representative ODF φ2 sections from neutron diffraction of as-fully-sintered (a) pure Cu (φ2= 15° and 65°) and (b) Cu/GNS composite (φ2= 0° and 45°).

6.3.3 Microstructure and orientation evolution of pure Cu and Cu/GNS during heating

To investigate the microstructure and texture evolution features of the Cu/GNS composite samples with respect to the pure Cu samples during the sintering process, the as-cold-rolled Cu and Cu/GNS samples were heated to 5 different temperatures (150 ℃, 170 ℃, 230 ℃, 450 ℃ and 700 ℃) and then quenched in compressed argon flow to preserve the as-heated microstructure and texture. **Fig. 6-3** shows the EBSD Kernel Average Misorientation (KAM) micrographs of single-foil Cu of the pure Cu and Cu/GNS samples heated to 150℃ and 170℃ (**Fig. 6-3b** and **Fig. 6-3c**), respectively, and the EBSD texture component micrographs of the single-foil Cu of the pure Cu and Cu/GNS samples heated to 230°C, 450°C and 700°C (**Fig. 6-3d, e** and **f**), respectively. For reference, the KAM micrograph of the initial cold-rolled Cu is also displayed (**Fig. 6-3a**). It is seen from **Fig. 6-3b** that with the increase of the heating temperature from 150°C to 170°C the microstructures are still in band form, however, at 150°C in both the pure Cu and the Cu/GNS sample, the density of the disorientation that represents the density of Geometrical Necessary Dislocations (GNDs) decreased in certain regions in the bands, as indicated with the white arrows in the figures, indicating the occurrence of recovery or the early recrystallization nucleation. When the heating temperature was increased to 170°C, small equiaxed and distortion-free grains started to appear in the two samples, as indicated with the yellow arrows in the micrographs, indicating the onset of recrystallization. When the samples were further heated to 230°C, recrystallization continued. In the Cu/GNS sample, the initially banded microstructure was totally replaced by recrystallized grains, whereas in the pure Cu sample, the recrystallization was still in progress with the microstructure composed of recrystallized grains and deformed bands. The orientations of the recrystallized grains in the two cases are close to those of the cold-rolled texture components, as evidenced by the consistent colors of the texture components in **Fig. 6-3d**. The Cube oriented grains did not show any preference in growth. When the heating temperature was elevated to 450°C, abnormal grain growth occurred in the Cu/GNS sample (**Fig. 6-3e$_2$**). The Cube grains demonstrate strong growth preference. However, in the pure Cu sample, the recrystallization fully terminated and some recrystallized grains started to grow. Compared with the Cu/GNS sample, the grain

growth did not occur preferentially to the Cube oriented grains. When the samples were further heated to 700°C, although abnormal grain growth occurred in the two samples, almost all the Cu/GNS sample is occupied by the Cube grains, whereas the pure Cu sample is mainly occupied by the Goss oriented grains in the observed area. These results infer that the GNSs deposited on the cold-rolled Cu foils indeed promoted the growth of the Cube oriented grains.

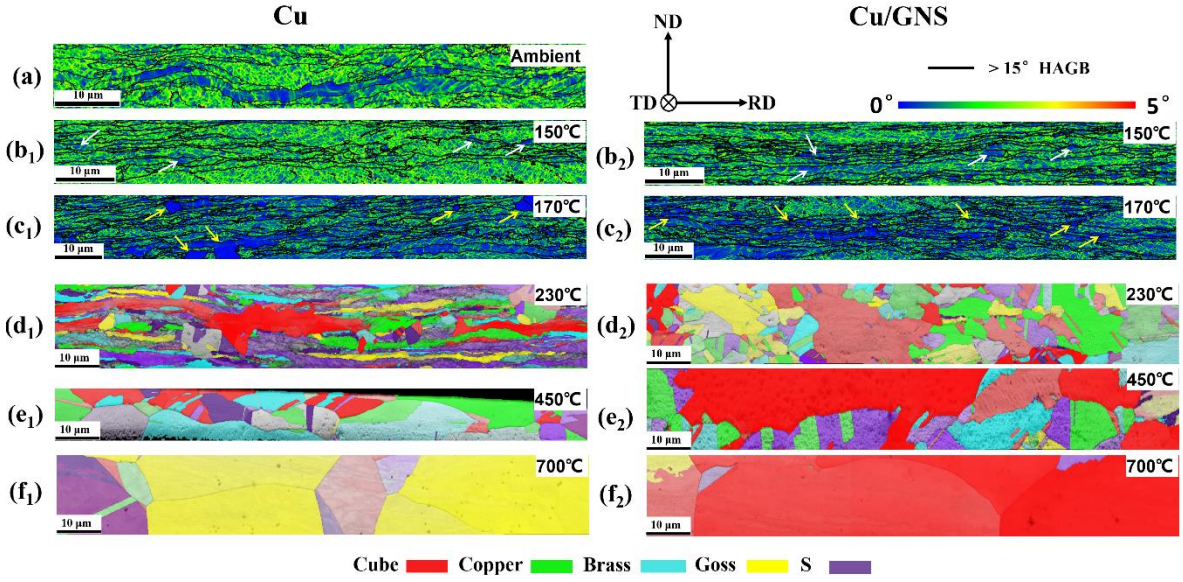

Fig. 6-3 Kernel Average Misorientation (KAM) micrographs of (a) Cu cold-rolled at ambient temperature and of Cu in pure Cu and Cu/GNS samples heated to (b) 150 ℃ and (c) 170 ℃, respectively. EBSD texture component micrographs of Cu in pure Cu and Cu/GNS heated to (d) 230 ℃, (e) 450 ℃ and (f) 700 ℃, respectively.

The texture evolution during the recrystallization and grain growth processes was also quantitatively examined in a large sample volume by neutron diffraction. **Fig. 6-4** shows the ODF sections of the pure Cu and the Cu/GNS composite sample heated to different temperatures (150 ℃, 170 ℃, 230 ℃ and 450 ℃) calculated from the neutron diffraction results measured from the whole sample volume. It is seen from **Fig. 6-4a$_1$**, **a$_2$**, **b$_1$** and **b$_2$** that both the pure Cu and the Cu/GNS samples still possess similar texture components but with different intensities with respect to those of the cold-rolled Cu. The spread of the Brass component along the α skeleton line toward the Goss orientation in the cold-rolled microstructure disappeared and the Cube component became strengthened, especially in the Cu/GNS sample. When the

heating temperature was increased to 230 ℃, the texture evolutions in the two samples were quite different. In the Cu/GNS sample, the non-Cube orientations greatly weakened, whereas the Cube orientation strengthened. However, in the pure Cu sample, the Cube component slightly weakened, whereas the Copper component strengthened. When the heating temperature increased to 450°C, in the Cu/GNS sample, the Cube component continued to develop and the other orientations largely disappeared, whereas, in the pure Cu sample, the existing orientations all continued to decrease their intensities. These results indicate that the GNSs indeed provided a unique driving force for the growth of the Cube grains during the grain growth process.

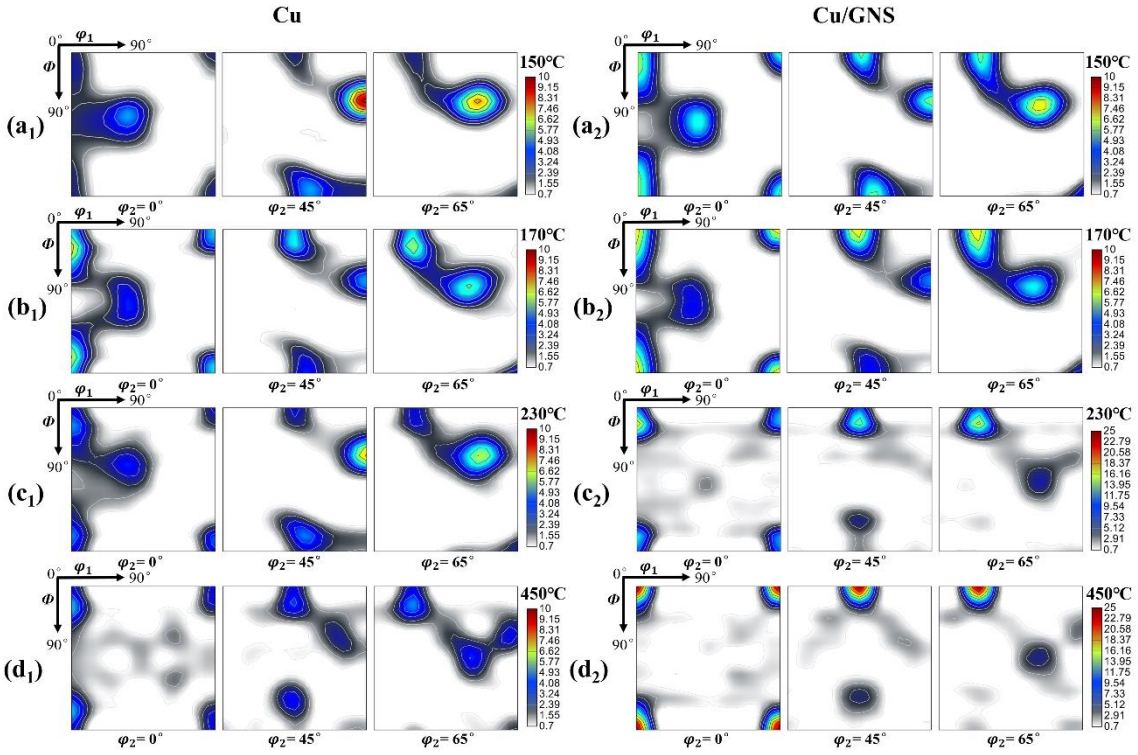

Fig. 6-4 Neutron diffraction ODF φ2= 0°; 45°; 65° sections of pure Cu samples heated to (a1) 150°C; (b1) 170°C; (c1) 230°C; (d1) 450°C and of Cu/GNS samples heated to (a2) 150°C; (b2) 170°C; (c2) 230°C; (d2) 450°C.

6.3.4 Thermal expansion of Cu and Cu/GNS during heating and relative lattice strains induced by GNS

As the promotion of the GNSs to the Cube grain growth occurred during the heating process, the incompatible thermal expansion behavior between the two materials should result

in thermal constraints to the softer Cu. This may lie behind the abnormal grain growth. Thus, in order to clarify the constraints, the evolution of the lattice strains of the Cu in the two kinds of samples during the heating process was investigated by the 4D *in-situ* synchrotron radiation technique (3D space + 1D time). **Fig. 6-5** displays the Debye-Scherrer pattern of the initial cold-rolled Cu sample and the integrated 1D Cu diffraction patterns from the pure Cu and the Cu/GNS composite sample in the 2θ range from 3° to 5.5° measured during heating, where the $\{111\}_{Cu}$, the $\{200\}_{Cu}$ and the $\{220\}_{Cu}$ reflection peaks were detected. It is seen from the two integrated peak figures that with the increase of the temperature all the detected peaks shifted toward the lower 2θ angle side, as indicated by the black arrows in the figures. According to the Bragg's law, such a shift of 2θ corresponds to the increase of the interplanar spacing (d-spacing) of these planes with the temperature. Thus, thermal expansion of Cu occurred during the heating process.

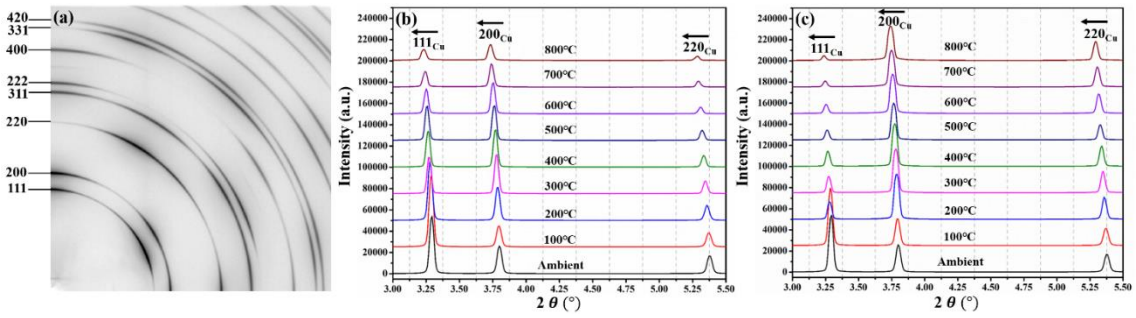

Fig. 6-5. HEXRD patterns for (a) the initial cold-rolled Cu sample obtained using a 2D detector and as-integrated 1D diffraction patterns of (b) pure Cu and (c) Cu/GNS at temperatures from ambient to 800°C. The intensity profile of each pattern was obtained by integrating the intensity of corresponding 2D Debye-Scherrer rings in the full azimuth angle range.

To analyze the characteristic lattice strain states of the Cu foils in the Cu/GNS sample with respect to those of the pure Cu, the in-plane (parallel to the foil plane) and out-of-plane (perpendicular to the foil plane) thermal expansion characteristics were further analyzed for the two kinds of samples. Under the geometrical arrangement of the synchrotron radiation diffraction measurements (**Fig. 2-3**), the samples were fixed during the whole heating process, and the incident beam was set to be parallel to the TD of each Cu foil in the pure Cu and

Cu/GNS samples. Thus, the change of the d-spacing of the lattice planes perpendicular to the RD was used to analyze the in-plane strain, and the change of the d-spacing of the lattice planes perpendicular to the ND the out-of-plane strain. **Fig. 6-6a** and **b** shows the RD and ND d_{hkl} of the $\{111\}_{Cu}$ and $\{200\}_{Cu}$ planes of the Cu foils in the pure Cu and in the Cu/GNS samples. It is seen that, in general, the d_{hkl} of each lattice plane increases linearly with the temperature. The difference in d_{hkl} between the RD and ND is due to the 2D feature of the thin Cu foils.

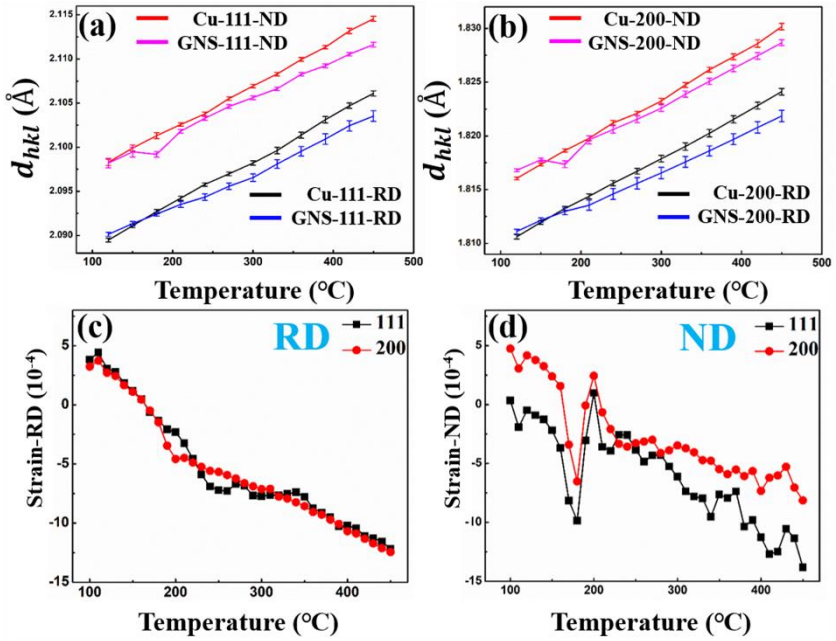

Fig. 6-6. Comparison of dhkl of (a) {111}Cu, (b) {200}Cu of the two samples and relative lattice strains of Cu in Cu/GNS with respect to that of Cu in pure Cu (c) in RD (in-plane) and (d) in ND (out-of-plane).

However, when we compare the slopes of the d_{hkl} curves of the Cu/GNS sample with those of the pure Cu sample in the same direction, we can find that with the increase of the temperature, $d_{hkl_{Cu}(T)}$ increases more rapidly than $d_{hkl_{GNS/Cu}(T)}$, especially at higher temperatures. This indicates that the deposited GNSs on the surfaces of the Cu foils indeed imposed constraints to the thermal expansion of the Cu foils. To figure out the constraints from the GNSs, we calculated the relative lattice strain (Type I, macro strain [80], giving rise to a shift of the diffraction peaks) of the Cu in the Cu/GNS sample with respect to that of the Cu in the pure Cu sample in the consistent direction at each temperature as expressed by Eq. (1):

$$\varepsilon = \frac{d_{hkl_{GNS/Cu}(T)} - d_{hkl_{Cu}(T)}}{d_{hkl_{Cu}(T)}}, \quad (6.1)$$

where $d_{hkl_{GNS/Cu}(T)}$ and $d_{hkl_{Cu}(T)}$ are the d_{hkl} of Cu in the Cu/GNS and in the pure Cu sample at temperature T. The results are displayed in **Fig. 6-6c** and **d**. It is seen from **Fig. 6-6c** that the GNSs induced a compressive strain in the plane parallel to the Cu foil plane (in-plane strain). This in-plane strain possesses bi-axial character, as the Cu layers in the sample are in thin foil shape, especially when the recrystallization was complete and the banded microstructure was replaced by the equiaxed recrystallized grains. Interestingly, the $\{200\}_{Cu}$ and $\{111\}_{Cu}$ strains were consistent during the whole heating process, inferring that the Cu foils possess an isostrain feature. Similarly, in the ND (**Fig. 6-6d**), the GNSs also introduced a compressive strain in the direction normal to the foil plane (out-of-plane strain). Although the value of the $\{111\}_{Cu}$ strain is not exactly the same as that of the $\{200\}_{Cu}$ strain at each temperature, the magnitudes of the two strains are very close. In the two cases, the absolute values of the strains increased linearly with the temperature, demonstrating an elastic condition.

Further examination of the diffraction patterns revealed that different levels of peak broadening occurred to the $\{200\}_{Cu}$ peaks in the two kinds of samples. Because a wide diffraction peak corresponds to a spread of d-spacing of the reflective lattice plane, the broadening of the peak infers a large variation of the lattice strain (Type II and III [80], mesoscopic and micro strain, manifested as a broadening of the diffraction peaks by synchrotron measurement), from a negative strain to a positive strain, if the peak is symmetric, which is the case in the present study. Thus, the Full Width at Half Maximum (FWHM) [81, 82] of the representive $\{200\}_{Cu}$ peaks of the pure Cu and the Cu/GNS in the respective RD and ND was extracted and displayed in **Fig. 6-7a** and **b**, respectively. As the FWHM are very sensitive to crystal defects, especially dislocations (the Type III strain [80]) that possess both lattice tension and compression around the dislocation lines, the progressive decrease and then a rapid decrease of the FWHM values below 210°C for the pure Cu sample and below 170°C for the Cu/GNS sample are related to the progressive and then rapid annihilation of dislocations during the recovery and recrystallization processes. After these temperatures, the FWHM

values of the two kinds of samples stay relatively constant (**Fig. 6-7a** and **b**). However, the RD-FWHM of the Cu/GNS sample behaves very abnormally, as shown in **Fig. 6-7b**. Instead of decrease, a drastic increase appeared although recrystallization had already completed and the dislocations had been largely eliminated (corresponding to the disappearance of the Type III strain [80]). Such a high level RD-FWHM infers that the compressive biaxial strain in the Cu foil plane is not constant everywhere. With respect to the average strain (corresponding to the diffraction peak), some parts of the foil were compressed and the other parts tensed. This result infers that the GNSs indeed imposed complicated constraints to the Cu foil (This strain corresponds to the Type II strain [80]). The multiple strain states of Cu will be analyzed in detail in the next part.

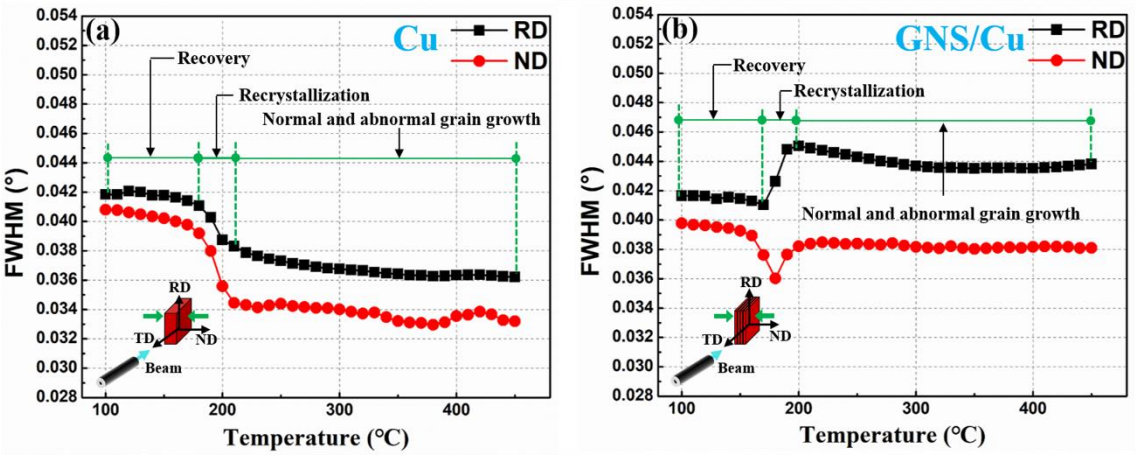

Fig. 6-7. FWHM of {200}Cu peaks for (a) pure Cu and (b) Cu/GNS in RD and ND on heating.

6.4 Discussion

6.4.1 Incompatible thermal expansion induced elastic strain states in Cu foil

The above results demonstrated that the GNSs deposited on the Cu surfaces imposed obvious constraints to the Cu foils during the heating process that significantly affected the growth of the recrystallized grains and modified the texture of the Cu foils. As the constraints occurred during the heating process and thermal expansion of the two materials is inevitable, the different thermal expansion behavior of the two should be at the origin. **Fig. 6-8** displays the TECs of Cu, graphite and graphene. The difference between graphite and graphene lies in the number of the two-dimensional hexagonally structured carbon layers. For the multi-layered

graphene (<15 layers) used in the present study, the expansion behavior shows different in-plane and out-of-plane features. The in-plane expansion behavior should be between that of graphene and graphite (> 10 layers [83]), *i.e.*, with negative TEC values (**Fig. 6-8**), and the out-of-plane behavior should be close to that of graphite, *i.e.*, with large positive TEC values even higher than those of Cu. For Cu, the expansion is isotropic with large positive TEC values. Thus, at elevated temperatures, the Cu of the Cu/GNS composite tended to expand in the planes parallel to the foil plane (in-plane), whereas the GNSs adhered on the Cu tended to shrink. The negative thermal expansion of the GNSs exerted a biaxial in-plain compressive constraint to the expansion of the Cu foil. However, in the out-of-plain direction, both the GNSs and the Cu foils expanded during heating. It should be noted that the samples were fixed by a holding frame in this direction during the heating process. Thus, with higher hardness and larger TEC, the GNSs exerted a uniaxial compressive constraint to the Cu foils in the direction perpendicular to the foil plane. Finally, a biaxial strain parallel to the Cu foil plane and a uniaxial compressive strain perpendicular to the Cu foil plane were produced in the Cu foils by the deposited GNSs on the Cu foil surfaces.

As the GNSs used in the present composite are very thin (1 ~ 5nm in thickness) with respect to the Cu foils (30 μm thickness), the biaxial constraint should be mainly situated in the surface layers of each Cu foil. With the increase of the depth to the central layer, this constraint decreases and the uniaxial compressive constraint in the foil normal direction (ND) becomes dominant. This means that the central layer experienced a tension in the foil plane from the uniaxial compression other than the compression from the in-plane shrinkage of the GNSs. Thus, the strain in RD changed from a compression in the surface layer to a tension in the central layer and resulted in a large variation of d_{hkl} and in turn the increased RD-FWHM (**Fig. 6-7b**). Thus, during the heating process, each Cu foil was in a composite strain state, i.e., the two surface layers were in biaxial compressive isostrain state in the foil plane and the central layer was in the uniaxial compression state in the direction normal to the foil plane. Clearly, it should be this complicated strain state that sustained the growth of the Cube grains in the Cu/GNS composite. The reason for this is certainly related to the interplay between the strain

state and the crystal orientation related elastic feature of Cu. Thus, the orientation-resolved elastic strain energy as the result of the interplay was further investigated.

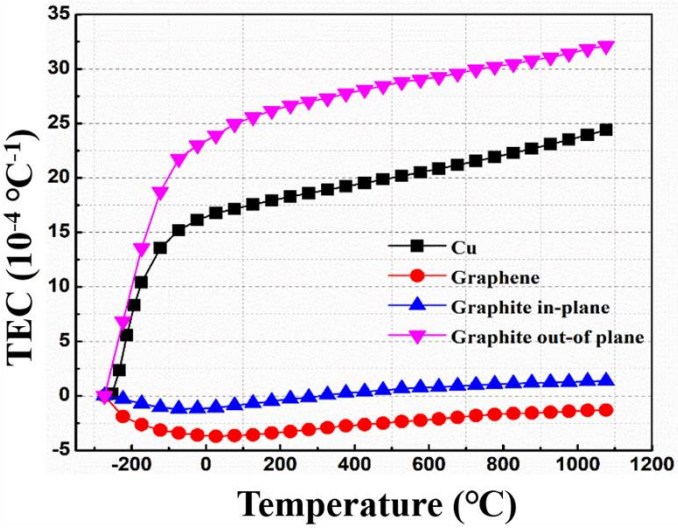

Fig. 6-8. Variations of thermal expansion coefficients (TECs) of Cu [84] and graphene [85] with temperature, and variations of in-plane and out-of-plane TECs of graphite [85] with temperature.

6.4.2 Orientation dependent elastic strain energy density of strained crystals

With the above analyzed strain state of the Cu foils, the stress state can be further derived and the elastic strain energy density can be calculated. In the theory of elasticity, if a crystal is elastically strained, the stress tensor σ_{ij} is related to the strain tensor ε_{kl} through the stiffness constant tensor C_{ijkl}, as expressed in the following equation in Nye's notation [86]:

$$\sigma_{ij} = C_{ijkl} \cdot \varepsilon_{kl}, \tag{6.2}$$

where the subscripts *i, j, k* and *l* take the integer values 1, 2 and 3. The matrix expression of Eq. (6.2) is given as Eq. (6.3). Due to the cubic crystal symmetry of Cu, the independent elastic constants of Cu in the crystal coordinate system are C_{11}, C_{12} and C_{44} with the corresponding values of 169, 122 and 75.3 GPa [19, 42], respectively. Eq. (6.3) for cubic crystals is given below.

Matrix expression of stiffness constant tensor C_{ijkl} in Nye's notation [86]:

$$\begin{bmatrix}\sigma_{11}\\ \sigma_{22}\\ \sigma_{33}\\ \sigma_{23}\\ \sigma_{13}\\ \sigma_{12}\end{bmatrix}=\begin{bmatrix}C_{1111} & C_{1122} & C_{1133} & C_{1123} & C_{1113} & C_{1112}\\ C_{2211} & C_{2222} & C_{2233} & C_{2223} & C_{2213} & C_{2212}\\ C_{3311} & C_{3322} & C_{3333} & C_{3323} & C_{3313} & C_{3312}\\ C_{2311} & C_{2322} & C_{2333} & C_{2323} & C_{2313} & C_{2312}\\ C_{1311} & C_{1322} & C_{1333} & C_{1323} & C_{1313} & C_{1312}\\ C_{1211} & C_{1222} & C_{1233} & C_{1223} & C_{1213} & C_{1212}\end{bmatrix}\cdot\begin{bmatrix}\varepsilon_{11}\\ \varepsilon_{22}\\ \varepsilon_{33}\\ \varepsilon_{23}\\ \varepsilon_{13}\\ \varepsilon_{12}\end{bmatrix} \tag{6.3}$$

For cubic crystals, Eq. (6.3) is in the following form:

$$\begin{bmatrix}\sigma_{11}\\ \sigma_{22}\\ \sigma_{33}\\ \sigma_{23}\\ \sigma_{13}\\ \sigma_{12}\end{bmatrix}=\begin{bmatrix}C_{11} & C_{12} & C_{12} & 0 & 0 & 0\\ C_{12} & C_{11} & C_{12} & 0 & 0 & 0\\ C_{12} & C_{12} & C_{11} & 0 & 0 & 0\\ 0 & 0 & 0 & C_{44} & 0 & 0\\ 0 & 0 & 0 & 0 & C_{44} & 0\\ 0 & 0 & 0 & 0 & 0 & C_{44}\end{bmatrix}\cdot\begin{bmatrix}\varepsilon_{11}\\ \varepsilon_{22}\\ \varepsilon_{33}\\ \varepsilon_{23}\\ \varepsilon_{13}\\ \varepsilon_{12}\end{bmatrix} \tag{6.4}$$

As the elastic strains were determined in the sample coordinate system (RD-TD-ND), the stress and strain are further related by

$$\sigma'_{ij} = C'_{ijkl} \cdot \varepsilon'_{kl} \tag{6.5}$$

in the sample coordinate system, where $C'_{ijkl}=A_{im}A_{jn}A_{ko}A_{lp}C_{mnop}$ (*i, j, k, l, m, n, o* and *p* all take integral values from 1 to 3) and A_{rt} (*r* = *i, j, k, l* and *t* = *m, n, o, p*) are direction cosine of the basis vectors of the crystal coordinate system with respect to the basis vectors of the sample coordinate system. Thus, the elastic strain energy density can be calculated as follows:

$$W = \frac{1}{2}\sigma'_{ij}\cdot\varepsilon'_{ij}. \tag{6.6}$$

6.4.2.1 Biaxial strain condition

In the present sample coordinate system, axes 1 and 2 stand for the respective RD and TD that define the plane parallel to the Cu foil plane and axis 3 stands for the ND normal to the foil plane. For the biaxial strain condition, the strain in the planes parallel to the foil plane is

$$\varepsilon'_{11} = \varepsilon'_{22} = \varepsilon'. \tag{6.7}$$

The stress components that are not in the plane of the Cu foil can be considered to be zero, i.e.,

$$\sigma'_{23} = \sigma'_{13} = \sigma'_{33} = 0. \tag{6.8}$$

As the GNSs were firmly embedded in the Cu foils,

$$\sigma'_{12} = 0. \tag{6.9}$$

Under these boundary conditions and with the cubic symmetry of Cu, the following equations can be obtained:

$$\begin{aligned} \sigma'_{11} &= C'_{1111}\varepsilon'_{11} + C'_{1122}\varepsilon'_{22} + C'_{1133}\varepsilon'_{33} \\ \sigma'_{22} &= C'_{2211}\varepsilon'_{11} + C'_{2222}\varepsilon'_{22} + C'_{2233}\varepsilon'_{33} \\ \sigma'_{12} &= C'_{1211}\varepsilon'_{11} + C'_{1222}\varepsilon'_{22} + C'_{1233}\varepsilon'_{33}. \end{aligned} \tag{6.10}$$

Thus, the biaxial moduli of plane (*h k l*) in the two in-plane directions (1 or RD and 2 or TD) is given by:

$$M_1 = \frac{\sigma'_{11}}{\varepsilon} = C'_{1111} + C'_{1122} - \frac{1}{C'_{3333}}\left(C'^{2}_{1133} + C'_{1133}C'_{2233}\right) \tag{6.11}$$

$$M_2 = \frac{\sigma'_{22}}{\varepsilon} = C'_{2211} + C'_{2222} - \frac{1}{C'_{3333}}\left(C'^{2}_{2233} + C'_{1133}C'_{2233}\right).$$

Hence, the linear mean value of the biaxial modulus for a plane *(h k l)* subjected to biaxial strain, $\bar{M}_{hkl}$, is:

$$\bar{M}_{hkl} = \frac{1}{2}(M_1 + M_2). \tag{6.12}$$

It should be noted that an equivalent way to obtain the coordinate transformation A_{rt} between the orthonormal sample coordinate system and the orthonormal crystal coordinate system can be made by representing the relation between the two coordinate systems with a set of triple rotations, i.e., Euler angles (φ_1, Φ, φ_2), in Bunge notation [45, 46], and expressing it in the rotation matrix, as follows

$$A_{rt} = R(\varphi_1)\ R(\Phi)\ R(\varphi_2) = \begin{bmatrix} u_1 & v_1 & w_1 \\ u_2 & v_2 & w_2 \\ h & k & l \end{bmatrix}. \tag{6.13}$$

In such a matrix, all the row elements are related to the foil plane. The (*h k l*) represents the crystalline plane parallel to the foil plane or normal to axis 3 (the ND), the $[u_1\ \ v_1\ \ w_1]$ and $[u_2\ \ v_2\ \ w_2]$ are two orthogonal in-plane unit vectors parallel to the respective axis 1 and axis 2, i.e., the RD and the TD. Once the matrix is constructed, the crystalline plane that is parallel

to the foil plane and the directions parallel to the RD and the TD are known. Thus, in the biaxial strain condition, the elastic strain energy density can be calculated with the following equation:

$$W = \frac{1}{2}\bar{M}_{hkl}\cdot{\varepsilon'}_{(hkl)}^{2}. \tag{6.14}$$

6.4.2.2 Uniaxial compression condition

Under this condition, the crystal is only subjected to a uniaxial stress in axis 3 (the ND), i.e., ${\sigma'}_{33}$ and all other normal stress components and all shear stress components are equal to zero, i.e.,

$${\sigma'}_{11} = {\sigma'}_{22} = {\sigma'}_{23} = {\sigma'}_{13} = {\sigma'}_{12} = 0. \tag{6.15}$$

Utilizing Eq. (6.15) as boundary conditions and with cubic crystal symmetry, the following stress and strain relations can be obtained:

$$\begin{aligned} {\sigma'}_{11} &= 0 = {C'}_{1111}{\varepsilon'}_{11}+{C'}_{1122}{\varepsilon'}_{22}+{C'}_{1133}{\varepsilon'}_{33} \\ {\sigma'}_{22} &= 0 = {C'}_{2211}{\varepsilon'}_{11}+{C'}_{2222}{\varepsilon'}_{22}+{C'}_{2233}{\varepsilon'}_{33} \\ {\sigma'}_{33} &= {C'}_{3311}{\varepsilon'}_{11}+{C'}_{3322}{\varepsilon'}_{22}+{C'}_{3333}{\varepsilon'}_{33}\ . \end{aligned} \tag{6.16}$$

Thus, the elastic modulus in the compressive stress direction can be deduced and is as follows:

$$E'_{33} = \frac{{\sigma'}_{33}}{{\varepsilon'}_{33}} = ({C'}_{1111}{C'}_{2233}^{2}+{C'}_{2222}{C'}_{1133}^{2}-2{C'}_{1122}{C'}_{1133}{C'}_{2233})/({C'}_{1122}^{2}-{C'}_{1111}{C'}_{2222})+{C'}_{3333}. \tag{6.17}$$

Then, the strain energy density associated with the uniaxial compression is:

$$W = \frac{1}{2}E'_{33}\cdot{\varepsilon'}_{33}^{2} \tag{6.18}$$

6.4.2.3 Simulated elastic modulus for the two strain conditions

The above analyses show that both the biaxial elastic strain energy and the uniaxial compressive elastic strain energy are crystal orientation related. The former is proportional to the biaxial modulus $\bar{M}_{hkl}$ and the latter to the Young's modulus in the direction normal to the foil plane or the (h k l) plane, E'_{33}. For the grains in the surface layers of the Cu foils in the Cu/GNS sample, they demonstrated a biaxial isostrain feature (**Fig. 6-6c**), meaning that for differently oriented grain the elastic strains induced by the GNSs are the same. Thus, the strain

energy is solely determined by $\bar{M}_{hkl}$. As Cu is elastically anisotropic, if differently oriented grains were subjected to the same biaxial strain, the strain energies of the grains should be very different. Thus, we simulated the $\bar{M}_{hkl}$ of all possibly oriented Cu crystals and the orientation-resolved $\bar{M}_{hkl}$ represented in the orientation space is displayed in **Fig. 6-9**. It is seen that the $\bar{M}_{hkl}$ is indeed very anisotropic, varying from 114.18 GPa to 261.26 GPa. The lowest $\bar{M}_{hkl}$ (114.86 GPa) is associated with the grains having their $\{002\}_{Cu}$ parallel to the foil plane and the highest $\bar{M}_{hkl}$ (261.26 GPa) with those possessing their $\{111\}_{Cu}$ parallel to the foil plane. Thus, in the biaxial isostrain state, the grains with the $\{002\}_{Cu}$ parallel to the foil plane possess the lowest elastic strain energy and are energetically advantageous to grow. Consequently, during the heating process when grain growth occurred, the growth of the Cube oriented grains was stimulated, as their growth can effectively minimize the elastic strain energy and hence the total energy of the system.

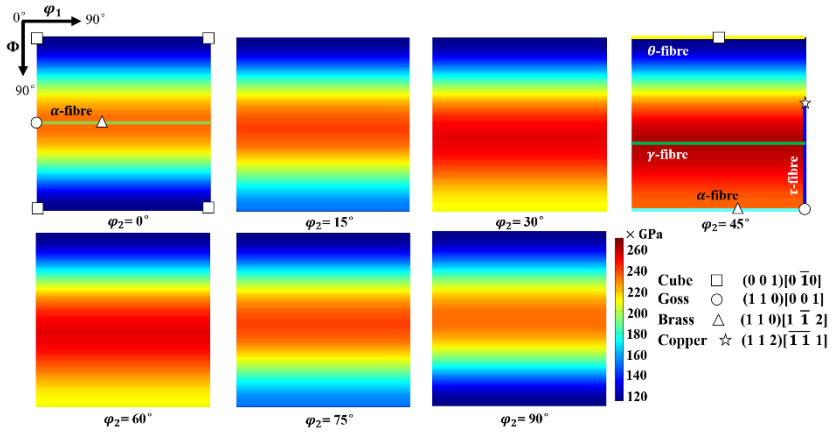

Fig. 6-9. φ_2=0° to 90° sections of mean biaxial modulus $\bar{M}_{hkl}$ as a function of crystal orientation in orientation space.

For the grains in the central layers of the Cu foils, they mainly experienced a uniaxial compressive strain. Although the strains in differently oriented grains are slightly different, they are very close (**Fig. 6-6d**). Thus, the strain energy should also be dominated by the Young's modulus in the compression direction, i.e., E'_{33}. We also calculated the E'_{33} of all possibly oriented Cu grains and the obtained orientation-resolved E'_{33} represented in the orientation space is displayed in **Fig. 6-10**. It is seen that the E'_{33} is also very anisotropic, varying from 66.70 GPa to 191.27 GPa. The lowest E'_{33} (66.70 GPa) is associated with the grains with their

<002>$_{Cu}$ parallel to the foil plane normal direction and the highest E'_{33} (191.27 GPa) is associated to those with their <111>$_{Cu}$ parallel to the foil plane normal direction. Thus, in the uniaxial compression (quasi-isostrain) condition, again the grains with the <002>$_{Cu}$ parallel to the foil plane normal direction or grains with the $\{002\}_{Cu}$ parallel to the foil plane possess the lowest elastic strain energy and are energetically advantageous to grow. As a result, during the heating process, the growth of the Cube oriented grains was stimulated, as their growth can minimize the elastic strain energy and hence the total energy of the system. These analysis results indeed indicate that the complicated strain state induced by the GNSs provided the unique driving force for the abnormal grain growth of the Cube oriented grains in the Cu/GNS composite.

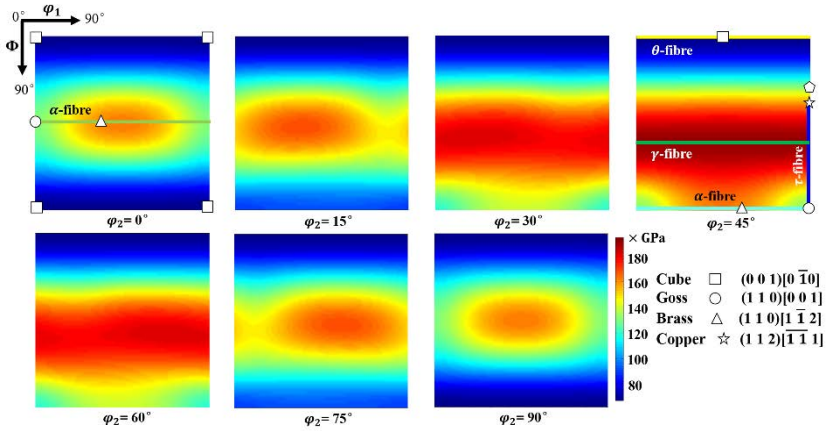

Fig. 6-10. φ_2=0° to 90° sections of Young's modulus in the uniaxial compression direction E'_{33} as a function of crystal orientation in orientation space.

6.5 Summary

In the present chapter, the complicated elastic strain state of the Cu matrix induced by the thermal constraints from the GNS reinforcements in the Cu/GNS metal/non-metal composite was experimentally investigated through *ex-situ* and *in-situ* characterization of microstructure, orientation and lattice strain by means of SEM-EBSD in mesoscale, and neutron diffraction and synchrotron radiation in macroscopic scale. Its selective simulating effect on the specifically oriented grains was quantitatively analyzed by integrated theories of crystallography and elasticity. Its orientation-related potential on orientation selectivity was mapped in the orientation space.

The results revealed that during the heating process of the sintering, the anisotropic and incompatible expansion of the GNS imposed multiple elastic constraints to the Cu foils. In the surface layers, the Cu foils mainly experienced a biaxial compressive isostrain parallel to the foil plane, and, in the central layer, they were subjected a uniaxial compressive strain perpendicular to the foil plane. The anisotropic elasticity of Cu favored the further growth of the Cube oriented grains. The growth of such grains allowed the smallest biaxial modulus planes ($\{200\}_{Cu}$ plane) to be situated in the biaxial isostrain planes and the smallest Young's modulus direction ($<200>_{Cu}$ direction) to be in the uniaxial compression direction, hence minimizing the total strain energy.

The mechanism of elastic strain induced grain growth of selected orientations revealed in the present work provides new information on recrystallization and grain growth of metallic materials and useful for analyzing abnormal grain growth in elastically strained materials, such as the cases in additive fabrication. The orientation related grain growth stimulus can be applied to fabrication process to realize texturization or even monocrystallization of metallic materials.

Chapter 7 Conclusion and Perspectives

7.1 Conclusions

In the present work, the fabrication method of the Cu/GNS laminated composites was studied and the synthesis parameters were optimized to fabricate the laminated Cu/GNS composite materials. The recrystallization features of cold-rolled Cu foils and fabricated Cu/GNS composites with two kinds of Cu foil thicknesses (10 μm and 30 μm) were investigated systematically by means of SEM-EBSD for microstructure evolution observation, neutron and synchrotron radiation diffraction for texture measurement and in-situ synchrotron radiation for lattice strain characterization during heating. The obtained data were analyzed in the frame of crystallography combined with crystal elasticity and surface energy. From the obtained results, the main conclusions can be drawn as follows:

(1) Fabrication of Cu/GNS composites and optimization of the fabrication parameters.

The deposition of the GNSs on the Cu surfaces was realized by electrophoretic deposition technique. The effects of ultrasonic vibration duration and deposition duration on the dispersion of clustered GNSs in the electrolyte and on the deposition quality of the GNSs on the Cu foil surfaces were investigated and the optimum parameters were worked out. With the optimized fabrication parameters, the GNSs were deposited uniformly on the Cu foil surfaces and the density of the GNSs on the Cu foil surface can be adjusted by varying the deposition duration. With the optimized process, as-deposited Cu foils were fabricated, then the qualified Cu/GNS composites were produced and employed as the subject materials for the recrystallization study of this work.

(2) Site and driving force for nucleation during the recrystallization process of cold-rolled Cu foils with Cu foil thickness of 10 μm.

At the nucleation state, the orientations of the nuclei were mainly inherited from the deformation texture components and clustered at two orientation locations. One is from the

Cube to the RD-rotated Cube and along the α skeleton line from the Goss to the Brass. The other is along the β fiber covering the Copper, the S and the φ_2-rotated Copper. The first cluster demonstrated size preference, especially the Cube orientation. At this state, the screening factor is the deformation stored energy. Those with low Taylor factors surrounded with high Taylor factor deformation matrices had the preference in nucleation and growth.

(3) Dominating factors for the primary grain growth right after the nucleation in 10 μm thick Cu foils.

When the recrystallized nuclei grew to certain sizes (through the foil thickness) during heating, the geometrical 2D features of the foils induced orientation dependent biaxial thermal constraint and imposed orientation dependent surface constraint to the grown grains. The nuclei with both moderate biaxial moduli in the foil plane and moderate surface energy densities were favored for further growth. Under such constraints, the RD-rotated Cube and the Brass orientations in the first cluster and the near Copper, the near S and the φ_2-rotated Copper orientations survived at the completion of the recrystallization.

(4) Dominating factors for the post-recrystallization grain growth in 10 μm thick Cu foils.

During the post-recrystallization grain growth, the twin relations between the RD-rotated Cube and the φ_2-rotated Copper grains produced coherent {111} interfaces when the two grew into contact. Such immobile boundaries stabilized the two orientations. The agglomerates of the two oriented blocks further benefited from the complementary anisotropic biaxial moduli. The relatively higher moduli of the φ_2-rotated Copper oriented crystals was compensated by the relatively lower moduli of the RD-rotated Cube oriented crystals. Such a combination allowed a preferential growth of the φ_2-rotated Copper crystals at the expense of the other surviving orientations that had no specific orientation relationships and were delineated by the random high-angle boundaries.

(5) Effect of GNS on the recrystallization texture evolution of Cu foils with thickness of 10 μm.

The effect of the GNSs on the recrystallization texture evolution of 10 μm thick Cu foils appeared at high temperatures. With the existence of the GNS layer, the growth of the Cu grains was confined within each Cu layer and the bulk Cu/GNS composites could be regarded as many individual Cu layers. Moreover, the adhered GNSs did not create much constrain on the expansion of adjacent Cu, only working as a barrier for the penetration of the grown Cu grains. As a result, the recrystallization texture of the bulk Cu/GNS composites possess the same features as those of the Cu foils at lower temperatures when they were not yet sintered into a bulk block. The texture of the bulk Cu/GNS composites are still dominated by the RD-rotated Cube and φ_2-rotated Copper components.

(6) Elastic strain induced abnormal grain growth in Cu/GNS composites with Cu layer thickness of 30 μm.

The results revealed that during the heating process of the sintering, the anisotropic and incompatible expansion of the GNS imposed multiple elastic constraints to the Cu foils. In the surface layers, the Cu foils mainly experienced a biaxial compressive isostrain parallel to the foil plane, and, in the central layer, they were subjected a uniaxial compressive strain perpendicular to the foil plane. The anisotropic elasticity of Cu favored the further growth of the Cube oriented grains. The growth of such grains allowed the smallest biaxial modulus planes ($\{200\}_{Cu}$ plane) to be situated in the biaxial isostrain planes and the smallest Young's modulus direction ($<200>_{Cu}$ direction) to be in the uniaxial compression direction, hence minimizing the total strain energy.

7.2 Perspectives

The present PhD work thoroughly investigated the recrystallization behavior of Cu and Cu/GNS composites with different Cu foil thicknesses. Various stages during sintering, such as nucleation, primary growth of nuclei, normal grain growth and abnormal grain growth were studied in the frame of crystallography. The driving force and dominating factors for each step were analyzed systematically. The revealed mechanism in this work could provide new

perspectives on further investigation of recrystallization of FCC materials that could be summarized as follows:

(1) As the grain growth in the Cu foils with thickness of 10 μm were controlled by surface energy, biaxial strain energy and grain boundary mobility, investigations on the recrystallization of Cu foils with different thicknesses should be conducted to find the threshold thickness for transition of the dominating factors.

(2) Since the annealing twins do not contribute to the obtained recrystallization texture, the formation mechanism and variant selection of the annealing twins can be further investigated.

(3) For the Cu/GNS composite with the Cu layer thickness of 30 μm, the addition of the GNS created a hybrid strain state in the Cu layers that resulted in the abnormal grain growth of the Cube oriented grains. The employed heating rate was 5 $℃ \cdot \mathrm{min}^{-1}$ making the recrystallization in our samples close to a static process. Different heating rates could be employed to investigate the kinetics of the recrystallization of Cu/GNS composites and the stimulating efficiency of the GNSs on abnormal grain growth.

Reference

[1] M. Mehdi, Y. He, E.J. Hilinski, L.A.I. Kestens, A. Edrisy, The evolution of cube ({001}<100>) texture in non-oriented electrical steel, Acta Mater. 185 (2020) 540-554.

[2] John Humphreys, Gregory S. Rohrer, A. Rollett, Recrystallization and Related Annealing Phenomena, Third ed., Elsevier (2017).

[3] F. Yang, C. Ma, J.Q. Jiang, H.P. Feng, S.Y. Zhai, Effect of cumulative strain on texture characteristics during wire drawing of eutectoid steels, Scr. Mater. 59(8) (2008) 850-853.

[4] S.-H. Kim, S.Z. Han, C.J. Kim, I.-Y. Hwang, F. Yin, Evolution of Rolling Textures of Cold Rolled Copper Foils, Mater. Trans. 50(3) (2009) 537-543.

[5] G.R. Canova, U.F. Kocks, J.J. Jonas, Theory of torsion texture development, Acta Metall. 32(2) (1984) 211-226.

[6] P. Sanchez, A. Pochettino, T. Chauveau, B. Bacroix, Torsion texture development of zirconium alloys, J. Nuclear. Mater. 298 (2001) 329-339.

[7] B.J. Duggan, M. Sindel, C.D. Kohlhoff, K. Lucke, Oriented nucleation, oriented growth and twinning in cube texture formation, Acta Metall. Mater. 38 (1990) 103-111.

[8] O. Engler, H.E. Vatne, E. Nes, The roles of oriented nucleation and oriented growth on recrystallization textures in commercial purity aluminium, Mater. Sci. Eng. A 205 (1996) 187-198.

[9] C.S. Barrett, Recrystallization texture of aluminium after compression, Trans. AIME 137 (1940) 128-145.

[10] G.H. Fan, Y.B. Zhang, J.H. Driver, D. Juul Jensen, Oriented growth during recrystallization revisited in three dimensions, Scr. Mater. 72-73 (2014) 9-12.

[11] D.A. Molodov, U. Czubayko, G. Gottstein, L.S. Shvindlerman, Mobility of <111> tilt grain boundaries in the vicinity of the special misorientation Σ=7 in bicrystals of pure aluminium, Scr. Metall. Mater. 32(4) (1995) 529-534.

[12] G. Gottstein, D.A. Molodov, L.S. Shvindlerman, D.J. Srolovitz, M. Winning, Grain boundary migration: misorientation dependence Curr. Opin. Solid State Mater. Sci. 5 (2001) 9-14.

[13] G. Gottstein, D.A. Molodov, U. Czubayko, L.S. Shvindlerman, High-Angle Grain Boundary Migration in Aluminium Bicrystals, Le Journal de Physique IV 05(C3) (1995) C3-89-C3-106.

[14] W.H. Hosford, Mechanical behavior of materials, New York, Cambridge University Press (2010).

[15] I. Samajdar, B. Verlinden, P.V. Houtte, D. Vanderschueren, γ-Fibre recrystallization texture in IF-steel: an investigation on the recrystallization mechanisms, Mater. Sci. Eng. A 238 (1997) 343-350.

[16] L. Kestens, J.J. Jonas, P.V. Houtte, E. Aernoudt, Orientation selective recrystalllization of nonoriented electrical steels, Metall. Trans. A 27A (1996) 2347-2358.

[17] M.H. Alvi, S.W. Cheong, J.P. Suni, H. Weiland, A.D. Rollett, Cube texture in hot-rolled aluminum alloy 1050 (AA1050)-nucleation and growth behavior, Acta Mater. 56(13) (2008) 3098-3108.

[18] A.A. Ridha, W.B. Hutchinson, Recrystallization mechanisms and the origin of cube texture in copper, Acta Metall. 30 (1982) 1929-1939.

[19] E.M. Zielinski, R.P. Vinci, J.C. Bravman, The influence of strain energy on abnormal grain growth in copper thin films, Appl. Phys. Lett. 67(8) (1995) 1078-1080.

[20] R. Carel, C.V. Thompson, H.J. Frost, Computer simulation of strain energy effects vs surface and interface energy effects on grain growth in thin films, Acta Mater. 44(6) (1996) 2479-2494.

[21] J.M. Zhang, K.W. Xu, V. Ji, Competition between surface and strain energy during grain growth in free-standing and attached Ag and Cu films on Si substrates, Appl. Surf. Sci. 187 (2002) 60-67.

[22] N.J. Park, D.P. Field, M.M. Nowell, P.R. Besser, Effect of film thickness on the evolution of annealing texture in sputtered copper films, J. Electron. Mater. 34(12) (2005) 1500-1508.

[23] L.A.I. Kestens, H. Pirgazi, Texture formation in metal alloys with cubic crystal structures, Mater. Sci. Technol. 32(13) (2016) 1303-1315.

[24] J. Hirsch, K. Lucke, Overview no. 76: Mechanism of deformation and development of rolling textures in polycrystalline f.c.c. metals-II. Simulation and interpretation of experiments on the basis of Taylor-type theories, Acta Metall. 36(11) (1988) 2883-2904.

[25] S.C. Hu, J.W. Huang, Z.y. Zhong, Z. Y.Y., Y. Cai, S.N. Luo, Texture evolution in nanocrystalline Cu under shock compression, J. Appl. Phys. 127 (2020) 215106.

[26] Q.Q. Shao, L.H. Liu, T.W. Fan, D.W. Yuan, J.H. Chen, Effects of solute concentration on the stacking fault energy in copper alloys at finite temperatures, J. Alloys Compd. 726 (2017) 601-607.

[27] P.A. Beck, H. Hu, The origin of recrystallization textures, Metals Park, OH: American Society for Metals, (1966).

[28] OLAF ENGLER, V. RANDLE, Introduction to Texture Analysis-Macrostructure, Microstructure and Orientation Mapping, Taylor & Francis (2010).

[29] M. Murakami, T. Yogi, Strain in evaporated Nb thin films, J. Appl. Phys. 57 (2) (1985) 211-215.

[30] P. Chekhonin, B. Beausir, J. Scharnweber, C.-G. Oertel, T. Hausöl, H.W. Höppel, H.-G. Brokmeier, W. Skrotzki, Confined recrystallization of high-purity aluminium during accumulative roll bonding of aluminium laminates, Acta Mater. 60(11) (2012) 4661-4671.

[31] P. Sonnweberribic, P. Gruber, G. Dehm, E. Arzt, Texture transition in Cu thin films: Electron backscatter diffraction vs. X-ray diffraction, Acta Mater. 54(15) (2006) 3863-3870.

[32] E.M. Zielinski, R.P. Vinci, J.C. Bravman, Effects of barrier layer and annealing on abnormal grain growth in copper thin films, J. Appl. Phys. 76(8) (1994) 4516-4523.

[33] C.V. Thompson, R. Carel, Texture development in polycrystalline thin films, Mater. Sci. Eng. B 32 (1995) 211-219.

[34] W. Mao, Formation of recrystallization cube texture in high purity face-centered cubic metal sheets, J. Mater. Eng. Performance 8(5) (1999) 556-560.

[35] B. Beausir, J.-J. Fundenberger, Analysis Tools for Electron and X-ray diffraction, ATEX - software (2017). http://www.atex-software. eu .

[36] C. Randau, U. Garbe, H.G. Brokmeier, StressTextureCalculator: a software tool to extract texture, strain and microstructure information from area-detector measurements, J. Appl.Crystallogr. 44(3) (2011) 641-646.

[37] N. Schell, A. King, F. Beckmann, T. Fischer, M. Müller, A. Schreyer, The High Energy Materials Science Beamline (HEMS) at PETRA III, Mater. Sci. Forum 772 (2013) 57-61.

[38] L. Lutterotti, Matthies, MAUD-materials analysis using diffraction. http:// maud.radiographema.com/.

[39] D. Chateigner, L. Lutterotti, M. Morales, Quantitative texture analysis and combined analysis, International Tables for Crystallography H(Chapter 5.3) (2019) 555-580.

[40] E.E. Villalobos-Portillo, D.C. Burciaga-Valencia, L. Fuentes-Montero, M.E. Montero-Cabrera, D. Chateigner, L.E. Fuentes-Cobas, Texture, 2D diffraction and piezoelectricity, Boletín de la Sociedad Española de Cerámica y Vidrio 59(5) (2020) 219-228.

[41] A.P. Hammersley, S.O. Svensson, M. Hanfland, A.N. Fitch, D. Hausermann, Two-dimensional detector software: From real detector to idealised image or two-theta scan, High Pressure Res. 14(4-6) (1996) 235-248.

[42] K.M. Knowles, The Biaxial Moduli of Cubic Materials Subjected to an Equi-biaxial Elastic Strain, J. Elast. 124(1) (2016) 1-25.

[43] R.J. Roe, Description of crystallite orientation in polycrystalline materials. III. General solution to pole figure inversion, J. Appl. Phys. 36 (1965) 2024.

[44] H.J. Bunge, Texture analysis in materials science, Akademie-Vertag, Berlin. (1969).

[45] H.J. Bunge, C. Esling, J. Muller, The role of the inversion centre in texture analysis, J. Appl. Crystallogr. 13 (1980) 544-554.

[46] H.J. Bunge, C. Esling, J. Muller, The influence of crystal and sample symmetries on the orientation distribution function of the crystallites in polycrystalline materials, Acta Cryst. A 37 (1981) 889-899.

[47] Y. Zhang, Z. Li, C. Esling, J. Muller, X. Zhao, L. Zuo, A general method to determine twinning elements, J Appl. Crystallogr 43(6) (2010) 1426-1430.

[48] R.D. Doherty, D.A. Hughes, F.J. Humphreys, J.J. Jonas, D.J. Jensen, M.E. Kassner, W.E. King, T.R. McNelley, H.J. McQueen, A.D. Rollet, Current issues in recrystallization: a review, Materials Science and Engineering A 238 (1997) 219-274.

[49] D.D. Sam, B.L. Adams, Orientation and strain dependence of stored energy of cold work in axisymmetric copper, Metall. Trans. A 17A (1986) 513-517.

[50] J. Hirsch, K. Lucke, The application of quantitative texture analysis for investigating continuous and discontinuous recrystallization processes of Al-0.01Fe, Acta Metall. 33(10) (1985) 1927-1938.

[51] D.G. Cram, X.Y. Fang, H.S. Zurob, Y.J.M. Bréchet, C.R. Hutchinson, The effect of solute on discontinuous dynamic recrystallization, Acta Mater. 60(18) (2012) 6390-6404.

[52] D.G. Cram, H.S. Zurob, Y.J.M. Brechet, C.R. Hutchinson, Modelling discontinuous dynamic recrystallization using a physically based model for nucleation, Acta Mater. 57(17) (2009) 5218-5228.

[53] P. Duval, F. Louchet, J. Weiss, M. Montagnat, On the role of long-range internal stresses on grain nucleation during dynamic discontinuous recrystallization, Mater. Sci. Eng. A 546 (2012) 207-211.

[54] H. Jazaeri, F.J. Humphreys, The transition from discontinuous to continuous recrystallization in some aluminium alloys, Acta Mater. 52(11) (2004) 3251-3262.

[55] A. Belyakov, T. Sakai, H. Miura, R. Kaibyshev, K. Tsuzaki, Continuous recrystallization in austenitic stainless steel after large strain deformation, Acta Mater. 50 (2002) 1547-1557.

[56] X.P. Chen, X.G. Li, S. Li, Q. Liu, Continuous recrystallization of commercial Al-1.2 wt%Mn alloy produced by thermomechanical processing, Mater. Lett. 180 (2016) 101-104.

[57] K.J.H. Al-Fadhalah, C.-M. Li, A.J. Beaudoin, D.A. Korzekwa, I.M. Robertson, Microplastic processes developed in pure Ag with mesoscale annealing twins, Acta Mater. 56(19) (2008) 5764-5774.

[58] Z.H. Cao, L.J. Xu, W. Sun, J. Shi, M.Z. Wei, G.J. Pan, X.B. Yang, J.W. Zhao, X.K. Meng, Size dependence and associated formation mechanism of multiple-fold annealing twins in nanocrystalline Cu, Acta Mater. 95 (2015) 312-323.

[59] I. Marković, S. Nestorović, B. Markoli, M. Premović, S. Mladenović, Study of anneal hardening in cold worked Cu-Au alloy, J. Alloys Compd. 658 (2016) 414-421.

[60] S. Mahajan, C.S. Pande, M.A. Iman, B.B. Rath, Formation of annealling twins in f.c.c. crystals, Acta Mater. 45(6) (1997) 2633-2638.

[61] R.L. Fullman, J.C. Fisher, Formation of annealing twins during grian growth, J. Appl. Phys. 22(11) (1951) 1350-1355.

[62] M.A. Meyers, L.E. Murr, A model for the formation of annealing twins in F.C.C. metals and alloys, Acta Metall. 26 (1978) 951-962.

[63] Z. Zhang, M.-p. Wang, Z. Li, N. Jiang, S. Hao, J. Gong, H. Hu, Twinning, dynamic recovery and recrystallization in the hot rolling process of twin-roll cast AZ31B alloy, J. Alloys Compd. 509(18) (2011) 5571-5580.

[64] J.M. Zhang, F. Ma, K.W. Xu, Calculation of the surface energy of fcc metals with modified embeded-atom method, Chin. Phys. 13(7) (2004) 1082-1090.

[65] J.J. Sidor, R.H. Petrov, L.A.I. Kestens, Modeling the crystallographic texture changes in aluminum alloys during recrystallization, Acta Mater. 59(14) (2011) 5735-5748.

[66] S.-H. Hong, D.N. Lee, The evolution of the cube recrystallization texture in cold rolled copper sheets, Mater. Sci. Eng. A 351(1-2) (2003) 133-147.

[67] B.J. Duggan, K. Lucke, G. Kohlhoff, C.S. Lee, On the origin of cube texture in copper, Acta Metall. Mater. 41(6) (1993) 1921-1927.

[68] A. Merlini, P.A. Beck, Study of the origin of the cube texture, Acta Metall. 1 (1953) 598-606.

[69] S. Xiang, X. Wang, M. Gupta, K. Wu, X. Hu, M. Zheng, Graphene nanoplatelets induced heterogeneous bimodal structural magnesium matrix composites with enhanced mechanical properties, Sci. Rep. 6 (2016) 38824.

[70] Z. Yang, L. Wang, Z. Shi, M. Wang, Y. Cui, B. Wei, S. Xu, Y. Zhu, W. Fei, Preparation mechanism of hierarchical layered structure of graphene/copper composite with ultrahigh tensile strength, Carbon 127 (2018) 329-339.

[71] C. Ferraro, S. Meille, J. Réthoré, N. Ni, J. Chevalier, E. Saiz, Strong and tough metal/ceramic micro-laminates, Acta Mater. 144 (2018) 202-215.

[72] B. Hwang, W. Kim, J. Kim, S. Lee, S. Lim, S. Kim, S.H. Oh, S. Ryu, S.M. Han, Role of Graphene in Reducing Fatigue Damage in Cu/Gr Nanolayered Composite, Nano Lett. 17(8) (2017) 4740-4745.

[73] X. Liu, D. Wei, L. Zhuang, C. Cai, Y. Zhao, Fabrication of high-strength graphene nanosheets/Cu composites by accumulative roll bonding, Mater. Sci. Eng. A 642 (2015) 1-6.

[74] A.G. Sheinerman, M.Y. Gutkin, Multiple cracking in deformed laminated metal-graphene composites, Comp. Struct. 191 (2018) 113-118.

[75] J. Sun, J. Zhao, Multi-layer graphene reinforced nano-laminated WC-Co composites, Mater. Sci. Eng. A 723 (2018) 1-7.

[76] H. Wu, G. Fan, M. Huang, L. Geng, X. Cui, H. Xie, Deformation behavior of brittle/ductile multilayered composites under interface constraint effect, Int. J. Plast. 89 (2017) 96-109.

[77] T. Han, J. Li, N. Zhao, C. He, Microstructure and properties of copper coated graphene nanoplates reinforced Al matrix composites developed by low temperature ball milling, Carbon 159 (2020) 311-323.

[78] S.L. Xiang, M. Gupta, X.J. Wang, L.D. Wang, X.S. Hu, K. Wu, Enhanced overall strength and ductility of magnesium matrix composites by low content of graphene nanoplatelets, Composites, Part A 100 (2017) 183-193.

[79] R.P. Vinci, E.M. Zielinski, J.C. Bravman, Thermal strain and stress in thin films, Thin Solid Films 262 (1995) 142-153.

[80] D. Chateigner, Combined Analysis, John wiley & Sons, London, UK, (2013).

[81] T. Adler, C.R. Houska, Simplifications in the x-ray line-shape analysis, J. Appl. Phys. 50(5) (1979) 3282-3287.

[82] A. Leineweber, E.J. Mittemeijer, Notes on the order-of-reflection dependence of microstrain broadening, J. Appl. Crystallogr. 43(5) (2010) 981-989.

[83] Z.H. Ni, H.M. Wang, J. Kasim, H.M. Fan, T. Yu, Y.H. Wu, Y.P. Feng, Z.X. Shen, Graphene thickness determination using reflection and contrast spectroscopy, Nano Lett. 7(9) (2007) 2758-2763.

[84] K. Wang, R.R. Reeber, Thermal expansion of Copper, High Temp. Mater. Sci. 35 (1996) 184-185.

[85] N. Mounet, N. Marzari, First-principles determination of the structural, vibrational and thermodynamic properties of diamond, graphite, and derivatives, Phys. Rev. B 71(20) (2005) 205214.

[86] J.F. Nye, Physical properties of crystals, University Press, Oxford, 1972, p.131.

Publication list

I: Publications in international journals

[1] **Hailong Shi**, Shulin Xiang, Xiaoshi Hu, Xiaojun Wang, Chao Xu. Fabrication and strengthening mechanisms of magnesium matrix composites with bimodal microstructure induced by graphene nanoplatelets. Journal of Materials Research. pp 1-11, 2021. **IF=2.502**

[2] **Hailong Shi**, Weimin Gan, Claude Esling, Xiaojun Wang, Yudong Zhang, Emad Maawad, Andreas Stark, Xiaohu Li, Lidong Wang. Acta Materialia. 200, pp 338-350, 2020. **IF=7.656**

[3] **Hailong Shi**, Xiaojun Wang, Xiaoshi Hu, Linglong Meng, Xuesong Leng, Kun Wu. Interfacial modification using matrix alloying in Mg/CNT composites for improved mechanical performance. Journal of Materials Engineering and Performance. 28, pp 3041-3047, 2019. **IF=1.652**

[4] **Hailong Shi**, Xiaojun Wang, Chunlei Zhang, Chendong Li, Wu Kun, Xiaoshi Hu. A novel melt processing for Mg matrix composites reinforced by multiwalled carbon nanotubes. Journal of Materials Science & Technology. 32, pp 1303-1308, 2016. **IF=6.155**

[5] Chao Ding, **Hailong Shi**, Kun Wu, Xiaojun Wang, Weimin Gan, Xiaoshi Hu, Chao Xu. Processing, Microstructure and Mechanical Properties of a Novel Mg Matrix Composites Reinforced with Urchin-like CNTs@SiCp. Diamond & Related Materials. 109, pp 109087, 2020. **IF=2.650**

[6] Xiaojun Wang, **Hailong Shi**, Xiaoshi Hu, Linglong Meng, Kun Wu. Improved strengthening efficiency of nanoreinforcements realized by a novel melt spinning process. Journal of Materials Research. 33, pp 2711-2720, 2018. **IF=2.502**

[7] Linglong Meng, Xiaojun Wang, Xiaoshi Hu, **Hailong Shi**, Kun Wu. Role of structural parameters on strength-ductility combination of laminated carbon nanotubes/copper composites. Composite Part A. 116, pp 138-146, 2019. **IF= 6.444**

[8] Miao Wang, Yu Zhao, Lidong Wang, Yunpeng Zhu, Xiaojun Wang, Jie Sheng, Ziyue Yang, **Hailong Shi**, Zhendong Shi, Weidong Fei. Achieving high strength and ductility in graphene/magnesium composite via an in-situ reaction wetting process. Carbon. 139, pp 954-

963, 2018. **IF=8.821**

[9] Linglong Meng, Xiaoshi Hu, Xiaojun Wang, Chunlei Zhang, **Hailong Shi**, Yeyang Xiang, Nanjia Liu, Kun wu. Graphene nanoplatelets reinforced Mg matrix composite with enhanced mechanical properties by structure construction. Materials Science and Engineering A. 733, pp 414-418, 2018. **IF=4.652**

II: Contributions to International Conferences

[1] **Hailong Shi**, Xiaojun Wang, Chendong Li, Kun Wu. Interfacial modification in CNTs reinforced Mg matrix composite. Oral presented in the "21st International Conference on Composites Materials (ICCM-21)". Xi'an, August 2017.

[2] **Hailong Shi**. Attended in the 11th European Symposium on "Martensitic Transformations" as volunteer student. France, August 2018.

[3] **Hailong Shi**, Yudong Zhang, Xiaojun Wang, Weimin Gan, Claude Esling. Texture evolution of a laminated graphene nanoparticles (GNP) reinforced copper matrix composites. Oral presented in the "Annual Texture Symposium" of DGM-F2M at MLZ. Munich, March 2019.

[4] **Hailong Shi**, Xiaojun Wang. A melt proessing for fabrication of CNT/Mg-6Zn composites. Poster presented in "the 10th Pacific Rim International Conference on Advanced Materials and Processing". Xi'an, August 2019.

[5] **Hailong Shi**, Yudong Zhang, Weimin Gan, Xiaojun Wang, Andreas Stark, Emad Maawad, Norbert Schell, Xiaohu Li, Claude Esling. In-situ investigation of orientation monopolization of Cu in GNS/Cu laminated composite during vacuum hot-pressing sintering using synchrotron dilatometer. Poster presented in the DESY Photon Science user's meeting 2020. Hamburg, January 2020.

Acknowledgement

My PhD work is completed at the Laboratoire d'Étude des Microstructures et de Mécanique des Matériaux (LEM3), UMR CNRS 7239, Université de Lorraine, Metz, France, the School of Materials Science and Engineering, Harbin Institute of Technology, Harbin, China and the GEMS at Heinz Maier-Leibnitz Zentrum (MLZ), Garching, Germany. It is my great honor to study at these three institutions. I would like to express my sincere thanks to all persons who help me in my study and live.

My stay in France an in Germany was financially supported by the China Scholarship Council (Grant No.201706120156), Helmholtz-Zentrum Geesthacht, Munich, Germany and LabEx DAMAS, Université de Lorraine. I would also like to express my sincere thanks to these three institutions.

I sincerely gratitude to my supervisors, Dr. Yudong Zhang at Université de Lorraine, France, Dr. Weimin Gan at Helmholtz-Zentrum Geesthacht, Germany, Professor Lidong Wang and Professor Xiaojun Wang at Harbin Institute of Technology, China, for their constant guidance and selfless help in my PhD work and daily life. I have benefited greatly from their academic attitude. I would like to express my deepest gratitude to Professor Claude Esling for his help in my research work and daily life in France.

I would like to thank the two reviewers for their efforts and time to review my dissertation, and to thank all the jury members for taking time out of their schedules to achieve my dissertation defense.

I would like to express my thanks to all the staffs and students in the laboratory of LEM3 in Metz, FRM-II in Garching and the laboratory in Harbin Institute of Technology. They shared their experiences with me and offered help to my PhD work, especially to Dr. Benoit Beausir and Dr. Jean-Jacques Fundenberger at LEM3, for their great efforts developing new functions in the software package ATEX which supported the texture and orientation analyses in my work, to Dr. Michael Hofmann and Dr. Xiaohu Li at STRESS-SPEC (MLZ), Garching and Dr. Andreas Stark and Dr. Emad Maawad at HEMS (DESY), Hambourg, for their support during the experiments.

Last but not least, I would like to express my deep love and gratitude to my wife for her understanding and support during my study abroad and to my parents and sisters for their generous love and support in my life.